University of New Mexico
UNM Digital Repository

Optical Science and Engineering ETDs | Engineering ETDs

Spring 4-24-2022

Design and Characterization of Frequency Tripling Mirrors

Amir Khabbazi Oskouei
University of New Mexico

Follow this and additional works at: https://digitalrepository.unm.edu/ose_etds

 Part of the Atomic, Molecular and Optical Physics Commons, and the Optics Commons

Recommended Citation

Khabbazi Oskouei, Amir. "Design and Characterization of Frequency Tripling Mirrors." (2022).
https://digitalrepository.unm.edu/ose_etds/85

This Thesis is brought to you for free and open access by the Engineering ETDs at UNM Digital Repository. It has been accepted for inclusion in Optical Science and Engineering ETDs by an authorized administrator of UNM Digital Repository. For more information, please contact disc@unm.edu.

Amir Khabbazi Oskouei

Candidate

Electrical and Computer Engineering

Department

This dissertation is approved, and it is acceptable in quality and form for publication:

Approved by the Dissertation Committee:

Wolfgang Rudolph, Chairperson

Mansoor Sheik-Bahae

Ganesh Balakrishnan

Luke Emmert

Design and Characterization of Frequency Tripling Mirrors

by

Amir Khabbazi Oskouei

B.S., Physics, Tabriz University, 2009
M.S., Photonics, Shahid Beheshti University, 2012
M.S., Optical Science and Engineering, University of New Mexico, 2017

DISSERTATION

Submitted in Partial Fulfillment of the

Requirements for the Degree of

Doctorate of Philosophy
Optical Science and Engineering

The University of New Mexico

Albuquerque, New Mexico

May, 2022

©2022, Amir Khabbazi Oskouei

Dedication

To Zahra

Acknowledgments

I would like to thank my supervisor prof. Wolfgang Rudolph for his time, and energy to guide me through my PhD. I appreciate his patience in teaching me in understanding and solving a problem.

I also thank prof. Luke Emmert for many useful discussion and comments, and training me with many equipment and devices in the lab. I thank our previous lab members, specially Sebastian Baur who had contribution in the study of material modification in FTMs.

In addition, I thank prof. Detlev Ristau and his group, prof. Marco Jupe, prof. Thomas Willemsen, Morten Steinecke, and Sebastian Balendat and many others from Laser Zentrum Hannover, for fabrication of FTM samples and useful discussions. Morten also joined our lab for a time and helped in conduction of experiments to study FTM performance during the pulse illumination.

I also like to thanks my committee members prof. Mansoor Sheik-Bahae, prof. Ganesh Balakrishnan, for many useful comments. Thanks to prof. Matthias Lenzner for many useful discussions.

Thanks to my mother and brothers, and all my family and friends for the their help and support.

Finally, I like to thank my wife for her endless love.

Design and Characterization of Frequency Tripling Mirrors

by

Amir Khabbazi Oskouei

B.S., Physics, Tabriz University, 2009

M.S., Photonics, Shahid Beheshti University, 2012

M.S., Optical Science and Engineering, University of New Mexico, 2017

Ph.D., Optical Science and Engineering, University of New Mexico, 2022

Abstract

Aperiodic stacks of dielectric low- and high-index films can be designed to enhance third-harmonic generation (THG) in reflection of near infrared laser pulses using computer optimization. Numerical and analytical results suggest that the TH energy increases rapidly with increasing number of films and the ratio of the high and low index.

Our optical matrix based THG model that takes into account the full pulse bandwidth predicts conversion efficiencies of about 7 % for transform-limited Gaussian pulse bandwidths of 16 nm for mirrors with 45 layers, which exceed those expected from periodic designs. Stability against film thickness fluctuations expected from the deposition process and information about laser-induced damage are components of the design process.

Frequency tripling mirrors manufactured from hafnia and silica by our collaboration partners in the Laser Center in Hannover according to our designs showed maximum conversion efficiencies of about 2% for 60 fs pulses at 815 nm.

The main obstacle to achieving higher conversion efficiencies in practice are undesired material modifications in the currently used dielectric materials, observed during a single pulse and pulse trains in the high-index layer.

Contents

List of Figures

List of Tables

Chapter 1

Introduction

Nonlinear optics governs the interaction of intense laser light with matter [7]. Since the advent of the laser and the observation of second harmonic generation by Franken in 1961 [8], nonlinear optics research has attracted enormous attention ranging from fundamental light-matter studies to applications such as laser frequency conversion and optical switching.

The polarization P of a material produced by a laser with electric field E can formally be written as:

$$P = \epsilon_0 \left(\chi^{(1)} E + \chi^{(2)} E^2 + \chi^{(3)} E^3 + ... \right), \tag{1.1}$$

where ϵ_0 is the free-space permittivity and $\chi^{(n)}$ the susceptibility of n-th order. In the regime of linear (classical) optics, only the term with $n = 1$ is considered and the medium response P is a linear function of the applied electric field E. The nonlinear terms are particularly important for illumination with short laser pulses due to their high peak intensity.

Third harmonic (TH) generation (THG), the subject of this thesis, is a third order nonlinear optical process, described by the term with $n = 3$. Incident radi-

ation of frequency ω is converted to radiation of frequency 3ω [9]. The energy of a created photon is equal to the total energy of the three incident photons (energy conservation). In addition, photon momenta have to be conserved, which leads to a phase matching condition for efficient conversion.

THG was first observed in Calcite in 1962 [10], and since then, it has found many applications. The most obvious (and important) application is to produce laser radiation at shorter wavelengths using well-developed and efficient sources at longer wavelengths. A large-scale example is the production of UV pulses at 10 kJ energy for the National Ignition Facility (NIF) [11]. The pulses at 351 nm are the TH of the 1053-nm pulses delivered by a Nd:glass laser system [12]. Direct generation of equally powerful UV laser pulses in a laser is not possible today, and the need for efficient laser-target interaction makes frequency conversion necessary.

THG has also found applications in microscopy [13]. Here, the image represents a 2D map of the nonlinear susceptibility of third order, $\chi^{(3)}(x, y)$, which often contains information complementary to ordinary microscopy. Compared to other nonlinear imaging techniques, for example second-harmonic microscopy, TH microscopy is particularly interesting because all materials possess non-zero $\chi^{(3)}$. TH microscopy is particularly interesting for biomedical applications, see for example [14], and in material science and engineering, see for example [15].

In practice, to generate radiation at the third harmonic frequency, one can use direct frequency conversion in a $\chi^{(3)}$-medium, see for example [16, 17] or a cascade of quadratic ($\chi^{(2)}$) nonlinearities, see for example [18, 17]. The latter is often the choice for converting short laser pulses because of the availability of nonlinear materials (crystals) with large $\chi^{(2)}$. The conversion efficiency depends on the incident intensity (or fluence) and is ultimately limited by the laser induced damage threshold (LIDT) in both techniques. High nonlinear susceptibilities and large LIDTs are thus desirable.

At high incident intensities other nonlinear processes can occur below LIDT and have a detrimental effect on THG. The Kerr effect, another nonlinearity of third order, causes a refractive index change which can lead to self-focusing and phase mismatch. Multi-photon absorption can also produce an index change and represents losses for the fundamental field.

While the specifics depend on the material, as a rule of thumb, large bandgaps are often of advantage even though they also tend to reduce the $\chi^{(3)}$ for THG. In addition, to frequency-convert ultrashort pulses without broadening, dispersive effects must be controlled. This often calls for thin optical elements. Obviously, because of these competing dependencies, compromises have to be made when choosing nonlinear optical elements.

An attractive combination of material parameters can be found in nonlinear optical crystals such as BBO, KTP, and LBO, which are often the elements of choice for nonlinear frequency conversion. For the direct conversion of femtosecond laser pulses efficiencies on the order of 10% were reported using BBO and incident intensities of 1 TW/cm^2 [19]. Most commercially available frequency triplers for fs laser pulses, however, use two crystals and frequency doubling followed by sum frequency generation [18, 20].

Depending on the application, crystals are relatively expensive, prone to optical damage and are not always environmentally stable (e.g., hygroscopic). For reasons like these and despite great progress in crystal growth, there has always been interest in alternative nonlinear optical components.

Two orders of magnitude enhancement of THG in silicon disk nanoparticles with respect to bulk silicon was demonstrated through the resonant modes of such nanoparticles controlling the electromagnetic field enhancement [21]. THG is also observed in graphene and in few-layer graphite films, where the TH signal was pro-

portional to the cube of the fundamental light intensity and the square of the numbers of atomic layers when the resonance condition of the light-graphene interaction was met [22]. The conversion efficiency still remained low. A THG efficiency of 1 percent was observed in a noncrystalline film of ZnO limited by the damage threshold of the material [16].

This thesis deals with aperiodic stacks of amorphous dielectric films on substrates to generate the TH. Such film stacks have found broad applications as linear optical elements, such as mirrors, beam splitters and polarizers.

Film deposition techniques and materials have been researched and developed over many decades. Large (meter-size) diameter samples can be produced relatively cost-effective and fast compared to crystals. From the near ultraviolet (UV) to the near infrared (IR) spectral region metal oxides are often used as coating materials, for example silica (SiO_2), hafnia (HfO_2), tantala (Ta_2O_5), alumina (Al_2O_3) [1], due to their environmental robustness, ready availability, ease of handling and large LIDT.

At first glance, the small $\chi^{(3)}$ values and small individual film thicknesses (typically < 400 nm) should prohibit noteworthy THG. Indeed, early experiments on THG using off-the-shelf high-reflecting (HR) mirrors (HRs) showed conversion efficiencies $< 10^{-5}$ with illumination by 300 fs pulses at 775 nm from a high-energy laser system [23]. The authors wanted to study the undesired THG in reflection by HRs to assess UV induced damage in optical components downstream.

The question arose whether a multilayer system of dielectric films designed to maximize TH in reflection could produce substantially higher efficiencies through the combined effect of all layers leading to a practical, easy to align, TH frequency converter that we will dub frequency-tripling mirror (FTM).

Neglecting pulse bandwidth effects, the TH energy in reflection from an FTM,

U_{TH}, can formally be written as

$$U_{TH} = \mathcal{Q}(\vec{n}, \vec{d}, \vec{\chi}^{(3)}) U_F^3 \tag{1.2}$$

where U_F is the energy of the incident pulse at the fundamental frequency. The factor $\mathcal{Q}\left(\vec{n}, \vec{d}, \vec{\chi}^{(3)}\right)$ is a design parameter that depends on the refractive indexes of all layers lumped into a vector $\vec{n}$ and corresponding vectors for the film thicknesses, $\vec{d}$, and nonlinear susceptibilities, $\vec{\chi}^{(3)}$. The number of layers and the materials they are made of determine $\vec{n}$ and $\vec{\chi}^{(3)}$). These are the input vectors for a typical design process, and $\vec{d}$ is the output that maximizes $\mathcal{Q}$. Prototype FTMs were designed and tested preliminary in our lab a few years ago, producing a maximum THG efficiency of about 1% [24]. While this is sufficient for certain applications, like producing probe pulses for pump-probe experiments or seed pulses for amplifiers, larger efficiencies are desirable.

The goals of my thesis were to explore the full potential of FTMs, develop new design concepts and FTMs that can be produced, experimentally test their performance and investigate technical and fundamental limits of FTMs with respect to conversion efficiency and bandwidth. The mirrors were manufactured by our collaboration partners according to our designs in the Laser Zentrum Hannover (LZH, group of Prof. D. Ristau) using ion-beam sputtering.

The thesis manuscript is structured as follows:

- In Chapter 2 we will review THG for monochromatic waves and laser pulses, concentrating on aspects that are relevant for FTMs.
- In Chapter 3 we will describe the laser sources and major instrumentation that we used to study FTMs and related laser-material interactions.
- Chapter 4 introduces FTMs and the design processes. Through modeling we will investigate how the conversion efficiency and bandwidth scales with the

number of films and derive analytical dependencies. The effect of film material properties (absorption and refractive index) will be discussed. All simulations are performed assuming monochromatic input.

- In Chapter 5 a model will be developed to take into account the pulse bandwidth. We will discuss the properties of the designs optimized with the pulse model. In addition, we will discuss the results of fabricated samples based on the optimum designs.

- Chapter 6 discusses the physical mechanisms of TPA and electron-plasma formation in a stack of dielectric material under the illumination with high fluence fundamental beam. The effect of TPA and electron-plasma formation on the conversion efficiency of THG, TH spectra, and beam profile is discussed.

- Chapter 7 summarizes the main results of the thesis and discusses possible future research directions.

Chapter 2

Theory of Third Harmonic Generation

In this chapter, the theory of third harmonic generation (THG) and its features will be discussed for the case of monochromatic plane wave, monochromatic Gaussian beam, and a transform-limited pulse with Gaussian profile. We will also introduce briefly the laser induced damage threshold (LIDT) in dielectric materials under illumination with short laser pulses.

2.1 Wave Equation

When an external electric field is applied to matter, it induces a polarization. This polarization is linearly proportional to the applied electric field. However when the electric field magnitude increases, the linear relation does not hold any longer, and

the polarization of the material will depend on higher powers of the electric field:

$$\begin{aligned}\mathbf{P}(\mathbf{r},t) &= \mathbf{P}_L(\mathbf{r},t) + \mathbf{P}_{NL}(\mathbf{r},t) \\ &= \epsilon_0\chi^{(1)}\mathbf{E}_F(\mathbf{r},t) + \epsilon_0\left(\chi^{(2)}\mathbf{E}_F^2(\mathbf{r},t) + \chi^{(3)}\mathbf{E}_F^3(\mathbf{r},t) + ...\right) \quad (2.1)\end{aligned}$$

where, $\chi^{(1)}$ is the susceptibility of linear optics, $\chi^{(2)}$ and $\chi^{(3)}$ are the second and third order susceptibilities, respectively. $\epsilon_0 = 8.85 \times 10^{-12}$ F/m is the permittivity of free space. $\mathbf{P}(\mathbf{r},t)$ is the polarization of the material and $\mathbf{E}_F(\mathbf{r},t)$ is the applied electric field. $\mathbf{r}$ and t are the position vector and time, respectively.

The $\chi^{(n)}$ are $(n+1)$th rank tensors. In the thesis we will deal with isotropic materials only, so the elements of the tensors have the same value. Isotropic materials are centrosymmetric and their $\chi^{(2)}$ is zero. Third order processes will be the lowest nonlinear optical process in such materials. We will ignore the frequency dependence of second and third order susceptibilities throughout this thesis, because the material responses allocated to them can be considered instantaneous at pulse durations $>$ 40 fs [4].

The wave equation that governs the generation of the nonlinear electric field $\mathbf{E}(\mathbf{r},t)$ in the presence of polarization as a source is [7]:

$$\nabla \times \nabla \times \mathbf{E} + \frac{n^2}{c^2}\frac{\partial^2\mathbf{E}}{\partial t^2} = -\frac{1}{\epsilon_0 c^2}\frac{\partial^2\mathbf{P}_{NL}}{\partial t^2} \quad (2.2)$$

where, n is the refractive index at the frequency of the generated electric field $\mathbf{E}(\mathbf{r},t)$, and $c = 299792458$ m/s is the speed of light. The first term on the left hand side of Eq. (2.2) can be expanded to:

$$\nabla \times \nabla \times \mathbf{E} = \nabla(\nabla \cdot \mathbf{E}) - \nabla^2\mathbf{E} \quad (2.3)$$

The first term on the right hand side of Eq. (2.3) would be neglected throughout this context we would be dealing with plane waves. Because in case of transverse, plane wave $\nabla \cdot \mathbf{E}$ vanishes [7]. So the nonlinear wave equation under the stated

approximations can be written as:

$$\nabla^2\mathbf{E} - \frac{n^2}{c^2}\frac{\partial^2\mathbf{E}}{\partial t^2} = \frac{1}{\epsilon_0 c^2}\frac{\partial^2\mathbf{P}_{NL}}{\partial t^2} \tag{2.4}$$

2.2 The Generation and Propagation of TH Produced by Monochromatic Plane Wave

THG is a process of producing a wave that oscillates at the frequency 3ω by mixing three waves with the same fundamental frequency ω. In this section, we solve the nonlinear wave equation of THG produced by a monochromatic plane wave. Figure 2.1 shows the coordinate system, where the fundamental electric field $\mathbf{E}_F(z,t)$ at frequency ω is in the direction of the x-axis, and the wave propagates in the direction of the z-axis.

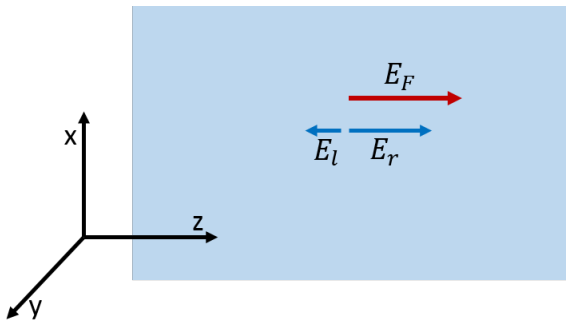

Figure 2.1: THG due to a fundamental at a medium.

The electric field of the fundamental wave in the direction of the z-axis induces a polarization in the xy-plane in an isotropic medium, which will emit TH waves in both the positive and negative directions of the z-axis. In other words, the TH wave will be generated in forward (backward) direction relative to the fundamental wave.

$$E_F(z,t) = Ae^{i(\omega t - kz)} + c.c. \tag{2.5}$$

$$E_r(z,t) = B_r(z)e^{i(3\omega t-\kappa z)} + c.c. \tag{2.6}$$

$$E_l(z,t) = B_l(z)e^{i(3\omega t+\kappa z)} + c.c. \tag{2.7}$$

Equation (2.5) shows the electric field of the fundamental monochromatic plane wave propagating in the positive direction of the z-axis. We assume no pump depletion, which means A is a constant amplitude. It is a justifiable assumption as far as the efficiency of fundamental conversion to TH is below 10-20 %. $E_r(z,t)$ and $E_l(z,t)$ are the TH electric fields that propagate in the direction of positive and negative z-axis, respectively. $B_r(z)$ and $B_l(z)$ are the amplitude of forward and backward propagating TH waves, respectively. k and κ are the wavevectors of fundamental and TH waves, respectively.

Plugging the Eqs. (2.5) and (2.6) into the wave equation Eq. (2.4), see Appendix A, yields the differential equation that governs THG in the direction of the positive z-axis

$$\frac{\partial B_r(z)}{\partial z} = -\frac{9i\omega^2\chi^{(3)}}{2\kappa c^2}A^3e^{-i\Delta k_- z} \tag{2.8}$$

and for THG in the direction of the negative z-axis

$$\frac{\partial B_l(z)}{\partial z} = \frac{9i\omega^2\chi^{(3)}}{2\kappa c^2}A^3e^{i\Delta k_+ z}. \tag{2.9}$$

Here $\Delta k_\pm = 3k \pm \kappa$ is the wavevector mismatch. In addition, in deriving the differential equations Eq. (2.8), and (2.9) we used the slowly varying envelope approximation (SVEA).

$$\left|\frac{\partial^2 B_{r,l}(z)}{\partial z^2}\right| << 2\kappa \left|\frac{\partial B_{r,l}(z)}{\partial z}\right|. \tag{2.10}$$

Solving the differential equations Eq. (2.8), and (2.9), we obtain the amplitude of the electric field in both forward and backward directions. Then, we plug them in the equations Eq. (2.6) and Eq. (2.7).

$$E_r(z,t) = \left[B_{r,0} - \frac{9i\omega\chi^{(3)}z}{2\kappa c^2}A^3e^{-i\frac{\Delta k_- z}{2}}\,\mathrm{sinc}\left(\frac{\Delta k_- z}{2}\right)\right]e^{i(3\omega t-\kappa z)} \tag{2.11}$$

and

$$E_l(z,t) = \left[B_{l,0} + \frac{9i\omega\chi^{(3)}z}{2\kappa c^2} A^3 e^{-i\frac{\Delta k_+ z}{2}} \operatorname{sinc}\left(\frac{\Delta k_+ z}{2}\right) \right] e^{i(3\omega t+\kappa z)} \tag{2.12}$$

2.3 The Generation and Propagation of TH Produced by a Monochromatic Gaussian Beam

The electric field of a Gaussian beam that propagates in the direction of the positive z-axis [7].

$$E_F(r,z) = E_{F,0}\frac{w_0}{w(z)} e^{-\frac{r^2}{w^2}} e^{-\frac{ikr^2}{2R(z)}} e^{i\arctan(z/z_R)} \tag{2.13}$$

where, w_0 is the beam waist, $z_R = \pi w_0^2/\lambda$ is the Rayleigh range, $b = 2z_R$ is the confocal parameter. $w(z)$ is the beam radius

$$w(z) = w_0\sqrt{1+\left(\frac{z}{z_R}\right)^2} \tag{2.14}$$

at which the Gaussian beam intensity drops to $1/e^2$. $R(z)$ is the radius of curvature of the wavefront

$$R(z) = z\left(1+\left(\frac{z_R}{z}\right)^2\right). \tag{2.15}$$

The nonlinear wave equation Eq. (2.4) for THG in the case of a Gaussian beam is:

$$2i\kappa\frac{\partial B}{\partial z} + \nabla_T^2 B = -\frac{(3\omega)^2}{c^2}\chi^{(3)}E_F^3 e^{i\Delta kz} \tag{2.16}$$

where, $\Delta k = 3k - \kappa$ is the phase mismatch of fundamental and TH waves. Equation (2.16) can be solved based on the fact that the TH wave will have the same symmetry as fundamental wave.

$$B(z) = \frac{3i\omega}{2\eta c}\chi^{(3)}E_{F,0}^3\int_{z_0}^{z}\frac{e^{i\Delta kz'}}{(1+2iz'/b)^2}dz' \tag{2.17}$$

where, z_0 is the position in the medium where the fundamental Gaussian wave begins propagation. At the limit of $b \gg |z_R|, |z - z_0|$, Eq.(2.17) simplifies to the case of THG with a plane wave.

The electric field of the TH wave will be:

$$E(z) = B(z)e^{-\frac{3r^2}{w_0^2}} e^{i\kappa z} \tag{2.18}$$

and the power associated with this electric field is:

$$P(z) = \frac{\pi}{3} c\epsilon_0 w_0^2 |B(z)|^2 \tag{2.19}$$

2.4 The Generation and Propagation of TH Produced by a Fundamental Pulse

THG using a fundamental pulse is important, because we will use femtosecond pulsed laser as the fundamental pulse to excite an FTM. Since a femtosecond pulse has a large peak power, so under right focusing condition it will generate high intense fundamental beam to generate efficient TH. Since, TH conversion efficiency scales with square of the fundamental intensity, it leads to efficient fundamental conversion to TH. Let's assume, a transform-limited pulse with a Gaussian temporal profile as shown in Eq. (2.20).

$$E_F(z,t) = E_{F,1}(z,t)e^{i(\omega t - kz)} + c.c. \tag{2.20}$$

where, τ_G is the Gaussian pulse duration, and $E_{F,1}(z,t) = E_{F,0}e^{-\frac{t^2}{\tau_G^2}}$ which $E_{F,0}$ is the amplitude of the fundamental electric field. The differential equation that governs the THG in a medium by a pulse is [25],

$$\left(\frac{\partial}{\partial z} + \frac{1}{v_{g3}}\frac{\partial}{\partial t}\right) B(z,t) = -\frac{9i\omega^2\chi^{(3)}}{2k_3c^2} e^{-i\Delta kz} E_{F,1}(z,t) \tag{2.21}$$

where, v_{g3} is the group velocity at TH frequency, and k_3, and k_1 are the wavevectors at the central wavelength of TH, and fundamental pulse respectively. $\Delta k = 3k_1 - k_3$ is the wavevector mismatch. For simplicity, we took only the TH field that is generated in forward direction (+z) and ignored the other term, where it has a form as Eq. (2.22).

$$E(z,t) = B(z,t)e^{i(3\omega t - k_3 z)} + c.c. \tag{2.22}$$

In a retarded frame using $\tau = t - \frac{z}{v_{g3}}$ and $\xi = z$ relation and assuming k_3 is a linear function of frequency, the analytical solution of the differential equation will be [25],

$$B(d,\tau) = -\frac{9i\omega^2\chi^{(3)}}{2k_3c^2}\int_0^d d\xi e^{-i\Delta k\xi}E_{F,1}^3\left(0, \tau + \left(\frac{1}{v_{g3}} - \frac{1}{v_{g1}}\right)\xi\right) \tag{2.23}$$

where, v_{g1} is the group velocity at fundamental frequency. Taking a Fourier transform of this relation, and conducting integration over ξ will lead to

$$B(d,\Omega) = -\frac{1}{(2\pi)^2}\frac{9i\omega^2\chi^{(3)}}{2k_3c^2}de^{i\frac{\phi}{2}}\operatorname{sinc}\left(\frac{\phi}{2}\right)\times \int_{-\infty}^{+\infty}d\Omega' E_{F,1}(\Omega-\Omega')\int_{-\infty}^{+\infty}d\Omega'' E_{F,1}(\Omega'-\Omega'')E_{F,1}(\Omega'') \tag{2.24}$$

where $\phi = \Omega(\frac{1}{v_{g3}} - \frac{1}{v_{g1}})d - \Delta kd$ is the phase mismatch parameter. Substituting the Gaussian profile $E_F(z,t)$ into Eq. (2.23), and (2.24), yields the below relations for TH field amplitude in case of a Gaussian pulse in time domain.

$$B(d,\tau) = \frac{9i\omega^2\chi^{(3)}}{2k_3c^2}E_{F,0}^3\int_0^d d\xi e^{-i\Delta k\xi}\exp\left\{-\frac{3\left[\tau + \left(\frac{1}{v_{g3}} - \frac{1}{v_{g1}}\right)\xi\right]^2}{\tau_G^2}\right\} \tag{2.25}$$

and frequency domain

$$B(d,\Omega) = -\sqrt{\frac{\pi}{3}}\frac{9i\omega^2\chi^{(3)}}{2k_3c^2}\tau_G d E_{F,0}^3 e^{-\frac{\tau_G^2\Omega^2}{12}}e^{\frac{i\phi}{2}}\operatorname{sinc}\left(\frac{\phi}{2}\right) \tag{2.26}$$

The resulted conversion efficiency of THG is shown in Fig. 2.2 relative to propagation distance at different pulse duration, while peak amplitude of fundamental

pulse $E_{F,0}$ is fixed for all cases. As a comparison the THG with monochromatic plane wave is shown in Fig. 2.2. The conversion efficiency of a monochromatic plane wave oscillates with integer period of coherence length $\pi/\Delta k$. The coherence length is a propagation distance in a medium that THG begins from zero value until it reaches a peak. As the fundamental propagates further than coherence length in the medium it generates TH field, which is out of phase with TH field generated over the coherence length, and cancels it out. So the THG will oscillate with the propagation distance in the medium. The values of peaks and valleys would remain same if we ignore the absorption and material dispersion.

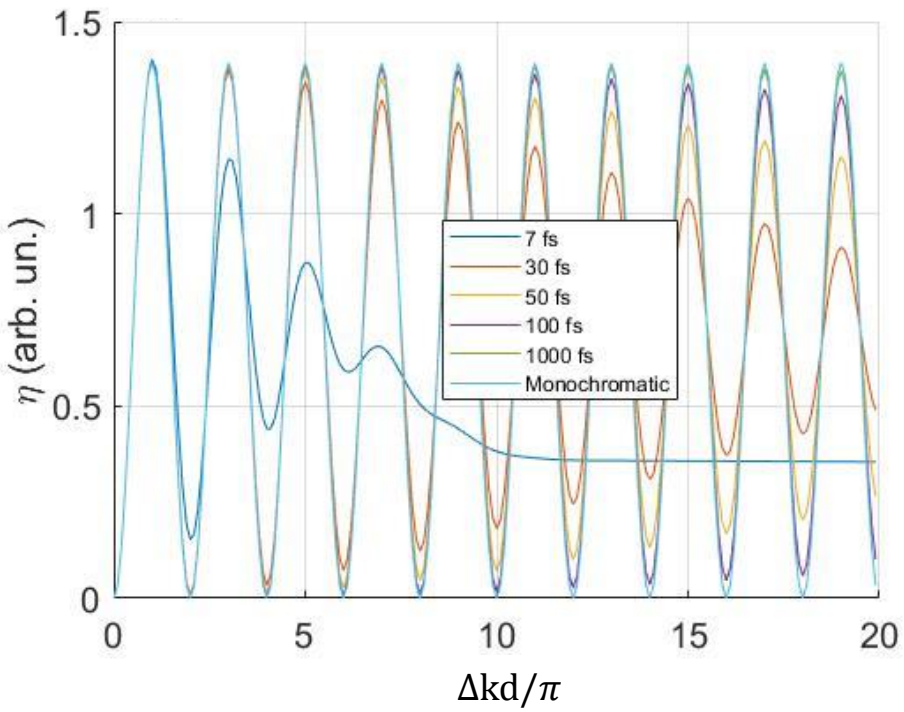

Figure 2.2: The conversion efficiency of THG relative to propagation distance inside a Hafnia (see Table 4.1) in case of a monochromatic plane wave at 800 nm and Gaussian pulse centered at 800 nm at the same fundamental peak amplitude, for different Gaussian pulse duration.

In case of a pulse that propagates in a medium, the conversion efficiency of THG will oscillate with coherence length. However, because of group velocity mismatch the peaks and (valleys) of conversion is no longer the same and their values will reduce(increase).

The TH conversion efficiency relative to distance at different pulse duration, is shown at fixed pulse energy in Fig. 2.3. The conversion efficiency of TH pulse increases with pulse duration with $1/\tau^2$. For example, the ratio of the first peaks of TH pulse energy corresponding to different pulse duration at the same pulse energy is $(\tau_2/\tau_1)^2$.Therefore, using shorter pulses would generate larger TH signal assuming no bandwidth limit of the nonlinear medium.

2.5 Laser Induced Damage Threshold of Dielectric Materials with Femtosecond Lasers

Since the TH conversion efficiency scales with square of fundamental beam intensity, to get the maximum TH conversion efficiency, it is important to know the damage threshold of the dielectric material. So, it is important to know how the damage threshold of dielectric materials depends on the pulse parameters. In this work, we will use an empirical function that is obtained from LIDT measurements on a single film of dielectric material coatings. The metal oxides like Hafnia, Alumina, and Tantala are often used in dielectric coatings from the near UV to near IR. measurements, and in this work we used Hafnia as a dielectric material in design of FTMs. This empirical function predicts a scaling law of $F_c \approx (c_1 + c_2 E_g)\tau_p^{\theta}$, where $\theta \approx 0.3$, $c_1 = -0.16 \pm 0.02$ Jcm^{-2}fs$^{-\theta}$, and $c_2 = 0.074 \pm 0.004$ Jcm^{-2}fs$^{-\theta}$eV^{-1} are material and pulse duration τ_p(the full width at half maximum of pulse intensity) independent parameters [1]. This phenomenological law also applies to composite

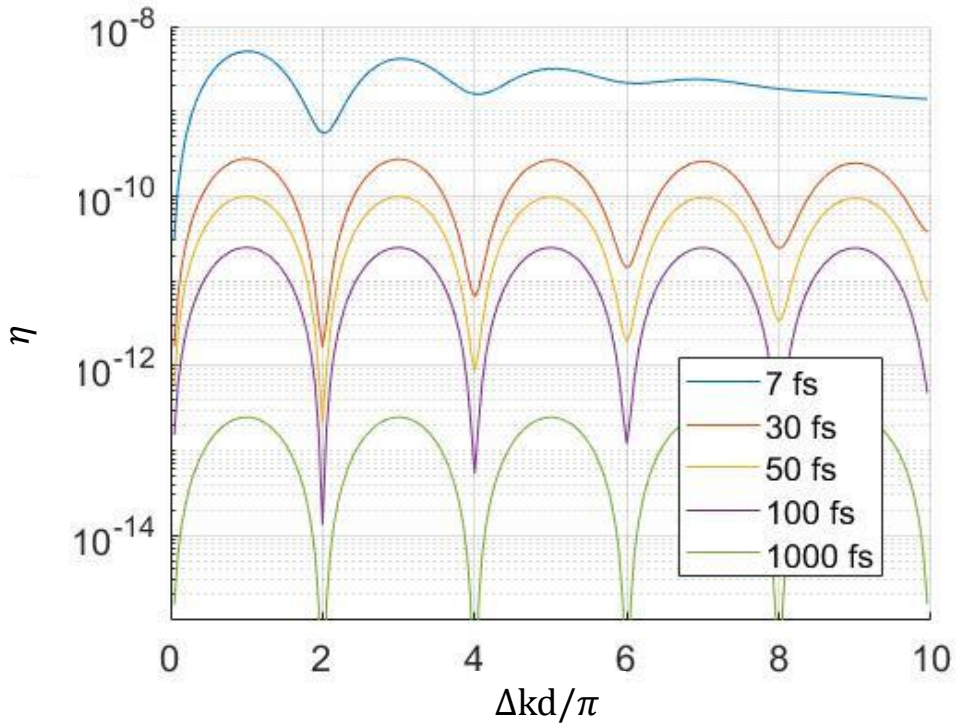

Figure 2.3: The conversion efficiency of THG relative to propagation distance in case of a monochromatic plane wave and Gaussian pulse at the same fundamental energy, for different Gaussian pulse duration.

(binary) oxides with tunable bandgap [26]. For instance, the damage threshold of a single layer Hafina with thickness of 568 nm on a top of a Silica substrate is 700 mJ/cm^2 at pulse duration of 50 fs and central wavelength of 800 nm. Note, the damage threshold of a layer depends on the electric field enhancement, and that is related to the thickness and refractive index of layer, and the substrate.

Absolute value of the max TH electric field respect to medium thickness is plotted for few dielectric materials in Fig. 2.4. The max TH electric field occurs at incident fundamental field that it reaches the damage threshold for pulse duration of 50 fs at central wavelength of 800 nm inside a material with thickness d. Figure. 2.4 indicates

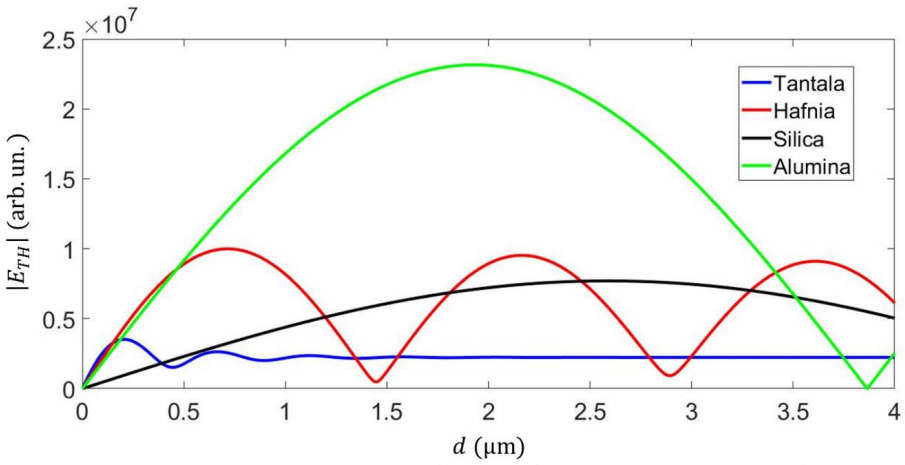

Figure 2.4: The relative TH field values at propagation distance longer than coherence length at the maximum applied fundamental fluence for pulse duration of $\tau_p = 50$ fs at central wavelength of 800 nm. see Tables B.1, and B.2.

that while Tantala and Hafnia have larger nonlinear susceptibility $\chi^{(3)}$ compared to Alumina and Silica, this is Alumina that will generate largest TH at coherence length at the damage threshold fluence. It must be noted that this case applies for wavelengths between 787 nm and 820 nm, where TH field of these materials are studied, because of the parameters of available laser sources. In general, the maximum TH field due to each material at its coherence length will be different at other spectral regime. Because, TH field also depends on dispersion of real and imaginary part of refractive index and the dispersion of $\chi^{(3)}$. For example it is the linear absorption at TH regime that dominantly determines TH conversion efficiency in Tantala.

Chapter 3

Experimental Setups

In this chapter, we will describe the two laser sources that are used to characterize FTMs. In addition, the general optical setups for the measurements are shown for reference. Minor modifications in the setups are pointed out in later chapters.

3.1 Ti:Sapphire oscillator

The experimental setup that is used to characterize FTM samples is shown in Fig. 3.1. The Ti:Sapphire oscillator generates a pulse train with 110 MHz repetition rate and 55 fs pulse duration at a central wavelength of 787 nm. The average output of laser is 1.1 W (with 1% variation over 30 s), which corresponds to an individual pulse energy of 10 nJ, and peak power of 200 kW. A typical pulse spectrum is shown in Fig. 3.2.

A half wave plate HW1 is used to tune the average power in combination with a Faraday isolator (FI). The latter also prevents any back reflection into the laser cavity. A second half wave plate HW2 is used to rotate the polarization of the laser beam before the Pockell cell (PC), which is used to select a predetermined number

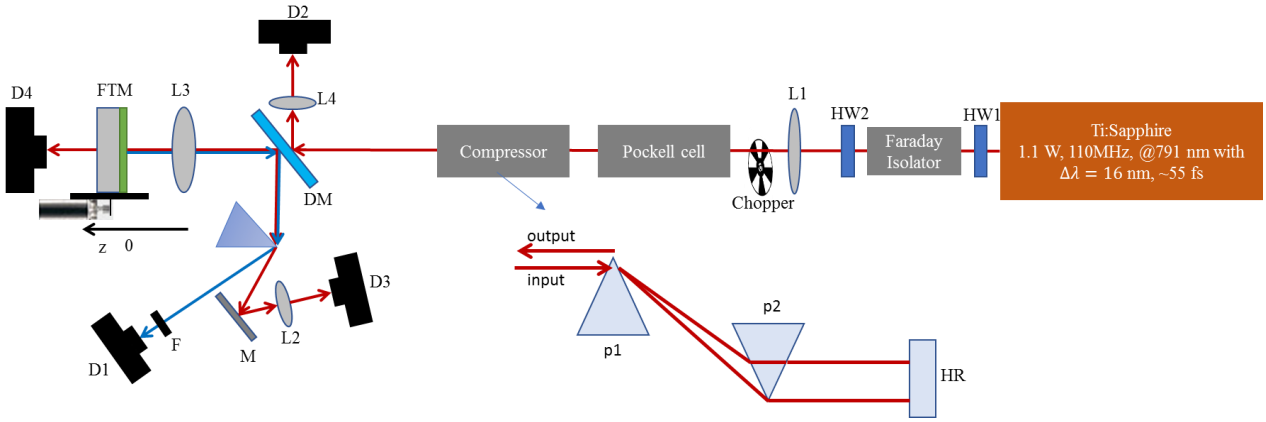

Figure 3.1: The optical setup to measure TH from an FTM sample using a laser oscillator with average power of 1.1 W, repetition rate of 110 MHz, at central wavelength of 791 nm as the source. HW1 and HW2: half wave plate at fundamental wavelength range, L1 through L4: lenses. p1 and p2: fused silica prisms cut for Brewster angle at minimum deviation. DM: dichroic mirror. M: a metal mirror. F: filter. Detectors: D1 (APD110A2) reflected TH, D2 (PDA55) reference fundamental, D3 (PDA36A) reflected fundamental, and D4 (PDA36A) transmitted fundamental. FTM: sample on a motorized micrometer translation stage. HR: high reflective mirror at fundamental wavelength range with angle of incidence of 0 degree.

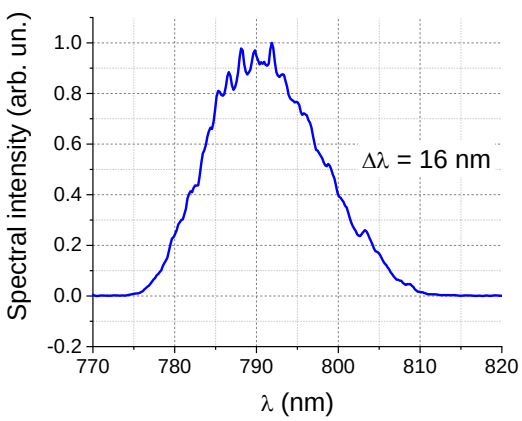

Figure 3.2: Typical spectrum of the output of our laser oscillator.

of pulses. Lens L1 is used to collimate the laser beam. The resulting beam waist of laser beam falls beyond the whole length of optical path from lens L1 up to the FTM sample. In case of illuminating the FTM sample with a continuous pulse train, a chopper and lock-in amplifier are used for detection of the TH. Because of normal dispersion of the materials in the FI and the PC, the laser pulses get stretched in time. The pulse duration of 55 fs after the FI increases to 150 fs, which is measured with GRating-Eliminated No-nonsense Observation of Ultrafast Incident Laser Light E-fields (GRENOUILLE) device [27]. The pulse duration of 55 fs after PC also stretches to 150 fs (note: the FI is removed from the path of beam for this measurement). The pulses then are sent into a two-prism pulse, double path, compressor. Prism p2 is used to fine tune pulse duration after compressor to reach minimum pulse duration by moving the prism in or out of the beam path (dispersion introduced by fused silica material). Note, the end mirror inside the compressor (HR), is tilted slightly so the output beam will be higher than the input beam to be able to couple the beam out. At the output of the compressor, the pulse duration is measured to be 55 fs, the same as right after the oscillator. Then beam passes through a DM that reflects TH (reflection $> 99\%$), and transmits the fundamental (transmission $> 93\%$). Note, the transmission spectrum of the DM at fundamental range, and its reflection in TH range is smooth, and varies by less than a percent. Finally a lens L3 is used to focus the beam onto the sample.

The beam size before lens is measured when the diameter of an iris is adjusted so that only 50% of laser power goes through. The diameter of iris is measured to be 7 ± 1 mm, which is 60% of $2\times$(beam radius). The generated TH in the FTM propagates back through lens L3, and bounces off DM. Since there is also residual fundamental beam that is reflected simultaneously with TH beam, a prism is used to isolate the TH beam from the fundamental beam. The filter F in TH spectrum is introduced to avoid the saturation of the detector D1, which is used to detect the TH signal. In general, there were two types of filters - interference and absorptive neutral density

(ND) filters. The interference filters were designed to allow only transmission of wavelengths that corresponds to the TH wave, with peak transmission of 5-20%, and a transmission bandwidth of 10-12 nm. Note, while interference filters are useful in blocking the fundamental beams mostly due to lots of scattering in the lab, because of their narrow bandwidth (comparable to the spectrum of TH pulses that have FWHM ≤ 3 nm). Care has to be taken to account for the actual attenuation factor depending on the peak of the TH spectrum relative to the spectral filter response.

The fundamental beam incident on the DM partially reflects. This beam is collected using lens L4 onto detector D2 as a reference to monitor the energy of individual pulses. The residual fundamental after the FTM sample is collected by detector D4 with a lens (not shown in the Fig. 3.1) to measure transmission. In addition, the fundamental beam that is separated from TH by the prism is used to measure the reflected fundamental on detector D3.

3.1.1 The Beam Waist Measurement Methods of Fundamental Beam

The beam waist (assuming a Gaussian beam profile) at focus is measured to be $w_0 = 6.2 \pm 0.3$ μm for an $f = 5$ cm lens. Two methods are applied to measure the beam waist. In the first method, a pinhole with radius of $a = 5$ μm is used to maximize the power through the pinhole by moving along the beam (to bring pinhole to the focal plane), and on the plane perpendicular to the beam. The power before(P_0) and after(P_t) pinhole could be related to the beam waist and pinhole size the equation Eq. (3.1) [28].

$$w_0 = \left[-\frac{2a^2}{\ln(1 - \frac{P_t}{P_0})} \right]^{\frac{1}{2}} \tag{3.1}$$

if we assume a Gaussian beam. The retrieved beam waist is estimated to be $w_0 = 6.1 \pm 0.2$ μm.

In the second method, the TH signal from an FTM is measured while its position is varied along the beam axis. Since the TH signal S_{TH} is proportional to the cube of the the fundamental intensity $I(r)$, TH signal could be estimated as Eq.(3.2). If we assume a fundamental beam with Gaussian profile $I(r) = I_0(\frac{w_0}{w})^2 e^{-\frac{2r^2}{w^2}}$, where I_0 is the beam intensity at the center of the beam $r = 0$, and $z = 0$. r, and z are positions in transverse plane (perpendicular to beam propagation direction), and along the beam with respect to the beam waist, respectively. $w = w_0\sqrt{1 + (\frac{z}{z_R})^2}$ is the beam radius at position z. w_0 is the beam waist and $z_R = \frac{\pi w_0^2}{\lambda}$ is the Rayleigh range of a beam with wavelength λ.

$$S_{TH} = C \int_0^\infty I^3(r) 2\pi r dr \tag{3.2}$$

where C is a constant. In case of a Gaussian beam, it yields:

$$S_{TH} = C \frac{4P^3}{3\pi^2 w_0^4} \left(1 + \left(\frac{z}{z_R}\right)^2\right)^{-2} \tag{3.3}$$

where $P = \frac{\pi w_0^2 I_0}{2}$ is the average power of the fundamental beam.

For example in Fig. 3.3, the TH signal from an FTM is measured relative to the position of sample z. The Eq. (3.3) is fitted to experimental points, and w_0 is extracted to be $w_0 = 6.2 \pm 0.3$ μm

In conclusion, there is a satisfactory consistency between these two methods. However, since the second method was more easy to apply, we mostly used this method to measure the beam waist.

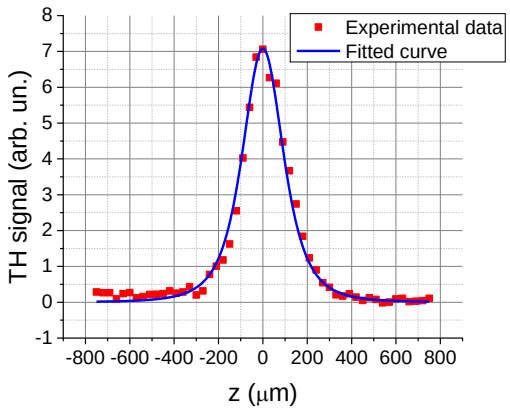

Figure 3.3: TH signal relative to the position of FTM sample z at the focus of fundamental beam.

3.2 The Short Pulse Amplifier

Another laser source we used was a chirped multi-pass pulse amplifier seeded by pulses from a Ti:Sapphire oscillator, see Fig 3.4. The latter generates a pulse train with 110 MHz repetition rate, 20 fs pulse duration at a central wavelength of 775 nm, with output power of 440 mW, which corresponds to an individual pulse energy of 4 nJ. The spectrum of the oscillator is measured using the back reflection of the wedged output coupler using a fiber coupled spectrometer. A diffuser and lens was used to couple all spectral components into the fiber. In addition, the diffuser reduced mode competition in the fiber. Typical spectra of oscillator nd amplifier are shown in Fig. 3.5.

Mirrors M2 through M5 steer the output beam of the oscillator toward the pulse energy controlling system. This power controlling system consists of a half wave plate (HWP) to rotate beam polarization, and two thin film polarizer (TFP) to only let the polarization parallel to the optical table pass. The reason to use two TFPs is to clean out further the wrong polarization, and also to avoid tranverse beam

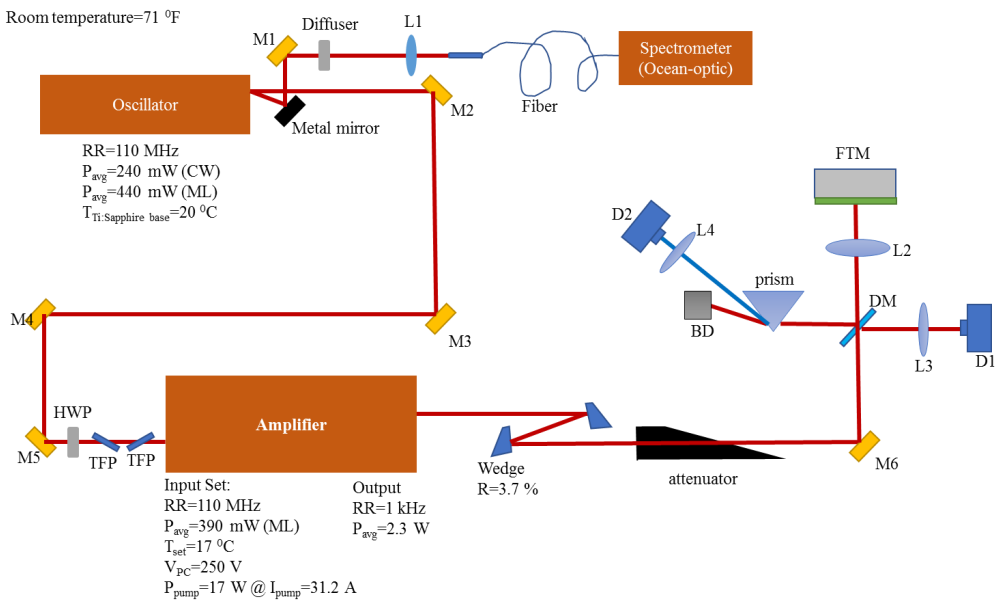

Figure 3.4: The schematic of optical setup used to measure TH from FTM samples at room temperature of 71 ^{0}F. Laser oscillator: repetition rate $RR = 110$ MHz, continuous wave (cw) average power $P_{avg} = 240$ mW, mode locked (ML) average power $P_{avg} = 440$ mW, crystal base temperature $T_{Ti:Sapphirebase} = 20\ ^0$C. M1, through M6: high reflective mirrors with angle of incidence of 45 degree. L1 through L4: lens. HWP: half wave plate. TFP: thin film polarizer. Amplifier: max input average power $P_{avg} = 390$ mW, temperature of base holder of Ti:Sapphire crystals $T_{set} = 17\ ^0$C, bias voltage of Pockell Cell (PC) $V_{PC} = 250$ V, average power of pump inside amplifier $P_{avg} = 17$ W at current $I_{pump} = 31.2$ A. D1 and D2: detector. BD: beam dumper.

deflection.

The amplifier picks 1 pulse out of 110000 pulses, and amplifies it using the multi pass chirped pulse amplification method [29]. The output of the amplifier are pulses with pulse duration of 42 fs, centered at 815 nm, with 1 kHz repetition rate, and average power of 2.3 W, which corresponds to pulse energy of 2.3 mJ. See Fig. 3.5 for the spectrum of the output pulses. Figure. 3.4 shows the practical parameters that are applied for normal function of the amplifier and oscillator as a record for

later use.

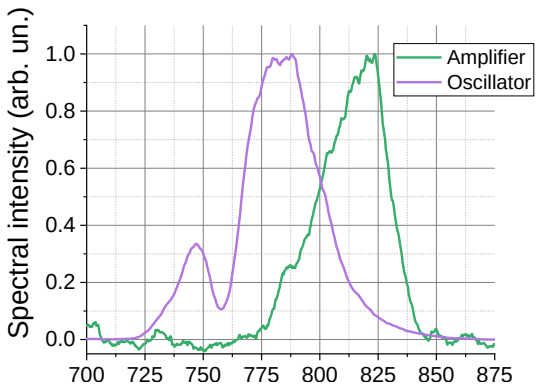

Figure 3.5: The output spectrum of laser oscillator and amplifier.

There is a pulse compressor based on two gratings inside the amplifier right before its output. The distance between the two gratings could be varied by moving the stage that is holding one of the gratings. The grating in the compressor system is always moved to the position for the shortest possible pulse.

The output beam of the amplifier bounces off two glass wedges to attenuate the pulse energy by a factor of approximately 730. So the pulse energy would be around 3μJ. However, it could be scaled up by replacing one of the wedges with a mirror, or a thin film beam splitter designed for femtosecond applications. Then, the beam passes through na attenuater, which is used as a controller to adjust the energy of the pulses. The beam is guided toward DM (reflects TH (reflection $>$ 99%), and transmits fundamental (transmission $>$ 93%)). The transmitted beam is focused using lens L2 onto the FTM sample. The generated TH is collected by L2 and is directed toward a prism by DM. The prism is used to separate the fundamental from the TH beam. Finally, the TH beam is measured by detector D2. A reflected fundamental beam from DM that passes through lens L3 is collected by detector D1 to monitor the fundamental pulse energy.

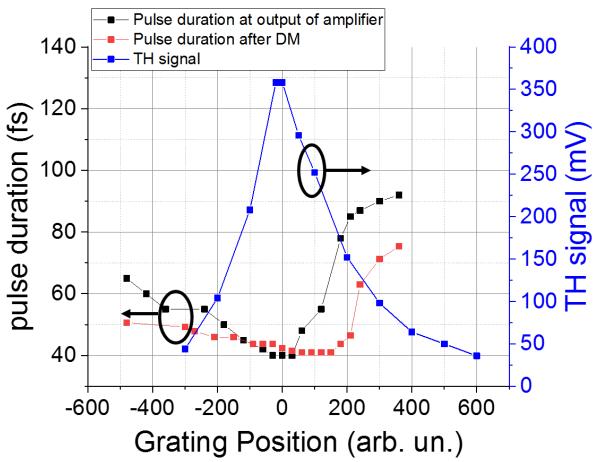

Figure 3.6: The pulse duration of the amplifier at its output (black) and after dichroic mirror (DM) (red) relative to the position of the grating in the pulse compressor inside the amplifier. The TH signal (blue) from sample O3R (see Appendix. C) peaks at the minimum pulse duration.

The beam size of the fundamental beam is measured using a beam profiler as shown in Fig. 3.7 configuration. The distance from the output of amplifier to the

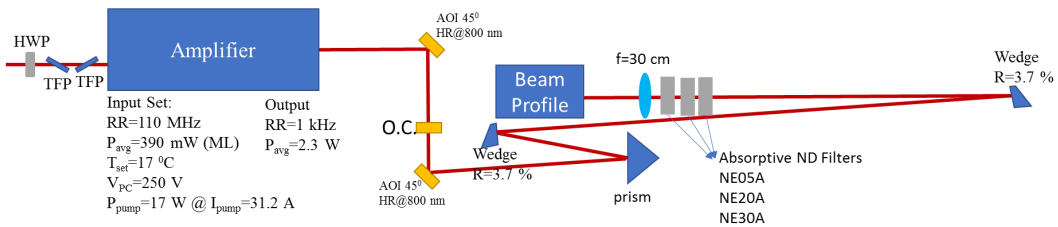

Figure 3.7: Experimental setup to measure the beam profile. HWP: half wave plate. TFP: thin film polarizer. Amplifier: max input average power P_{avg} = 390 mW, temperature of base holder of Ti:Sapphire crystals T_{set} = 17 ^{0}C, bias voltage of Pockell Cell (PC) V_{PC} = 250 V, average power of pump inside amplifier P_{avg} = 17 W at current I_{pump} = 31.2 A. AOI: angle of incidence. O.C.: output coupler. Neutral density filters NE05A, NE20A, NE30A have transmission 1/3, 1/100, and 1/1000, respectively.

focusing lens ($f = 30$ cm) is 2.5 ± 0.1 m. The fundamental beam passes through an output coupler (O.C.), and reflects back from three glass surface to attenuate the beam enough to not cause any kind of Kerr lensing due to high peak power in the absorptive neutral density (ND) filters. The measured beam profile and the beam waist as a function of position are shown in Fig. 3.8 with the trend line expected from Gaussian beams.

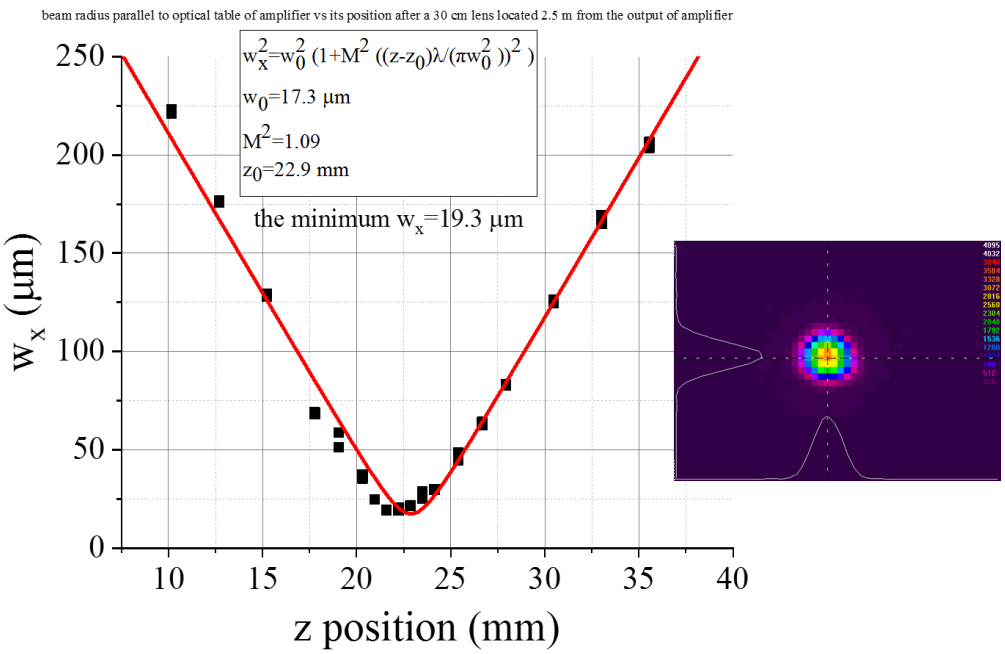

Figure 3.8: The profile of the amplifier beam after an $f = 30$ cm lens placed 2.5 m from the output of the amplifier. w_x is the Gaussian beam radius in x direction (parallel to optical table). z: is the position of the beam profiler. w_0: beam waist obtained from fit of Gaussian beam to intensity profile at different z. $\lambda = 815$ nm: central wavelength of fundamental beam. M^2: beam quality factor.

3.3 Summary

In summary, the spatial and temporal profile of the femtosecond oscillator and amplifier are characterized. The oscillator output is a pulse train with repetition rate of 110 MHz, and pulse duration of 55 fs, and pulse energy of 10 nJ centered at 787 nm. The beam waist of fundamental beam after 5 cm focusing lens is 6.2 ± 0.2 μm on the sample. The amplifier output is 1 kHz short pulses of 42 fs with pulse energy of 2.3 mJ, centered at 815 nm. The beam waist of fundamental beam after 30 cm lens is 17 μm.

Chapter 4

Design of Frequency Tripling Mirrors and Scaling of Frequency Conversion - Quasi-monochromatic Approach

In this chapter, we will discuss aperiodic structures called frequency tripling mirrors (FTMs) [24] based on three favorable design concepts that address maximum TH output and efficiency. It will be shown that TH generation scales exponentially with number of layers in the design. In addition, other features of designs like bandwidth, linear loss, selection of materials, and the effect of film thickness fluctuations due to the deposition process, are studied.

4.1 Basic Architecture of FTMs

An FTM is a dielectric multi-layer structure that converts incident laser radiation to TH in reflection, see Fig. 4.1. A matrix formalism can be applied to predict the TH for a given sequence of N (typically) high and low index coatings characterized by its vector of thicknesses $\vec{d}$, complex refractive indices $\vec{n}(\omega)$ and nonlinear susceptibilities of third order $\vec{\chi}^{(3)}$ [30]. The respective $(N+1)$th vector components describe the substrate properties. Note, there is no required condition on periodicity of layer thicknesses inside the stack. In addition, we designed FTMs at normal incidence. The optimization process of designs for high TH output determines the thickness of each individual layer.

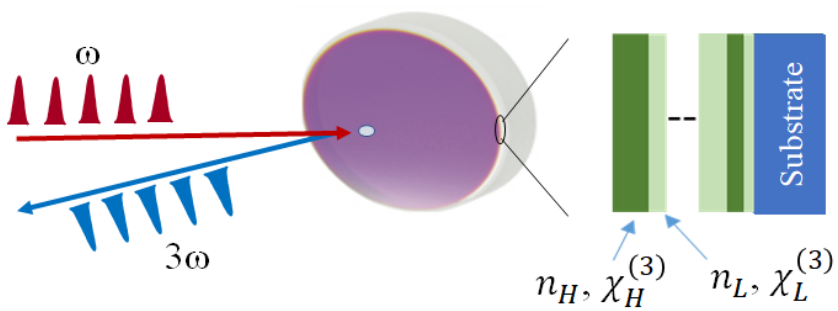

Figure 4.1: Schematic diagram of a frequency tripling mirror.

The TH field in reflection can be regarded as phasor sum of the fields generated in each layer and propagated out of the structure [30]. For a given number of layers, the optimum design is one that maximizes the TH field through a combination of field enhancement in the stack and global compensation of phase mismatch so that fields add in phase.

To design an FTM one can consider three basic approaches that we label A, B, and C.

Design A refers to a layer sequence that produces the largest TH for given incident

laser parameters (fluence, intensity) irrespective of what the field parameters are inside the stack.

Design B produces the largest TH if we compare different designs and assume that the maximum fluence reached inside the stack is the same. This, of course, requires different incident fundamental fields. Design B has practical relevance if the task is to produce maximum TH energy S_{TH} for given input energy of the fundamental S_F. In practice, one would decrease the beam spot size until the maximum field (or fluence) inside the stack reaches a critical value F_{crit}. This critical value can be associated with material damage or with the onset of material modifications that compromise the performance of the nonlinear element.

Design C maximizes the conversion efficiency $\eta = S_{TH}/S_F$. Again, because of the practical relevance, we compare mirrors for the same maximum field reached inside the stack, $E_{F,max}$. Maximum conversion efficiency is obtained when the incident fluence $E_{F,max} = E_{F,crit}$.

The TH energy measured in reflection by an integrating detector can formally be written as

$$S_{TH} = q\left(\vec{d}, \vec{n}, \vec{\chi}^{(3)}\right) |E_{F,0}|^6 \int dt \int d^2r |\hat{E_F}(t,r)|^6 = q_A |E_{F,0}|^6 K, \tag{4.1}$$

where q_A is the figure of merit of the stack for THG for designs of type A, $E_{F,0}$ is the peak incident field amplitude, $\hat{E_F}$ describes the incident field's temporal and spatial shape with its maximum $\hat{E_F}(0,0) = 1$, and K is the numerical value obtained from the time and spatial integration. These designs are of practical importance in situations where $E_{F,max} < E_{F,crit}$ and cannot be increased. In designs of type A, the q_A parameter is maximized at given $\vec{n}$, and $\vec{\chi}^{(3)}$ by optimizing $\vec{d}$. The parameter $q_A = |E'_{0,l}/E'^3_{F,0,r}|^2$, where $E'^3_{F,0,r}$ and $E'_{0,l}$ are the incident fundamental and produced TH fields at the air/stack interface. See appendix E for analytical relations of the

fields.

For designs of type B it is convenient to re-write Eq. (4.1) in terms of the maximum field amplitude reached inside the layer stack, $|E_{F,max}|$.

$$S_{TH} = q_A \left| \frac{E_{F,0}}{E_{F,max}} \right|^6 |E_{F,max}|^6 K = q_B |E_{F,max}|^6 K, \tag{4.2}$$

where $q_B = q_A / f^6$ with $f = |E_{F,max}/E_{F,0}|$ being the field enhancement factor. Note that f is also a function of the stack parameters. Designs of type B maximize q_B. We can estimate the maximum possible TH signal using for example $|E_{F,max}| = 0.9|E_{F,crit}|$. As mentioned previously, these designs are relevant where the input field can always be increased, for example by tighter focusing.

The conversion efficiency is obtained by dividing Eq. (4.2) by the fundamental energy $S_F = K'|E_{F,0}|^2$:

$$\eta = \frac{S_{TH}}{S_F} = q_A \frac{1}{f^4} |E_{F,max}|^4 K'' = q_C |E_{F,max}|^4 K''. \tag{4.3}$$

Here $K'' = K/K'$ is a numerical constant. Designs of type C maximize q_C and produce the largest conversion efficiency for given $|E_{F,max}|$.

In this work we will refer to designs for which the q parameters are maximized for a certain wavelength of the fundamental input. The so obtained stacks exhibit finite bandwidth $\Delta\lambda$ (Full width at half maximum of TH energy relative to wavelength) and pulses as short as 55 fs have been converted [24]. The design process involves the calculation of the TH for given stack parameters and a computer optimization that seeks the layer thicknesses $\vec{d}$ for maximum output, see [30]. Other constraints like robustness with respect to thickness fluctuations can be incorporated. In some designs an Al layer was sandwiched between substrate and dielectric stack.

The reflection of four pairs of Hafnia/Silica with quarter wave (QW) thickness (the total thickness is 920 nm) is equivalent to reflection from an Al substrate. So,

in practice, instead of using more Hafnia/Silica layers, a single Al substrate could be used in the design of an FTM.

We will describe sequences of Hafnia and Silica layers, which are typical dielectric materials used for optical coating stacks.

The dispersion of their complex refractive indices $n(\lambda)$ were measured in LZH Hannover by our collaboration partners who also manufactured the FTMs.

The wavelength for the incident light was 787 nm. Table 4.1 shows the complex refractive index $n = n_r + in_i$ for our materials of interest.

Table 4.1: **Complex refractive index n, third-order susceptibility $\chi^{(3)}$ and coherence length of the films used. The $\chi^{(3)}$ values are from [4], where $\gamma = 2 \times 10^{-22}$ $\mathbf{m^2/V^2}$ is $\chi^{(3)}$ of fused silica.**

material	n (@800nm)	n (@267nm)	L_{coh} (nm)	$\chi^{(3)}$
HfO_2 (film)	1.9547	2.1488	676	20.3γ
	$-0.0004i$	$-0.0058i$		
SiO_2 (film)	1.4755	1.5342	2234	γ
Al	2.6052	0.219	55	8γ
	$-8.527i$	$-3.16i$		
Suprasil	1.4542	1.5015	2768	γ

The TH calculations do not take into account the depletion of the pump. For the results to describe experimental conditions the laser input parameters must therefore be chosen so that the conversion efficiency is not larger than 10% - 20%.

4.2 The Search Space for Optimum Designs

The q parameter is a function is a function of $\vec{d}$ ofr given $\vec{n}$. We assume the thickness of each layer regardless of any deposition limit, is only confined by the coherence length, l_{coh}. The coherence length is the length that the optical path difference of

fundamental and TH fields has π phase shift, and the energy of generated TH couples back to the fundamental beam. However, in multilayer thin films the length for maximum TH conversion efficiency will change due to fundamental field interference. The optimization wavelength of the fundamental beam of designs is set to 787 nm, which corresponds to a TH wavelength of 262.3 nm in free space. The coherence lengths are 680 nm, 2.24 μm for Hafnia and Silica, respectively. The thickness of the layers have an uncertainty of D_l, which ranges from less than a nanometer up to few nanometers depending on the deposition technique. We will later discuss the effect of random thickness fluctuations. Using D_1 as minimum thickness increment, each layer can take on $(l_{coh}/D_l)^N$ values. As the number of layers increases, the search space grows exponentially with number of layers. Therefore the computer search algorithm will not be able to find the optimum design for a certain number of layers in a short time, unless we have a good initial guess of the thickness of each layer.

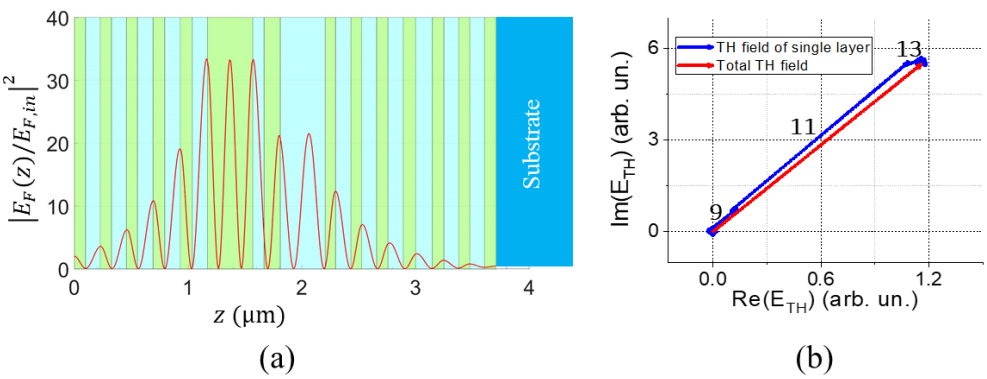

Figure 4.2: (a) Standing fundamental wave intensity distribution in a multi-layer stack (green is Hafnia, and blue is Silica) of design A for $N = 27$ dielectric layers on a fused silica substrate. (b) Phasor sum of the TH field components in reflection outside the FTM. The numbers on top of the blue arrows show at which layer the TH field originates (layers are numbered starting from the air interface). The other field components are too small to be seen in this phasor diagram

The computer search and optimization of an FTM requires as input the number

of layers N, constraints on individual layer thicknesses, the complex refractive index vector, the $\chi^{(3)}$ vector. The optimization begins from a random set of thicknesses (or guesses based on previous deisgns) and then tries to maximize the TH energy by finding the aproppriate thickness vector. We used the Genetic algorithm in MATLAB to look for the solution. In general, it starts from random initial populations (in this case a set of values for the thicknesses), then evaluates the TH energy for all of them, and compares the TH values to keep the populations that have larger values. Next, it generates new populations based on successive sets, and continues this process to reach the best population. It should be noted that there are many knobs to control this optimization flow, for example see the online MATLAB help. Finally, the output of the optimization is a set of thicknesses for the stack $\vec{d}$, which are used to fabricate the FTM. As an example, Fig. 4.2(a) shows a design, where the first layer on top of the substrate is a Hafnia film, and followed by a Silica film, and this alternates up to the output interface.

Note, since the search space increases exponentially with number of layers N, it is crucial to come up with a design that has the potential to turn into a design after optimization with decent TH conversion efficiency.

4.3 Design A

Figure 4.3 shows the (normalized) figure of merit q_A as a function of the number of layers N obtained from the computer simulation. For each N the computer search was repeated multiple times and the largest q_A value is displayed.

For the dielectric stack on the fused silica substrate the TH signal ($\propto q_A$) is expected to increase exponentially with N, see curves a1 and a2. For designs with an Al layer sandwiched between substrate and dielectric stack (or an Al substrate) the behavior of $q_A(N)$ is qualitatively similar, but with a larger exponent, lets call it

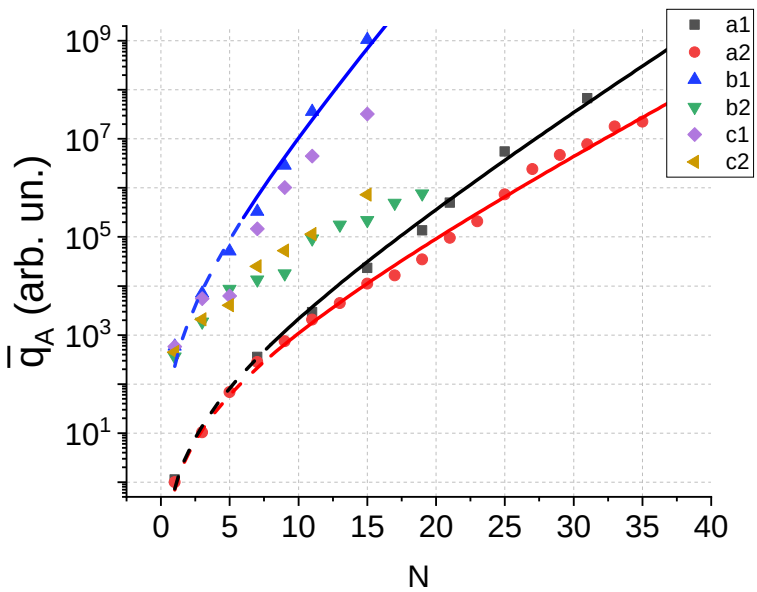

Figure 4.3: Conversion parameter $\bar{q}_A$, see Eq. (4.7) (design A) as a function of the number of dielectric layers on (a) the substrate (fused silica) and (b) an aluminum layer (30 nm) deposited on the substrate (fused silica). a1 (a2) and b1 (b2) neglect (take into account) the imaginary part of the refractive index. c1(c2) takes into account imaginary part of dielectric layers(aluminum) and ignoring the imaginary part of aluminum(dielectric layers). The data points are from the computer search, the lines represent analytical models, see text. The dashed parts in regions of small N are beyond the validity range of the model, see Eq. (4.7).

κ. In both cases the losses decrease κ. c1 data points indicate that absorption in the dielectric layers lower κ. However, κ is still quite large compared to case c2 where a perfect reflector for both fundamental and TH wavelengths is replaced with Al.

A closer inspection of these designs shows that most of the TH signal is generated in just a few layers sandwiched between structures that resemble mirrors. Both mirrors are highly reflective at fundamental wavelength, meanwhile mirror on top of substrate is highly reflective at TH wavelength, too. These "mirrors" form Fabry-Perot resonators that lead to field enhancements. The field distribution in the stacks

is exemplified in Fig. 4.2(a).

The phasor diagram shows how the TH fields from each layer add up at the air/stack interface. Layers with larger $\chi^{(3)}$ (HfO_2) and field enhancement generate TH fields (blue vectors) that contribute the most to the total TH field (red vector). The other layers still have important functions - they produce desired linear properties like high reflection of fundamental and TH, and produce optimal relative phases so that the largest TH field components add constructively.

The optimization decides how many layers should be used to form the two mirrors. More layers increase the reflectance and subsequently the field enhancement, but reduce the number of layers in the region of the maximum electric field that contribute most to the TH signal. This simple understanding of the function of the layer stack as frequency converter leads naturally to a possible analytical model to explain the scaling $q_A(N)$. We will now try to understand these computer results using such a simple model.

Let us assume that the N layers are divided into two quarter-wave stacks, each with $M = (1-a)N/2$ films, and aN layers in between that generate TH radiation and take advantage of the field enhancement f. The generated TH signal is proportional to

$$S_{TH} \propto (aN)^2 f^6 |E_{F,0}|^6. \tag{4.4}$$

The field enhancement factor f is controlled by the reflectivity r of the two mirrors $f^2 = (1+r)/(1-r)$ [31]. Using the known relationship $r(M) = (\Delta^M - 1)/(\Delta^M + 1)$ for a quarter-wave stack [28], where $\Delta = n_H/n_L$ and n_H, n_L is the refractive index of the high-index and low-index film, respectively. Note, the ratio n_{sub}/n_{air} is ignored in $r(M)$, because it doesn't have a large impact on S_{TH}.

Assuming the TH field in a single layer is proportional to the cube of the maximum

fundamental field inside the stack, we obtain

$$S_{TH} \propto (aN)^2 \Delta^{3(1-a)N/2} |E_{F,0}|^6, \tag{4.5}$$

where the N^2 dependence arises from the fact that the TH field is linearly proportional to the total layer thickness. Comparison of Eq. (4.1) and Eq. (4.5) yields

$$q_A \propto (aN)^2 \Delta^{3(1-a)N/2}. \tag{4.6}$$

If we include absorption, the field enhancement $f_{abs}^2 = f^2 \times (1-r^2)^2/(1-r^2 e^{-\beta_F})^2$, where $\beta_F = \alpha a N d$ is the small-signal absorption coefficient for the fundamental field for one round trip.

Because $\beta_F << 1$, the field enhancement can be approximated as $f_{abs}^2 = f^2/(1 + \beta_F \Delta^M/4)^2$. In addition, the absorption of the TH radiarion attenuates q_A by a factor $e^{-\beta_{TH}}$, where $\beta_{TH} = \alpha_{TH} d N/2$.

For simplicity we introduce normalized quantities $\bar{q}_A(N) = q_A(N)/q_A(1)$ and obtain

$$\begin{aligned} \log(\bar{q}_A) \propto \;& 2\log(N) \\ & + N\left[\frac{3(1-a)}{2}\log(\Delta) - d\log(e)\left(\frac{\alpha_{TH} + 3a\alpha_F \Delta^{\frac{(1-a)N}{2}})}{2}\right)\right]. \end{aligned} \tag{4.7}$$

For large N the second term dominates and describes an exponential increase of $\bar{q}_A$ seen in Fig. 4.3. In the absence of losses the slope of $\log(\bar{q}_A)$ is controlled by a single material parameter Δ. For example, an 1% increase of Δ at $N = 25$ will lead to 28% increase in q_A. Losses reduce the slope and for our situation are dominated by α_{TH}, cf. Table 4.1. The lines shown in Fig. 4.3 were obtained by fitting model Eq. (4.7) to the simulation results. The fitting parameter is $a = 0.1$ (in case of Fig. 4.3 a1, no losses) and $a = 0.21$ (in case of Fig. 4.3 a2, with losses).

To obtain the corresponding expression for the case of a perfect reflector (perfect metal) at the bottom of the stack, cf. data b1 in Fig. 4.3, we just replace one of the quarter-wave stacks with a perfect reflector with reflectance of $R = 1$ at both fundamental and TH wavelengths. The prefactor of $\log(\Delta)$ in Eq. (4.7) now becomes $3(1-a)$. Good agreement with the computer search data was obtained for $a = 0.19$.

4.4 Design B

If the maximum intrafield is constrained to the damage threshold, the optimum design is one with a larger number of layers with similar intrafilm peak intensity that contribute to the TH compared to design A. Because of the assumption that the critical field can always be reached by changing the input (focusing and / or fluence) the field enhancement inside the stack is less important.

The structure is essentially one mirror with TH generating layers on top. These layers act as an AR coating stack and see several periods of the standing intensity distribution with similar peak amplitudes. The field enhancement is considerably lower than in design A for the same N but more layers contribute to the TH. The mirror on top of the substrate is highly reflective for the TH, too. An example for $N = 17$ is shown in Fig.4.4.

Figure 4.5 shows the scaling of the conversion parameter q_B with layer number N with and without linear absorption losses. In design B, the fundamental field enhancement is not as strong as in design A, but many layers contribute to THG equally. It implies that in these designs, the strength of the TH field increases linearly with the total thickness of the layers that generate most of the TH field.

Lets take the reflectivity of the mirror on top of the substrate to be $r(N)$. It is weakly dependent on the number of layers based on the reflectivity evaluation of the

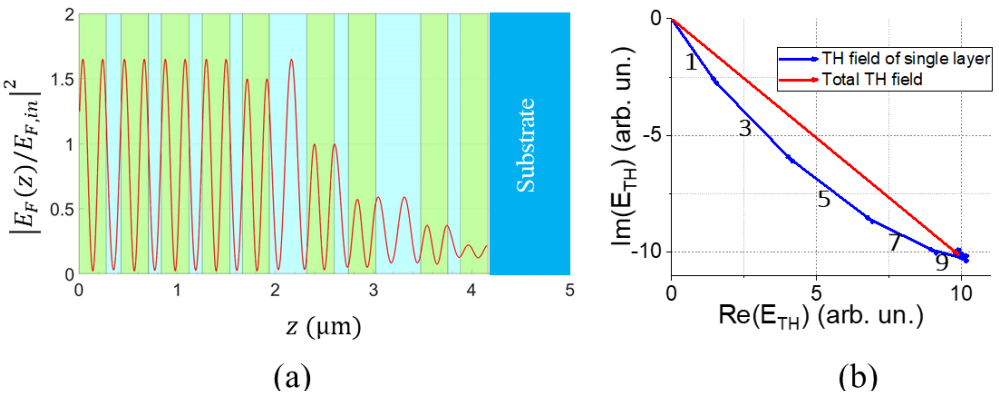

Figure 4.4: (a) Standing fundamental wave intensity distribution in a multi-layer stack (green is Hafnia, and blue is Silica) of type B for $N = 17$. The layers larger than $z > 2.2$ μm, form a mirror with a field reflection r (b) Phasor sum of the TH field components in reflection outside the FTM. The numbers on top of the blue arrows show at which layer the TH field originates (layers are numbered starting from the air interface). The other field components are too small to be seen in this phasor diagram

mirror structure in the optimum designs. Because with increase in N the reflection of the mirror on top of substrate at both fundamental and TH wavelengths approaches 1. Since the optimum B designs are not resonant structures, as long as N is large enough a further increase in N does not affect the field enhancement significantly as we saw earlier in A designs. The field enhancement is proportional to $(1+r(N))E_{F,0}$ in an AR structure, which at first order is assumed to be fixed. The TH field that is generated in an AR structure with aN layers is linearly proportional to the total thickness of layers. So, we can write,

$$q_B \propto (aN)^2(1+r(N))^6. \tag{4.8}$$

Absorption in these designs at the fundamental wavelength is negligible unlike type A designs, because they are not resonant designs. By non-resonant, we mean the fundamental field propagates through these layers only twice (forward and backward). Absorption at the TH wavelength can be considered by multiplying $e^{-\beta_{TH}}$, where $\beta_{TH} =$

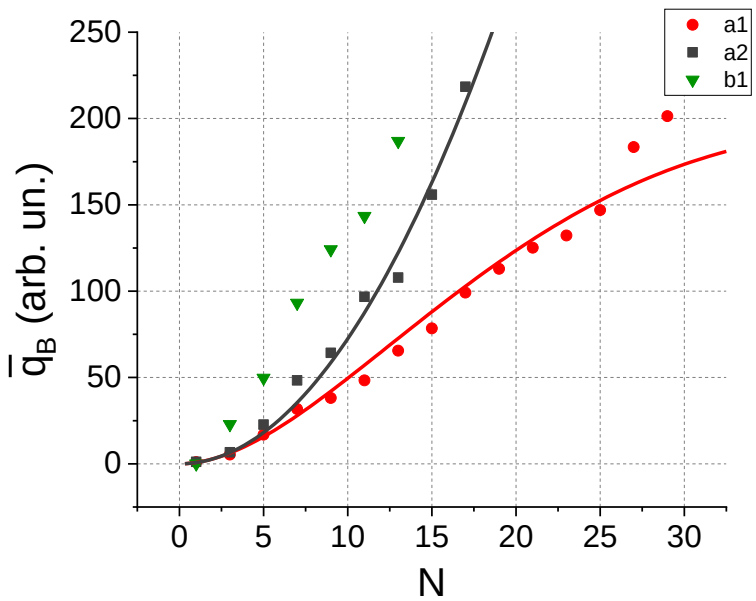

Figure 4.5: $\bar{q}_B$, see Eq. (4.9), (design B) as a function of the number of dielectric layers on (a) the substrate (fused silica) and (b) an Al layer (30 nm) deposited on the substrate (fused silica). a1 (a2) and b1 take into account (neglect) the imaginary part of the refractive index. The data points are from the computer search, the lines represent analytical models, see text. The regions of small N are beyond the validity range of the model Eq. (4.9).

$\alpha_{TH} daN/2$. After introducing the normalized quantity $\bar{q}_B(N) = q_B(N)/q_B(1)$, we find

$$\log(\bar{q}_B) \propto 2\log(N) + 6\log(1 + r(N)) - ad\alpha_{TH}\log(e)N/2 \tag{4.9}$$

Since the reflectivity of mirrors on top of substrate $r(N)$ is only weakly dependent on N, q_B increases parabolically with the number of layers. Absorption of the TH is a strong function of N, and it surpasses parabolic growth in designs with lager number of layers.

The insertion of an Al layer between substrate and the dielectric layers increases q_B. This is because the Al layer replaces the layers forming a mirror on the substrate. The results is that with the same number of total layers, the design reaches a larger q_B relative to the all-dielectric case.

4.5 Design C

Designs A and B are optimized for THG at the same incident and intrafilm electric field, respectively. Type C designs present structures optimized for conversion efficiency of THG, when the intrafilm maximum fluence is less than the critical fluence. Based on the simulation results, the structure of optimized C designs favors fundamental field enhancement like A designs.

Mirrors on both ends of the stack are reflective at the fundamental, while only the mirror on top of the substrate is highly reflective at the TH. Figure. 4.6 shows the fundamental field intensity distribution and the phasor diagram of TH fields for design C with $N = 27$.

Optimized designs for q_C are shown on Fig. 4.7. We followed the A type design modeling approach here using Eq. (4.5), and the fact that in the C type designs the conversion efficiency is the figure of merit in the computer optimization.

The resemblance of these designs with design type A enable modeling $q_C(N)$ using the same assumptions and relations as before. Using Eqs. (4.3) and (4.5) and $f^2 = \Delta^M$, we find

$$q_C \propto (aN)^2 \Delta^{(1-a)N/2} \tag{4.10}$$

The effect of absorption is the same as in type A designs. For the normalized figure

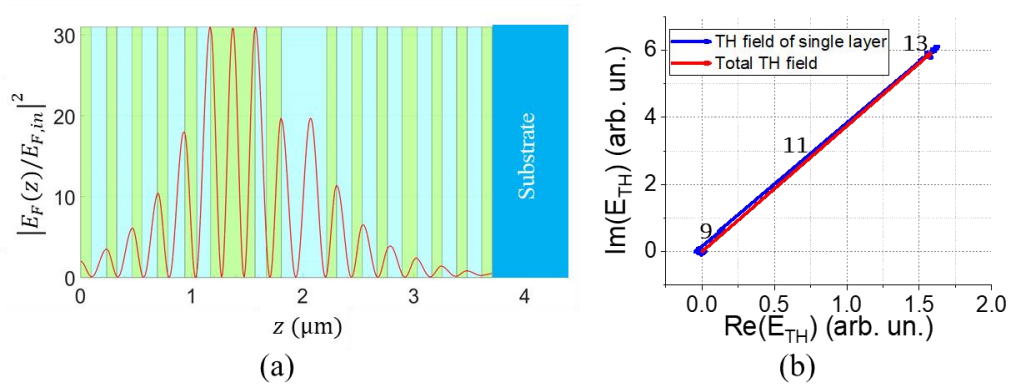

Figure 4.6: (a) Standing fundamental wave intensity distribution in a multi-layer stack (green is Hafnia, and blue is Silica) of type C for $N = 27$. (b) Phasor sum of the TH field components in reflection outside the FTM. The numbers on top of the blue arrows show at which layer the TH field originates (layers are numbered starting from the air interface). The other field components are too small to be seen in this phasor diagram

of merit $\bar{q}_C(N) = q_C(N)/q_C(1)$ we obtain

$$\begin{aligned}\log(\bar{q}_C) \propto \quad & 2\log(N) \\ & + N\left[\frac{(1-a)}{2}\log(\Delta) - d\log(e)\left(\frac{\alpha_{TH} + 3a\alpha_F\Delta^{\frac{(1-a)N}{2}})}{2}\right)\right]. \qquad (4.11)\end{aligned}$$

Figure 4.7 shows a fit of this model to the simulation results. It is obvious how absorption in the dielectric layers reduces the slope of $\bar{q}_C(N)$. Again,an Al layer could advantageously replace the mirror-forming layer on top of a substrate.

4.6 Detailed Study of the THG Inside an FTM

In this section, the effect of the fundamental field distribution on THG in a single layer is discussed. The idea is to study what parts inside an individual layer (for example 9th from air interface in A type design in Fig. 4.8), generates most of the TH

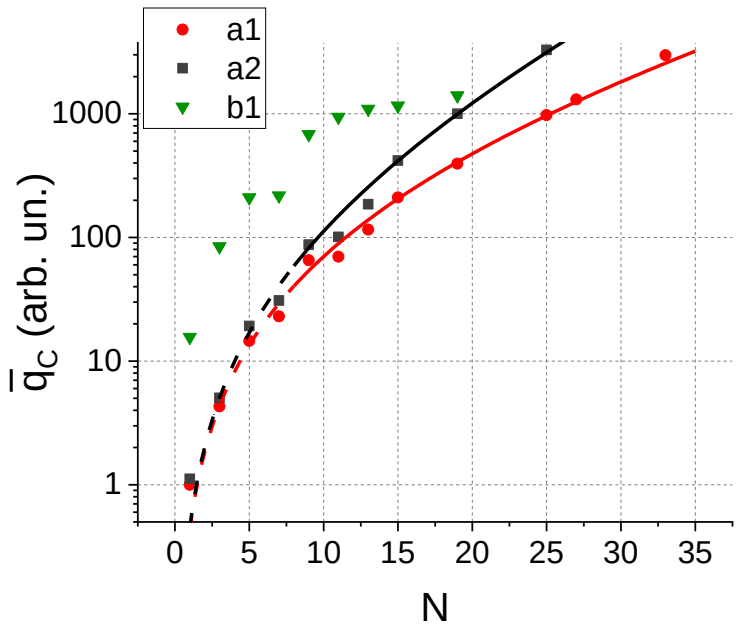

Figure 4.7: Normalized conversion efficiency $\bar{q}_C$ for design C, see Eq. (4.11), as a function of the number of dielectric layers on (a) the substrate (fused silica) and (b) an Al layer (30 nm) deposited on the substrate (fused silica). a1 (a2) and b1 (b2) neglect (take into account) the imaginary part of the refractive index. The data points are from the computer search, the lines represent analytical models, see text. The dashed parts in regions of small N are beyond the validity range of the models.

signal. We took the layer nine from air interface (left) of design in Fig. 4.2. The $\chi^{(3)}$ of all layers are set to zero, so there is no TH field at the output due to each layer. Then, in the ninth layer (hafnia) a 1-nm film slice with nonzero $\chi^{(3)}$ is introduced. Its position is varied from 0 to the thickness of layer nine. The TH signal relative to the position of this slice is shown in Fig. 4.8.

We see that almost negligible TH is generated in the initial part of the ninth layer, while the peak of THG happens when the thin probe slice is at position 30 nm

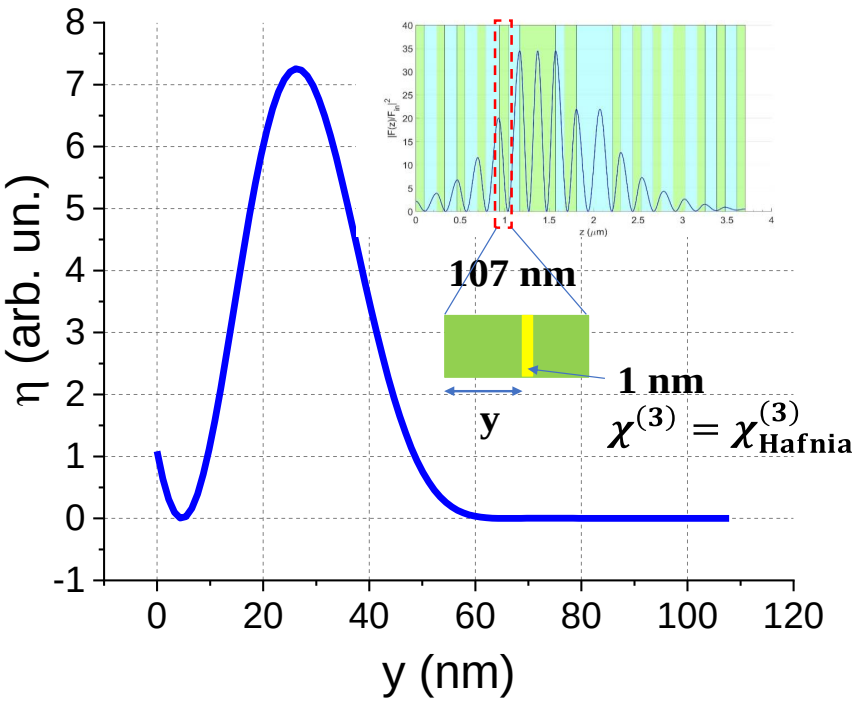

Figure 4.8: The conversion efficiency of THG from a 1-nm thick probe layer inside layer 9 of an FTM with $N = 27$ (green is Hafnia, and blue is Silica). The x-axis shows the position of the probe layer. It was assumed that $\chi^{(3)} = 0$ in all layers, except in the thin probe layer. Note, the fundamental field peaks in layer 9 at $y = 0$, which is different from the position of the probe layer producing the maximum TH signal.

from interface, where the fundamental intensity is 25% lower than its value at the interface. It points to the fact that maximum THG does not happen always at the position with highest fundamental field enhancement. Because in each layer there are two fundamental waves that propagate in opposite directions their superposition produces the total fundamental field. This results in TH fields that have four terms see Eq. (E.11), and (E.12). Note appendix E presents the monochromatic model of THG in a stack of thin films. For example, for the TH that is generated in forward

direction, compared to the term that includes the third power of the fundamental field propagating in forward direction, the two cross terms produce comparable contributions. This is despite of them having a much larger phase mismatch. This controls the dependence of THG within the film in addition to the field enhancement.

In an individual layer that has only one fundamental peak, most of the TH is generated in a small range inside the layer. Now we want to study the case that an individual layer contains multiple maxima of the fundamental standing wave. Let's take the 11th layer from the air interface in Fig. 4.2, where there are three peaks of fundamental. This is also the layer that generates the largest part (above 50%) of the output TH of this FTM.

Figure. 4.9 shows the TH variation relative to the position of the probe layer. The peak THG happens near the three fundamental peaks. This example points out that the entire layer is not required to generate TH. The TH fields are generated in 60 nm, which is below 10% of the coherence length.

In summary, maximum output TH fields are not always generated where the fundamental standing wave peaks, and only a small fraction of each film contributes to THG. It is an important result, because based on discussion about the max THG at damage threshold fluence, see Fig. 2.4, in bulk form, Alumina generates the largest TH over the coherence length. However, in a stack of thin films we see from above discussion that the THG in thin film layers does not grow with thickness of layers up to the coherence length. So, the above discussion puts an upper limit on the THG inside a layer in a stack and guides toward better material selection. For a wavelength of 800 nm, Hafnia is better than Alumina. In addition, in certain cases these findings may save computer time because we can constrain the search space more.

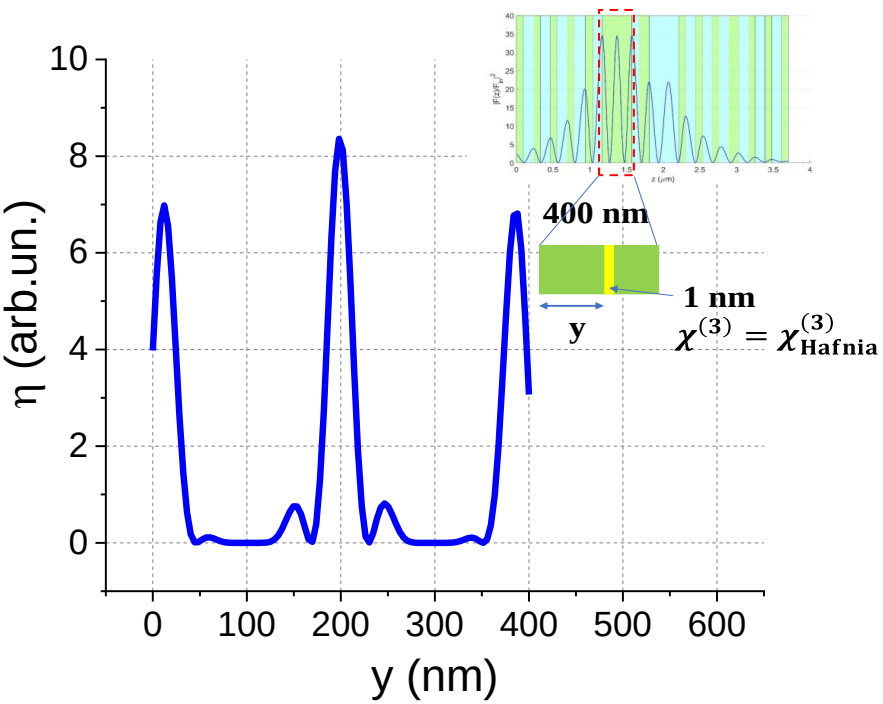

Figure 4.9: The conversion efficiency of THG from a 1-nm thick probe layer inside layer 11 of an FTM with $N = 27$ (green is Hafnia, and blue is Silica). The x-axis shows the position of the probe layer. It was assumed that $\chi^{(3)} = 0$ in all, but layer 11. Note the locations of the fundamental intensity peaks in layer 11 are different from the position of the probe layer producing the maximum TH signal.

4.7 Fluctuations of the Film Parameters

In the fabrication process of FTMs, there is always an uncertainty in the thickness of the layers during the deposition process. Therefore, it is necessary to assess the THG dependency on thickness errors.

To compare the designs, a parameter P_{50-100} is used to illustrate the robustness of design to thickness errors. We start from a single initial (optimized) design characterized by a thickness vector $\vec{d}$. We next generate 1000 designs from this initial

design by introducing a random thickness vector $\vec{d} + \vec{\Delta}d$. Here each component $\Delta d_i/d_i$ is a random number from the interval $[-1, 1]$. In other words, each layer thickness is allowed to fluctuate randomly by up to $\pm 1\%$, which is a typical number for the actual deposition process.

P_{50-100} is the probability that a such generated new design will produce a TH signal of at least 50% of the original design. Figure. 4.10 shows this probability P_{50-100} as a function of the number of layers N in the FTM.

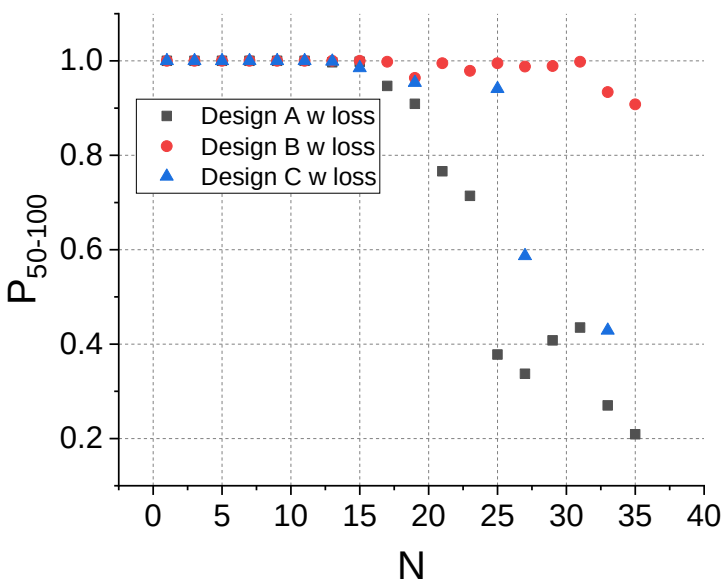

Figure 4.10: Probability P_{50-100} that random layer thickness fluctuations of $\leq 1\%$ lead to THG efficiencies not smaller than 50% of those of the original optimized design, as a function of the number of layers. q_A was analyzed for the simulation and 1000 designs with random thickness vectors were used.

The probability P_{50-100} of optimum A, B, and C designs decreases with increasing number of layers N, and consequently with increasing q. There are two reasons

for this behavior. (1) Deviations from the optimum conditions (optimum thickness vector) result in a lower fundamental field enhancement. This is more pronounced in type A and C designs compared to type B FTMs. (2) The phases of the TH fields originating in different fields deviate now more from the optimum condition (constructive interference).

To be more specific let us consider as an example an optimized FTM with $N = 15$ and a figure of merit q_0. The lowest q value of 1000 randomly generated FTMs using the procedure explained before was $0.67q_0$ at the original design wavelength (787 nm). The field intensity enhancement was 25% less compared to the optimized FTM. This modified mirror showed a maximum conversion at 782 nm, where the corresponding q value was still 10% lower than q_0. In addition, the generated TH fields at the output interface(air/stack interface) due to each layer have larger phase mismatch with each other.

4.8 The Design in Transmission

So far only designs in reflection have been studied for THG. In this section, we will study designs that are optimized for maximum THG in transmission. A well-known approach is quasi-phase matching (QPM) [7], that is used widely for example in crystals. Here, after each coherence length, the sign of $\chi^{(3)}$ of crystal is flipped. In this way, the generated TH after the coherence length can be in phase with the TH wave generated in $z = l_{coh}$, where l_{coh} is the coherence length of the TH process.

The TH energy is proportional to

$$U_{TH} \propto |E_{TH}|^2 \propto \left(\frac{\chi^{(3)} l_{coh}}{n_{\lambda/3}} \right)^2 \tag{4.12}$$

Equation (4.12) indicates that the maximum THG in a medium with coherence length (l_{coh}) depends on third order electrical susceptibility ($\chi^{(3)}$), and refractive

index at TH wavelength ($n_{\lambda/3}$). Since, in a multilayer stack with two materials that the sign of their $\chi^{(3)}$ are not opposite, the relative generated TH fields are important. Because, total TH fields will be the sum of TH fields that are generated in the whole pair of Hafnia/Silica. The value of $\chi^{(3)} l_{coh}/n_{\lambda/3}$ for Hafnia and Silica are in the same order, see Table. 4.1. So, while the significant TH is generated in Hafnia, the TH that later is generated in Silica would cancel most part of it.

Table 4.2: **Coherence length (l_{coh}), phase mismatch ($\Delta k = 3k - \kappa$) of k fundamental and κ TH, and $\chi^{(3)}$ of Hafnia, Silica, and air at 790 nm along with the refractive index ($n_{\lambda/3}$) of them at 263.3 nm are shown. The product of $\chi^{(3)} l_{coh}/n_{\lambda/3}$ is also shown as a comparison for THG over a coherence length. The $\chi^{(3)}$ value for bulk fused silica is from [4].** $\gamma = 2 \times 10^{-22}$ **m^2/V^2.**

material	l_{coh} (μm)	Δk (μm^{-1})	$\chi^{(3)}$	$n_{\lambda/3}$	$10^{28}\chi^{(3)} l_{coh}/n_{\lambda/3}$
Hafnia (film)	0.54	5.824	20.9γ	2.22	10.2
Silica (film)	3.27	0.96	γ	1.53	4.3
Air	6480	4.8×10^{-4}	$2.85 \times 10^{-4}\gamma$	1.00	3.7

In a stack of amorphous, dielectric films, there is no change in the sign of $\chi^{(3)}$. Since the Silica layer has a $\chi^{(3)}$, which is 5% of the $\chi^{(3)}$ of Hafnia, the Silica layers are implemented as layers that phase mismatch of fundamental and TH electric fields reach π phase shift, so in the TH which is going to be generated in the next Hafnia layer will be in phase with TH field generated in the latter Hafnia layer.

It means, for example, in case of a single Hafnia/Silica pair(each layer is thick as a coherence length) and assumption of equal fundamental electric field, the net THG is 18% of TH value in a single Hafnia layer with thickness of one coherence length. In other word, more than 5 pairs of Hafnia/Silica are required to produce TH lager than a single Hafnia layer. We will call such a structures that thickness of layers is a coherence length, QPM-like stacks hereinafter of current section.

As an example, Fig. 4.11 shows a transmission design optimized based on the QPM-like concept. In optimization flow, QPM-like (QPM in Fig. 4.12(a), and

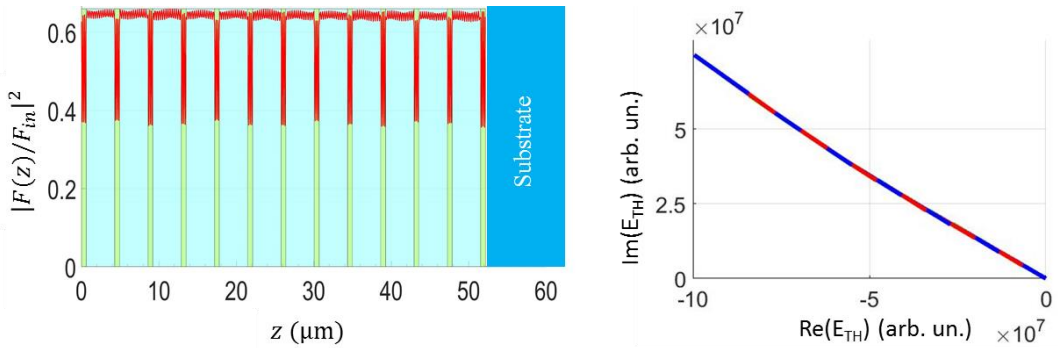

Figure 4.11: Intensity distribution (green is Hafnia, and blue is Silica) and phasor diagram of a QPM-like stack with $N = 25$. The phasor diagram indicate the contribution from Hafnia (blue and red lines) and silica (green lines). The reason that green lines are not recognizable is that phasors due to Hafnia is on top of them (phasors due to Hafnia are shown in red and blue to distinguish the layers). The TH produced inHhafnia, despite the much lower $\chi^{(3)}$, because the Silica layer is much thicker than the Hafnia film.

4.12(a)) design is given as a start point to optimization algorithm, and let the computer to search for the best solution. The final result of optimization (optimized QPM in Fig. 4.12(a), and 4.12(b)) looked similar to initial QPM-like design, where variation in thicknesses was below a percent in all the layers. The fundamental field enhancement is similar in Hafnia and silica layers. The phasor diagram Fig. 4.11 shows that each Hafnia layer has equal contribution to the total TH field. It also indicates that silica layers with small $\chi^{(3)}$ only compensate for TH field phase. In addition, since the coherence length for silica is 3.3 μm, consequently the optimum designs with large number of layers are thicker. The TH energy growth is the coherent sum of TH fields due to each layer, which is proportional to square of total thickness d^2 of stack, or simply the number of layers $(N/2)^2$. Figure. 4.8 shows this trend for the optimized designs.

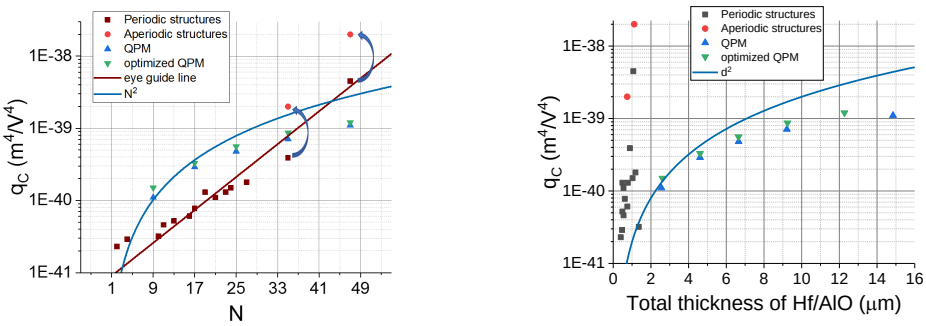

(a) (b)

Figure 4.12: q_C of C designs optimized in transmission relative to (a) number of layers N, (b) total thickness of stack d

While, the QPM-like design is optimized, it still is not the global optimum design. Because, a set of design optimized based on a a random initial design, and only constrianet was that the thickness of all Silica layers has to be same, and Hafnia layers has to be same. The results after optimiztion are periodic structures (periodic structures in Fig. 4.12(a), and 4.12(b)). Later, we removed the constraint on the thickness equalness of all Silica layers and all Hafnia layers, and let optimization algorithm to optimize further the two of the periodic structures. These optimized structures (aperiodic structures in Fig. 4.12(a), and 4.12(b)) improved q_C by a factor more than 2. The results show that for $N > 33$ the periodic and aperiodic structures have larger q_C compared to QPM-like structures.

In general periodic and aperiodic structures have two advantages compared to QPM-like based designs. First, while silica layers compensate for phase mismatch, they also generate negligible out of phase TH fields respect to TH fields in hafnia layers. Second, the total thickness of optimum designs at a fixed number of layers have larger THG. see Fig. 4.8.

Finally, the aperiodic structures in transmission have the largest q_C values at

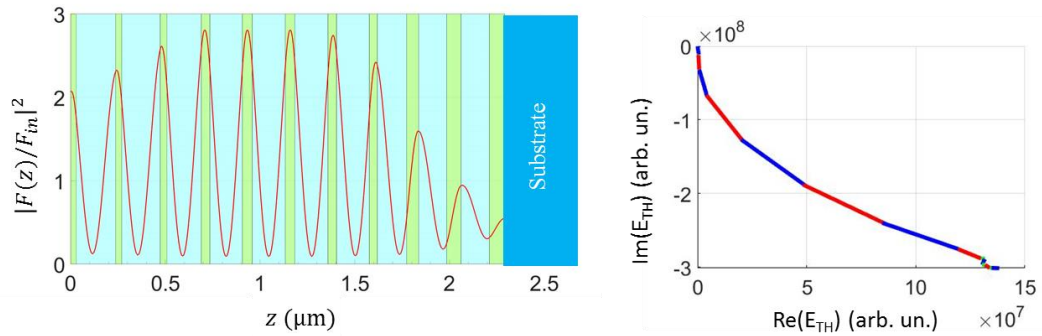

Figure 4.13: Intensity and phasor diagram of a design optimized in transmission with N=21

$N > 33$. Comparing these designs in transmission to C designs in reflection, still the C designs in reflection show bigger q_C values. So, the designs are optimized for maximum TH conversion efficiency in reflection geometry.

4.9 Monochromatic Design Bandwidth

An FTM optimized at a single fundamental wavelength, generates significant amount of TH in the vicinity of the optimization wavelength. However, the TH signal in optimum designs, for example A designs, with $N \geq 5$ drops as the wavelength of the fundamental beam is detuned from the optimization wavelength. The design bandwidth is a parameter that describes the full width at half maximum of the TH signal plotted as a function of the fundamental wavelength. The TH signal for the same incident electric field is proportional to q_A. Therefore we used the q_A value for all designs (A, B, and C type) to evaluate the design bandwidth ($\Delta\lambda$). The results are summarized in Fig. 4.14. Here we plot q_A as a function of ($\Delta\lambda$).

The trend line follows $q_A \propto \Delta\lambda^{-4}$. Since A and C designs with a sufficiently large number of layers resemble a Fabry-Perot resonator the fundamental intensity

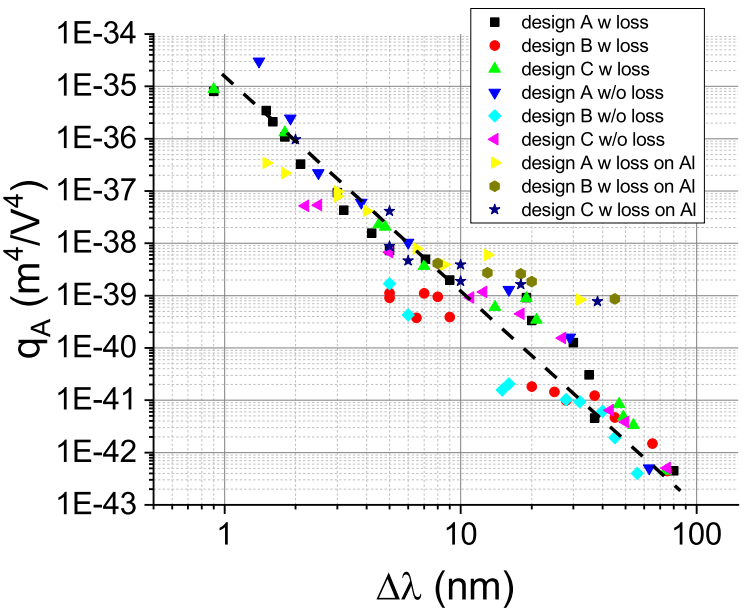

Figure 4.14: q_A as a function of the FTM bandwidth ($\Delta\lambda$). The data points correspond to different numbers of layers and design concepts. q_A for the case of B type and C type means q (TH signal) at a fixed incident fluence, which is basically the definition of q_A, cf. Eq. (4.6).

I_F at the resonance wavelength is proportional to $1/\Delta\lambda$ to first order. Since $q_A \propto I_F^3$, we expect q_A will be proportional to $\Delta\lambda^{-3}$. The discrepancy compared to the aforementioned trend line is probably due to the difficulty of in-phase addition of different spectral components. This could lead to another $1/\Delta\lambda$ factor in the relation between q_A and $\Delta\lambda$.

4.10 The Absolute TH Conversion Efficiency of an FTM

The conversion efficiency of THG process is the ratio of the energy of the TH pulse and the fundamental pulse. For simplification, we assume a fundamental pulse with a Gaussian spatial and temporal profile.

$$E_F(r,t) = E_{F,0} e^{-r^2/w_F^2} e^{-t^2/\tau_F^2}, \tag{4.13}$$

where r, and t are position and time, respectively. w_F is the beam waist, and $\tau_G = \tau_p/\sqrt{2\ln 2}$ is Gaussian pulse duration of fundamental pulse (τ_p is the pulse duration at full width at half maximum of pulse intensity). The fundamental pulse energy

$$U_F = 2c\epsilon_0 \int_{-\infty}^{\infty} dt 2\pi \int_{-\infty}^{\infty} r dr |E_F(r,t)|^2 \tag{4.14}$$

can be calculated analytically for a Gaussian pulse and beam profile, which yields

$$U_F = \pi \sqrt{\frac{\pi}{2}} c\epsilon_0 \tau_G w_F^2 |E_{F,0}|^2. \tag{4.15}$$

The TH pulse energy, using the fact that the TH beam waist is $w_{TH} = w_F/\sqrt{3}$, and the TH pulse duration is $\tau_{TH} = \tau_G/\sqrt{3}$, is then

$$U_{TH} = \frac{\pi}{3} \sqrt{\frac{\pi}{6}} c\epsilon_0 \tau_G w_F^2 |E_{TH,0}|^2. \tag{4.16}$$

The TH conversion efficiency, taking into account the relation $|E_{TH,0}|^2 = q_A |E_{F,0}|^6$, becomes

$$\eta = \frac{U_{TH}}{U_F} = \frac{2}{3\sqrt{3}\pi^3 c^2 \epsilon_0^2 \tau_G^2 w_F^4} q_A U_F^2 \tag{4.17}$$

Equation. (4.17) shows that the TH conversion efficiency increases with the square of the fundamental pulse energy, and decreases with the second power of the fundamental pulse duration and fourth power of the waist of the fundamental beam.

The TH conversion efficiency (η) of an A design with just a single Hafnia layer $N = 1$, see Fig. 4.3 (a2 data points, red circles), with $q_A = 4.47 \times 10^{-43}$ m^4/V^4 at a pulse energy of $U_F = 10$ nJ, pulse duration of $\tau_p = 100$ fs, and beam waist of $w_F = 10$ μm (fundamental fluence would be 6.4 mJ/cm^2) is $\eta = 1.09 \times 10^{-9}$. The TH conversion in an FTM depends on the square of the incident fundamental intensity (I_F^2) and magnitude of q_A. For example, for A type design with $N = 31$, cf. a2 in Fig. 4.3, with the same beam and pulse parameters as before, $\eta = 1.09 \times 10^{-2}$ with loss in dielectric materials, and a2 in Fig. 4.3 $\eta = 1.02 \times 10^{-1}$ without loss.

At damage threshold($F_{crit} \approx 475$ mJ/cm^2 for Hafnia with pulses of 55 fs at central wavelength of 800 nm) for A type design with $N = 31$, the TH conversion efficiency is $\eta = 2.66 \times 10^{-2}$. Note, in this design field intensity enhancement $f^2 = 46$, which corresponds to critical incident fluence of 10 mJ/cm^2.

The increase of intensity/fluence is constrained practically by the material breakdown (optical damage). To take this into account, one should use type C designs. As it is discussed earlier in Fig. 4.7, q_C grows exponentially with N of optimum FTM. So, larger conversion efficiencies are possible for large N.

Within the framework of this model and its limitations, conversion efficiencies larger than 20 % are predicted before the LIDT is reached for C designs. However it should be mentioned these solutions are violating pump depletion assumption. We will discuss later the model limitations and practical issues.

4.11 The Experimental Results of FTMs Design with the Monochromatic Approach

In this section we will study the effect of the design bandwidth on the THG experimentally. We will compare the TH signal from three samples with different design

bandwidths, see Table 4.3. The FTMs are illuminated with pulses that have a different bandwidth. For comparison, note that a transform limited pulse with a temporal Gaussian profile, and pulse duration of 50 fs at 787 nm has a bandwidth of 16 nm. The bandwidth of the incident laser pulse is changed and the TH signal is recorded.

We set up an experiment to measure the TH signal versus the pulse duration, while keeping the central wavelength at the resonance wavelength for each sample and incident fluence fixed. Figure. 4.15 shows the experimental setup. We used a Ti:Sapphire oscillator with an average output power of 1.2 W, with a repetition rate of 110 MHz, a central wavelength of 791 nm (tunable in a range of $\pm$20 nm), a bandwidth of 16 nm, and a pulse duration of 55 fs. There is Faraday isolater to avoid fundamental pulse feedback into the laser cavity. A Pockells cell is used to enable single shot, and bursts of a desired number of fundamental pulses. The Faraday isolator and the Pockells cell introduce group velocity dispersion (GVD), broadening the pulses. A two-prism compressor (double pass) is used for GVD compensation and restores the original pulse duration (55 fs). A Dichroic Mirror (DM) reflects the TH (reflection $>$ 99%) and transmits the fundamental (transmission $>$ 92%). An $f = 5$ cm lens is used to focus the fundamental beam onto the sample surface. A photo-multiplier (PMT) is used as detector for the generated TH. A band pass filter (BPF) blocks the fundamental. Note, inside the compressor right before the high reflective (HR) end mirror, two parallel razor blades form an adjustable slit to control the pulse bandwidth.

The pulse duration measured using GRENOUILLE device relative to pulse bandwidth measured using spectrometer is recorded for different slit widths, see Fig. 4.16(a). At each slit width, the TH signal is measured for both the single layer sample, and the sample (FTM) under investigation. As we closed the slit we kept the central wavelength fixed at the wavelength where the TH signal from each sample peaked, see Fig. 4.16(b).

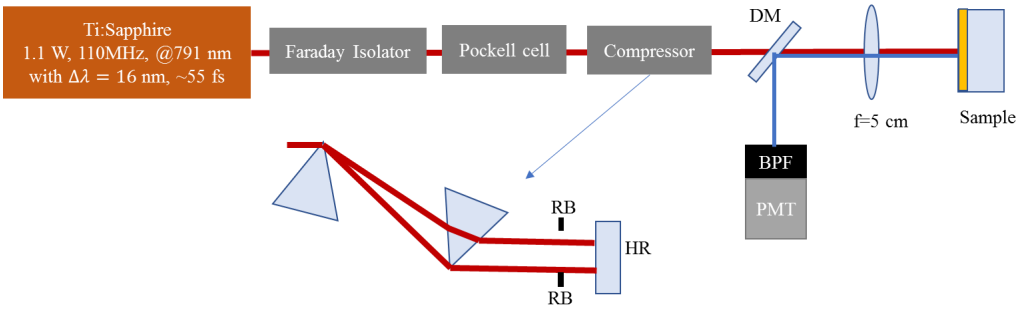

Figure 4.15: Experimental setup of measuring the TH signal as a function of the pulse bandwidth. DM - dichroic mirror, BPF - band pass filter , PMT - photomultiplier tube, HR - high reflective mirror at normal incidence (HR), BR - and razor blade.

The TH signal versus the pulse's central wavelength is measured for all samples. The peak wavelength of the filtered pulses coincides with the peak wavelength for maximum TH signal in the case of the full pulse spectrum (sample OS at 791 nm, sample L1R at 785 nm, and sample N1R at 780 nm). The samples were SL: single layer Hafnia (film thickness $d = 377$ nm) on a 6 mm fused silica substrate, with bandwidth larger than pulse bandwidth, OS: a sample with 25 layers $\Delta\lambda = 6$ nm,

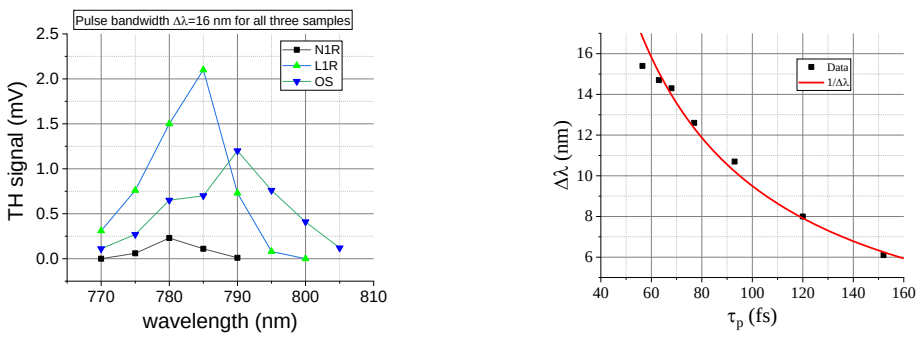

(a) (b)

Figure 4.16: (a) The TH signal generated in different samples as a function of the central wavelength of the incident pulse for constant pulse duration of 60 fs. (b) The pulse bandwidth measured with a spectrometer as a function of the pulse duration measured with GRENOUILLE device.

L1R: a sample with 25 layers $\Delta\lambda = 6$ nm, and N1R: a sample with 37 layers $\Delta\lambda = 0.6$ nm, see also Table. 4.3.

Table 4.3: **Parameters of samples used to obtain the results in Fig. 4.16(a). The TH efficiency peaks at the central wavelength (λ_{peak}) of the fundamental pulse at full pulse spectrum. The FTMS have a design bandwidth of $\Delta\lambda$ and consist of N layers. SL corresponds to a single layer Hafnia on top of the substrate. The TH from this layer is measured at all three λ_{peak} of 791, 785, and 780 nm for comparison.**

Sample name	λ_{peak} (nm)	$\Delta\lambda$ (nm)	N
OS	791	6	25
L1R	785	6	25
N1R	780	0.6	37
SL	N/A	N/A	1

The TH signals of the three samples were measured and compared to a single layer of Hafnia. Note, the single layer has a conversion bandwidth much larger than the pulse bandwidth. The maximum TH signal does not happen at the same wavelength for all samples as shown in Fig. 4.16(b). Figure. 4.17 shows the experimental values and expected theoretical values divided by the signal from the SL sample, Eq. (4.18). This ratio is

$$R_\lambda = \frac{S_\lambda^X}{S_\lambda^{SL}}, \tag{4.18}$$

where X (S_λ^X) refers to the FTM and SL (S_λ^{SL}) to a single layer Hafnia sample. Figure. 4.17 shows that as the bandwidth of the incident pulse decreases the R increases. The slope of this increase for the sample N1R is much steeper than for the others. The reason is that this sample has a much narrower design bandwidth compared to the other designs. The samples OS and L1R show similar behavior because they have same design bandwidth. In conclusion, the pulse bandwidth needs to be implemented in the design optimization to look for solutions that have larger design bandwidths, to produce large TH signals, and to be more practically relevant for short pulses.

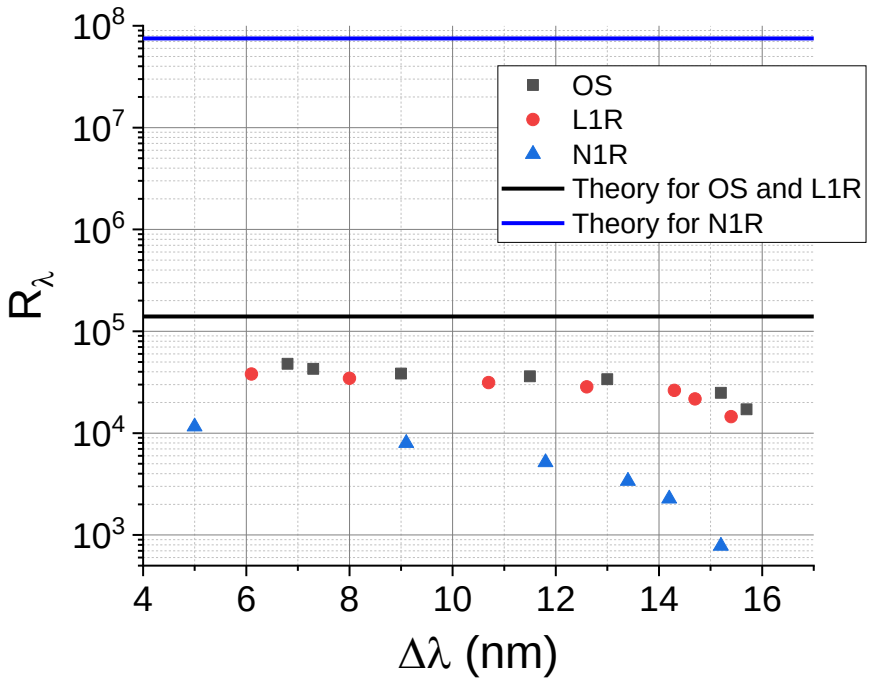

Figure 4.17: The TH signal of the different samples listed in Table 4.3 divided by the signal from the SL sample as a function of the incident pulse bandwidth.

4.12 Summary

In this chapter we addressed scaling laws governing frequency tripling mirrors based on A, B, and C designs. It is shown how a simple model based on a Fabry-Perot-like resonant structure can explain the exponential growth of q_A, and q_C designs with the number of layers N as suggested by the computer design. Loss due to absorption of dielectric materials at the TH wavelength is the dominant factor in decreasing the growth slope at small N. Absorption of the fundamental radiation is the limiting process at large N. In all three designs, a dielectric mirror, reflective at the fundamental and the TH wavelength is formed on top of the substrate, see

appendix F. This mirror can be replaced with a broadband reflective metal resulting in designs of similar performance parameters with fewer number of layers. Layer thickness fluctuations that are introduced by the film deposition decrease the THG efficiency and become more critical for FTMs with large N. Robustness against such fluctuations can be incorporated in the design process. The design bandwidth of A, B, and C designs gets narrower with increase of q_A, q_B, and q_C values, respectively. The transmission designs compared to reflective designs at same number of layers indicate smaller TH values.

Chapter 5

Frequency Tripling Mirrors Designed with Pulse Model and Experiments

A model will be developed that predicts THG from FTMs using the full pulse bandwidth. The model will be discussed in the frequency domain. This approach will be compared to the monochromatic model to understand the effect of pulse bandwidth for the TH conversion efficiency. FTMs based on this pulse model using A and C design concepts will be introduced. Experimental test results of selected FTMs will be presented and discussed.

5.1 Implementation of the Full Bandwidth of a Pulse in Design of FTMs

A pulse with electric field $E_{F,t}(z,t)$ that propagates in $+z$ direction and has a spatial profile of a plane wave is incident on the surface of a stack of thin film layers, where z, t are the position and time coordinate, respectively. The spectral field is obtained via a Fourier Transform, see appendix D.

$$E_{F,\Omega}(z,\Omega) = \mathcal{F}\{E_{F,t}(z,t)\} \tag{5.1}$$

Since the amplitude of each spectral component is known at the input interface, the amplitude of the electric field can be calculated through the matrix formalism at each interface inside the stack (Note, the indices t and Ω will be dropped because the time and frequency dependencies are shown in the arguments), see appendix E. We solve the nonlinear wave equation in the presence of all fundamental spectral component in each layer. The produced TH in each layer will propagate to the output interfaces as shown in appendix E.

Our goal is to solve the nonlinear wave equation that governs THG due to two fundamental pulses that propagate in a layer in opposite directions. The fundamental electric field $E_F(z,t)$ at each position inside a layer i (note we will not show the index i in the equations to keep the relations simple) is the sum of the electric fields propagating in the right ($+z$) direction $B_{1,r}(z,t)e^{-ik_1 z}$ and left (-z) direction $B_{1,l}(z,t)e^{+ik_1 z}$ as follow:

$$E_F(z,t) = B_{F,r}(z,t)e^{-ik_1 z} + B_{F,l}(z,t)e^{+ik_1 z} \tag{5.2}$$

where $k_1 = 2\pi n_1 f_1$, n_1 is the refractive index at the fundamental frequency f_1 and $\omega_1 = 2\pi f_1$. The fundamental electric field $E_F(z,t)$ at each point will generate TH

fields that propagate to the right $E_r(z,t)$ and the left $E_l(z,t)$:

$$E_r(z,t) = B_r(z,t)e^{i(\omega_3 t - k_3 z)} \tag{5.3}$$

$$E_l(z,t) = B_l(z,t)e^{i(\omega_3 t + k_3 z)} \tag{5.4}$$

where $k_3 = 2\pi n_3 f_3$, n_3 is the refractive index at the TH frequency f_3 and $\omega_3 = 2\pi f_3$. The third order susceptibility $\chi^{(3)}$ is assumed to be frequency independent, that is the nonlinear process is instantaneous. Assuming the slowing varying envelope approximation and a linear frequency dependence of $k(\Omega)$, the nonlinear wave equation can be separated into two relations that governs THG in $+z$ and -z directions [25].

$$\left(\frac{\partial}{\partial z} + \frac{1}{v_{g3}}\frac{\partial}{\partial t}\right) B_r(z,t) = \frac{9\omega_1^2\chi^{(3)}}{2ik_3c^2} e^{ik_3 z}\left(B_{F,r}(z,t)e^{-ik_1 z} + B_{F,l}(z,t)e^{+ik_1 z}\right)^3 \tag{5.5}$$

$$\left(\frac{\partial}{\partial z} - \frac{1}{v_{g3}}\frac{\partial}{\partial t}\right) B_l(z,t) = \frac{9\omega_1^2\chi^{(3)}}{2ik_3c^2} e^{-ik_3 z}\left(B_{F,r}(z,t)e^{-ik_1 z} + B_{F,l}(z,t)e^{+ik_1 z}\right)^3 \tag{5.6}$$

where v_{g3} is the group velocity at the TH frequency. We introduce new variables $\tau = t - z/v_{g3}$, and $\xi = z$ in Eq. (5.5), and $\tau = t + z/v_{g3}$, and $\xi = z$ in Eq. (5.6). This yields

$$\frac{\partial}{\partial \xi} B_r\left(\xi, \tau + \frac{\xi}{v_{g3}}\right) = \frac{9\omega_1^2\chi^{(3)}}{2ik_3c^2} e^{ik_3\xi}\left(B_{F,r}\left(\xi, \tau + \frac{\xi}{v_{g3}}\right)e^{-ik_1\xi} + B_{F,l}\left(\xi, \tau + \frac{\xi}{v_{g3}}\right)e^{+ik_1\xi}\right)^3 \tag{5.7}$$

$$\frac{\partial}{\partial \xi} B_l\left(\xi, \tau - \frac{\xi}{v_{g3}}\right) = \frac{9\omega_1^2\chi^{(3)}}{2ik_3c^2} e^{-ik_3\xi}\left(B_{F,r}\left(\xi, \tau - \frac{\xi}{v_{g3}}\right)e^{-ik_1 z} + B_{F,l}\left(\xi, \tau - \frac{\xi}{v_{g3}}\right)e^{+ik_1 z}\right)^3 \tag{5.8}$$

If we expand k up to first order in frequency. In our new frame of coordinates with the initial conditions $B_r(0) = 0$ and $B_l(0) = 0$, the solutions of the differential

Eq. (5.7) and Eq. (5.8) are:

$$B_r(\tau) = \frac{9\omega_1^2\chi^{(3)}}{2ik_3c^2}\int_0^d d\xi e^{ik_3\xi} \left(B_{F,r}\left(\tau+\left(\frac{1}{v_{g3}}-\frac{1}{v_{g1}}\right)\xi\right)e^{-ik_1\xi} + B_{F,l}\left(\tau+\left(\frac{1}{v_{g3}}+\frac{1}{v_{g1}}\right)\xi\right)e^{+ik_1\xi}\right)^3 \tag{5.9}$$

$$B_l(\tau) = \frac{9\omega_1^2\chi^{(3)}}{2ik_3c^2}\int_0^d d\xi e^{-ik_3\xi} \left(B_{F,r}\left(\tau+\left(-\frac{1}{v_{g3}}-\frac{1}{v_{g1}}\right)\xi\right)e^{-ik_1z} + B_{F,l}\left(\tau+\left(-\frac{1}{v_{g3}}+\frac{1}{v_{g1}}\right)\xi\right)e^{+ik_1z}\right)^3 \tag{5.10}$$

After performing a Fourier Transform of Eq. (5.9) and Eq. (5.10) and integration them with respect to ξ over a thickness d, the TH field in +z direction becomes:

$$\begin{aligned} B_r(\Omega) = {} & \frac{1}{(2\pi)^2}\frac{9\omega_1^2\chi^{(3)}d}{2ik_3c^2} \\ & e^{-i\frac{\Gamma_1 d}{2}}\,\mathrm{sinc}\left(\frac{\Gamma_1 d}{2}\right)\int_{-\infty}^{+\infty}d\Omega' B_{F,r}(\Omega-\Omega')\int_{-\infty}^{+\infty}d\Omega'' B_{F,r}(\Omega'-\Omega'')B_{F,r}(\Omega'') \\ & + e^{-i\frac{\Gamma_2 d}{2}}\,\mathrm{sinc}\left(\frac{\Gamma_2 d}{2}\right)\int_{-\infty}^{+\infty}d\Omega' B_{F,l}(\Omega-\Omega')\int_{-\infty}^{+\infty}d\Omega'' B_{F,l}(\Omega'-\Omega'')B_{F,l}(\Omega'') \\ & + 3\int_{-\infty}^{+\infty}d\Omega' B_{F,l}(\Omega-\Omega')e^{-i\frac{\Phi_1 d}{2}}\,\mathrm{sinc}\left(\frac{\Phi_1 d}{2}\right)\int_{-\infty}^{+\infty}d\Omega'' B_{F,r}(\Omega'-\Omega'')B_{F,r}(\Omega'') \\ & + 3\int_{-\infty}^{+\infty}d\Omega' B_{F,r}(\Omega-\Omega')e^{-i\frac{\Phi_2 d}{2}}\,\mathrm{sinc}\left(\frac{\Phi_2 d}{2}\right)\int_{-\infty}^{+\infty}d\Omega'' B_{F,l}(\Omega'-\Omega'')B_{F,l}(\Omega'') \end{aligned} \tag{5.11}$$

where the phase terms are

$$\Gamma_1 = 3k_1 - k_3 - \Omega\left(\frac{1}{v_{g3}}-\frac{1}{v_{g1}}\right) \tag{5.12}$$

$$\Gamma_2 = -3k_1 - k_3 - \Omega\left(\frac{1}{v_{g3}}+\frac{1}{v_{g1}}\right) \tag{5.13}$$

$$\Phi_1 = k_1 - k_3 - \Omega\left(\frac{1}{v_{g3}} + \frac{1}{v_{g1}}\right) + \frac{2\Omega'}{v_{g1}} \tag{5.14}$$

$$\Phi_2 = -k_1 - k_3 - \Omega\left(\frac{1}{v_{g3}} - \frac{1}{v_{g1}}\right) - \frac{2\Omega'}{v_{g1}}. \tag{5.15}$$

A similar procedure for the amplitude in -z direction yields

$$\begin{aligned} B_l(\Omega) = {} & \frac{1}{(2\pi)^2}\frac{9\omega_1^2\chi^{(3)}d}{2ik_3c^2} \\ & e^{-i\frac{\Gamma_1' d}{2}}\,\mathrm{sinc}\left(\frac{\Gamma_1' d}{2}\right)\int_{-\infty}^{+\infty} d\Omega' B_{F,r}(\Omega-\Omega')\int_{-\infty}^{+\infty} d\Omega'' B_{F,r}(\Omega'-\Omega'')B_{F,r}(\Omega'') \\ & + e^{-i\frac{\Gamma_2' d}{2}}\,\mathrm{sinc}\left(\frac{\Gamma_2' d}{2}\right)\int_{-\infty}^{+\infty} d\Omega' B_{F,l}(\Omega-\Omega')\int_{-\infty}^{+\infty} d\Omega'' B_{F,l}(\Omega'-\Omega'')B_{F,l}(\Omega'') \\ & + 3\int_{-\infty}^{+\infty} d\Omega' B_{F,l}(\Omega-\Omega')e^{-i\frac{\Phi_1' d}{2}}\,\mathrm{sinc}\left(\frac{\Phi_1' d}{2}\right)\int_{-\infty}^{+\infty} d\Omega'' B_{F,r}(\Omega'-\Omega'')B_{F,r}(\Omega'') \\ & + 3\int_{-\infty}^{+\infty} d\Omega' B_{F,r}(\Omega-\Omega')e^{-i\frac{\Phi_2' d}{2}}\,\mathrm{sinc}\left(\frac{\Phi_2' d}{2}\right)\int_{-\infty}^{+\infty} d\Omega'' B_{F,l}(\Omega'-\Omega'')B_{F,l}(\Omega''), \end{aligned} \tag{5.16}$$

where the phase terms are

$$\Gamma_1' = 3k_1 + k_3 - \Omega\left(\frac{1}{v_{g3}} + \frac{1}{v_{g1}}\right) \tag{5.17}$$

$$\Gamma_2' = -3k_1 + k_3 - \Omega\left(\frac{1}{v_{g3}} - \frac{1}{v_{g1}}\right) \tag{5.18}$$

$$\Phi_1' = k_1 + k_3 - \Omega\left(\frac{1}{v_{g3}} - \frac{1}{v_{g1}}\right) + \frac{2\Omega'}{v_{g1}} \tag{5.19}$$

$$\Phi_2' = -k_1 + k_3 - \Omega\left(\frac{1}{v_{g3}} + \frac{1}{v_{g1}}\right) - \frac{2\Omega'}{v_{g1}}. \tag{5.20}$$

Note that d is the material thickness, v_{g1},v_{g3} are the group velocities of the fundamental and TH pulse, respectively.

5.2 Numerical Results

The numerical search for FTMs now proceeds as follows. First, we calculate the fundamental field in each layer as a function of frequency, e.g. $E_{F,i}(\Omega)$ for the field

in layer number i, see Appendix. D. Using this field we can now determine the eight components of the TH field produced in each layer; the left and right-propagating TH fields have four components each, see Eq. (5.11), and Eq. (5.16). The sum of the TH fields from all layers at the output of the mirror in reflection produces the total TH field $E_{TH}(\Omega)$ from which the TH energy can be obtained using Parseval's theorem.

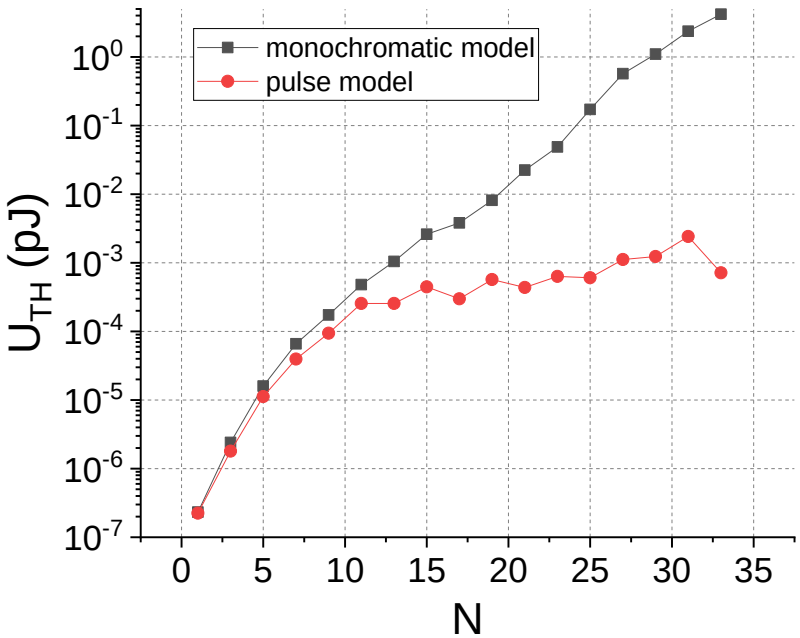

Figure 5.1: TH pulse energy of optimum monochromatic A designs predicted with both the monochromatic model, see section 4.10, and the pulse model as a function of the number of layers N. The parameters of the incident fundamental pulse were $U_F = 1$ nJ, $w_0 = 6$ μm and $\tau_p = 60$ fs.

As an example of the importance of the pulse spectrum, we calculated the TH pulse energy using the pulse model for the A designs that are optimized using monochromatic model. To compare the value of TH energy, we assumed a fun-

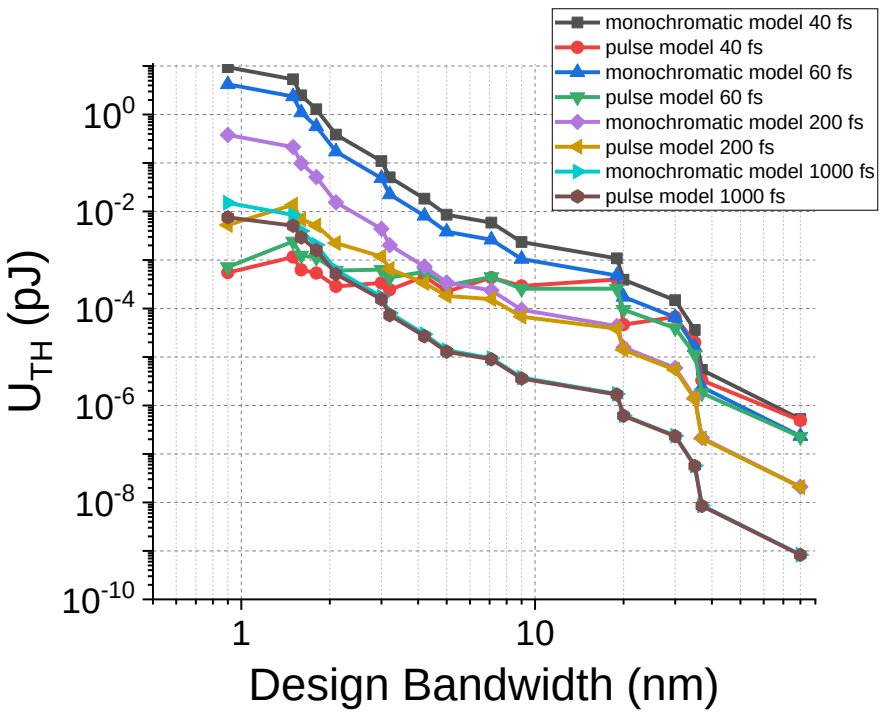

Figure 5.2: TH pulse energy of optimum monochromatic A designs, see section 4.10, predicted with both the monochromatic model and pulse model, at fixed incident fundamental pulse parameters of $U_F = 1$ nJ, $w_0 = 6$ μm, at different pulse duration (τ_p) as a function of design bandwidth.

damental pulse with Gaussian spatial profile that has a beam waist of 6 μm, and a transform limited pulse with Gaussian temporal profile that has a pulse duration of $\tau_p = 60$ fs. Note, it is assumed the the total thickness of the stack of thin films is negligible compared to confocal parameter of incident beam, so a Gaussian beam is approximated with a plane wave. For example, the confocal parameter of 6 μm beam waist at 800 nm is 283 μm, which is much larger than total thickness of a stack, which in general is below 10 μm. Figure. 5.1 shows that the TH pulse energy due to prediction of both monochromatic and pulse model coincides at low N. However, at larger number of layers $N \geq 13$ the TH energy differs by more than factor of 4. In other word TH energy does not scale exponentially with number of layers N as

monochromatic model predicted, see Eq. (4.6).

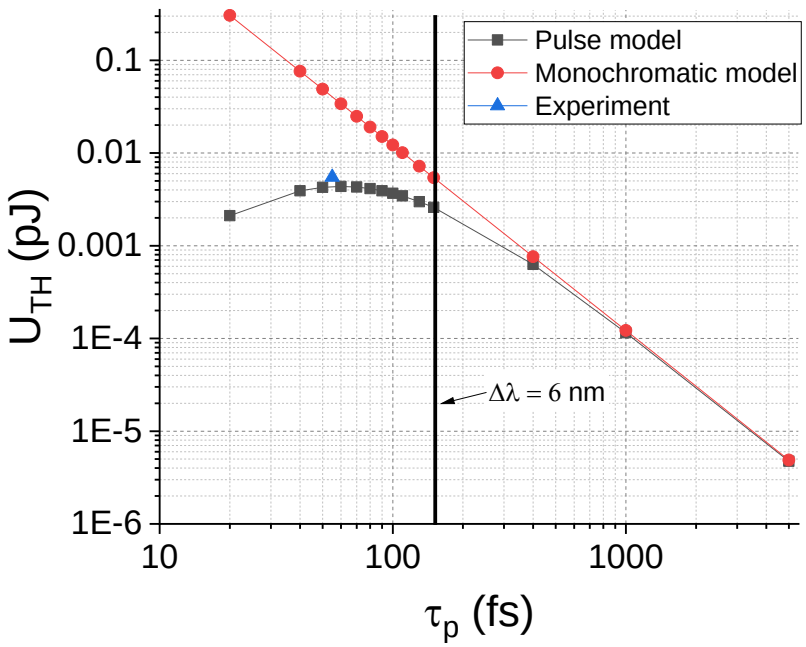

Figure 5.3: TH pulse energy, see section 4.10, from an FTM (monochromatic A design, see design OS in appendix C) produced with different pulse durations (τ_p) using the monochromatic model and the pulse model. The incident fundamental pulse parameters were $U_F = 1$ nJ, $w_0 = 6$ μm. The experimental data point coincides with the pulse model prediction. The vertical line at $\tau_p = 152$ fs is at the pulse duration of a transform-limited Gaussian pulse with bandwidth of $\Delta\lambda = 6$ nm (This is also the design bandwidth of OS).

This can be understood by comparing the design bandwidth $\Delta\lambda$ to the incident pulse spectrum, where we assume a transform-limited pulse with Gaussian profile. Figure. 5.2 shows the TH pulse energy relative to monochromatic design bandwidth for different pulse duration. According to Fig. 5.2 the monochromatic and pulse model predictions coincide with each other as long as the incident pulse bandwidth is smaller than the design bandwidth. However, as the incident pulse spectrum gets larger than design bandwidth, the design no longer supports those broadband pulses,

and the TH conversion efficiency decreases. Therefore, the concept of A, B, and C monochromatic designs that favors only a large q value, is inadequate if it leads to designs that have bandwidth much smaller than the incident pulse bandwidth.

As an example of the impact of the pulse spectrum we calculated the conversion efficiency as a function of pulse duration for an FTM with 25 layers, which produced a maximum conversion efficiency of about 1 % in practice. Figure. 5.3 compares the predictions of the monochromatic to the pulse model as a function of the pulse duration. At an incident fundamental Gaussian pulse with pulse duration of 60 fs, the monochromatic model overestimates the TH conversion efficiency by a factor of 10. The pulse model prediction match the experiment with better accuracy rather than the monochromatic model.

5.3 FTM Design at a Fixed Incident Fluence

The FTMs based on the pulse model are optimized for maximum TH conversion efficiency at a fixed incident fluence similar to the monochromatic A type designs. The incident pulses on multi-layer dielectric stack are assumed to be transform limited Gaussian pulses with pulse duration of 60, and 100 fs at a central wavelength of 787 nm. The materials are Hafnia and Silica on top of a substrate with the parameters from Table. 4.1. Figure. 5.4 shows the TH conversion efficiency of optimum designs relative to the number of layers N.

The TH conversion efficiency of optimum A designs without absorption scales with the second power of N. N_0 and η_0 are fitting parameters in Fig. 5.4 that shows the growing trend up to 45 layers. As the number of layers increases, there are more layers that contributes to THG. Since, the total TH is the coherent sum of electric fields generated in each individual layer, the THG should scale with N^2 for given fundamental pulse parameters.

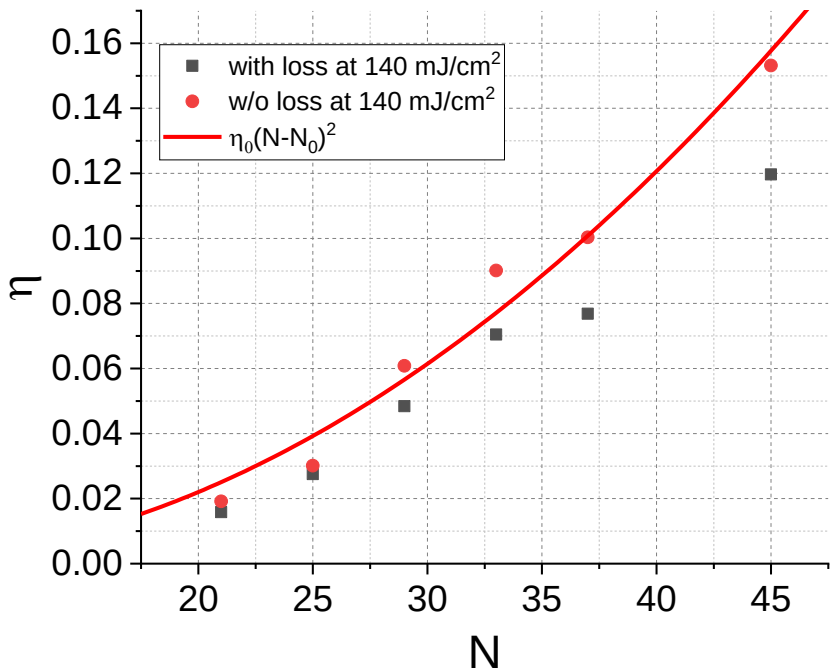

Figure 5.4: TH conversion efficiency of FTMs designed with the pulse model as a function of the number of layers. A fundamental transform-limited Gaussian pulse with $\tau_p = 60$ fs with fluence of 140 mJ/cm^2 was assumed. The red line is a parabolic fit with parameters $\eta_0 = 9.9 \times 10^{-5}$, and $N_0 = 5.1$.

Figure 5.5 refers to an optimum design with $N = 45$ and shows the normalized monochromatic electric field intensity at the central wavelength for monochromatic input, and the pulse intensity at the moment when it reaches a maximum inside the stack. The figure shows the results for different pulse durations. A narrow-bandwidth Gaussian pulse with a duration of 1 ps and monochromatic input show similar results. However, as the pulse duration decreases, the profile of electric field intensity inside the stack drops in magnitude and also changes in shape for very short pulses for instance at 10 fs. Therefore, the fundamental electric field enhancement is not as large as the monochromatic beam for short pulses inside a dielectric stack,

and this has a direct impact on THG. Note, the fundamental field intensity profile shown in Fig. 5.5 is only for the moment when the fundamental pulse intensity has the highest value inside the stack. At earlier or later time intervals the profile of fundamental intensity is different, with a lower peak value. The TH pulse energy is the accumulation of TH generation at each time and therefore the time-dependent intensity enhancement is important to make correct predictions.

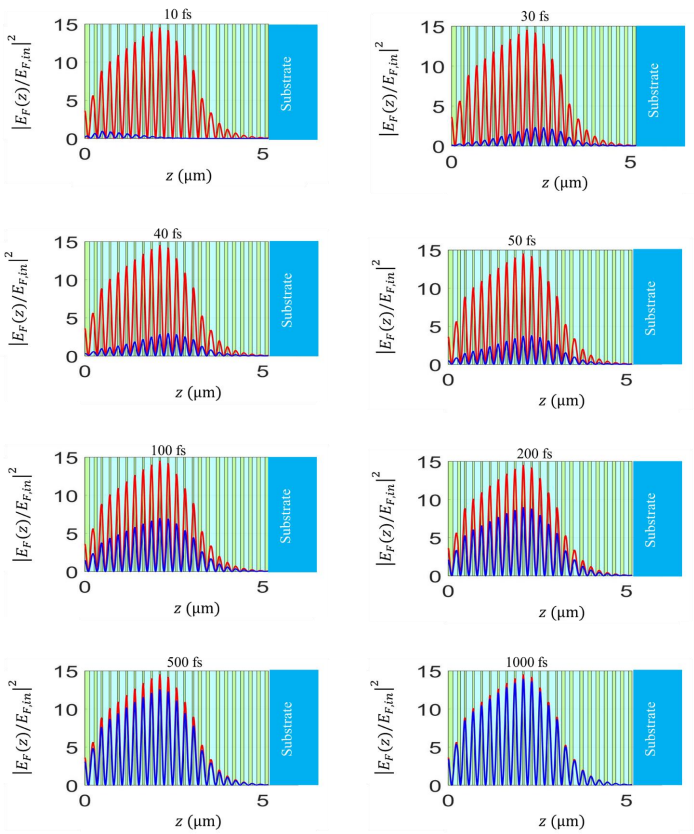

Figure 5.5: Field intensity distribution normalized to the peak incident field intensity inside the layer stack of an FTM, sample S2 (see Appendix C), with $N = 45$ for different duration(τ_p) of the incident pulses (blue) and monochromatic input (red) for comparison. The center wavelength is $\lambda = 787$ nm.

Based on Eq. (4.4), the TH conversion efficiency depends on the peak fundamental field intensity distribution, and the number of the layers in which an intensity

peak close to the maximum occurs. Equation (4.17) states that the TH conversion efficiency is related inversely to the second power of the incident pulse duration. Note, a Gaussian beam is approximated with a plane wave that its amplitude could be related to amplitude and beam waist of Gaussian beam. This perspective, which is true in case of a monochromatic plane wave could not be generalized for a pulse.

Let's call the moment that maximum fundamental field intensity enhancement occurs in time t_{peak}. The fundamental field intensity distribution will vary before and after t_{peak}, too, so it will still generate TH. Therefore, the time interval that fundamental field intensity enhancement is comparable to maximum value at t_{peak}, is another factor that will decide the TH conversion efficiency.

The designs optimized with the pulse model for short pulse duration ($<$ 100 fs) have more layers that are contributing to THG compared to monochromatic designs. This is because more layers show a similar field intensity enhancement. In addition, the designs optimized with the pulse model show larger design bandwidth. This means that for the same q_A the design optimized with the pulse model have a larger bandwidth compared to the design that is optimized with the monochromatic model. For example, let's take an A type monochromatic design with loss that has a design bandwidth of $\Delta\lambda = 2$ nm, $N = 25$, and $q_A = 3.3 \times 10^{-37}$ $\mathrm{m}^4/\mathrm{V}^4$, see Fig. 4.14.—textcolorrednot clear what you want to use this example for. The pulse model FTMs below have different N. You need to motivate and summarize this discussion better.

The designs with $N = 45$, and $N = 65$ that are optimized with pulse model(for the case of a transform-limited Gaussian pulse profile with 60 fs pulse duration) that have the same q_A as A type monochromatic design have design bandwidth of $\Delta\lambda = 7$ nm, and $\Delta\lambda = 10$ nm, respectively. It should also be noted that designs optimized with pulse model with the large bandwidth at the same q_A have more layers compared to stack of thin films that are optimized based on monochromatic

A design concept. In summary, the designs optimized based on pulse model have larger design bandwidth compared to monochromatic designs both at the same q_A.

The phasor diagram of TH fields from the individual layer for monochromatic input suggests nearly optimal phase alignment for constructive interference.

However, the phasor of TH fields due to each layer at wavelengths longer or shorter than the optimization wavelength add up less than optimal.

While such phasor diagram picture of TH fields was true for optimum monochromatic designs, it is not the case for designs optimized with pulse model. The phasor of TH fields due to each layer for wavelengths in the range of full width at half maximum of central wavelength are also in phase.

Another important parameter is the absorption loss in the designs optimized with the pulse model. The absorption at the fundamental wavelength is negligible in the optimum designs. For example, the absorption at the central wavelength of the fundamental pulse, for a optimum design with $N = 45$, leads to a reduction in conversion by 1%. Unlike, monochromatic designs where absorption at the fundamental is important due to their Fabry-Perot structure, absorption at the fundamental regime is almost negligible. The absorption at the TH wavelength is the main loss mechanism. For the design with $N = 45$, the conversion of TH wavelength drops by 23% when absorption at TH wavelength is included. Using materials with low absorption at the TH wavelength would improve the FTM performance.

Figure. 5.6 shows the transmission spectrum of an optimum design with $N = 45$ at $\lambda = 789.5$ nm. As expected the transmission at TH and fundamental is low. From our previous discussion we expect the FTM to be reflective in these spectral regions. The fundamental is close to a local transmission maxima (10%).

The local peak happens in the vicinity of the central wavelength of the fundamental pulse.

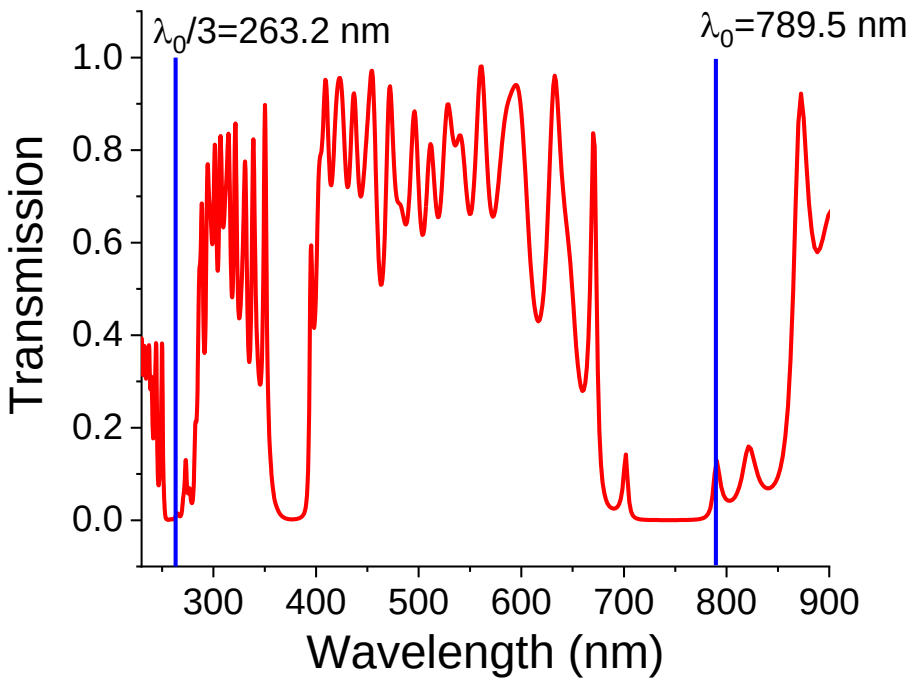

Figure 5.6: Calculated transmission spectrum of the optimum design S2, see Appendix C, with $N = 45$, optimized for incident Gaussian pulses with $\tau_p = 60$ fs at 787 nm.

We attribute the fact that local peak happening in the vicinity of the central wavelength of fundamental pulse to the resonance form of the optimum designs at fundamental regime that leads to the field enhancement. In addition, the transmission of the FTM near the TH pulse central wavelength of $\lambda_0/3 = 263.2$ nm is below 2%. This is not surprising, to have an efficient FTM mirror, the TH generated inside the stack in different layers have to be reflected for maximum TH outside the FTM.

5.4 FTM Design at the Critical Fluence

The A design is optimized for maximum conversion efficiency at the same incident fluence. The C design concept is based on the optimization of thin film layers to maximize the conversion efficiency of THG at maximum applicable fluence before the sample breaks down. In other words, C designs take into consideration the LIDT of materials, and basically are the optimum designs for maximum conversion at the same maximum internal fluence.

To take into account the fundamental field enhancement in the figure of merit for the optimization process, we followed the same steps as in deriving Eq. (4.3). We will use the capital letter Q to show stack properties. The conversion efficiency is now

$$\eta = \frac{U_{TH}}{U_F} = QU_F^2, \tag{5.21}$$

where, U_{TH},U_F are the energy of TH and fundamental pulses, respectively. The maximum TH conversion efficiency can be rewritten as follows:

$$\eta_{max} = \frac{Q}{f^4} U_{F,max}^2, \tag{5.22}$$

where f^2 is the peak of the fundamental field enhancement intensity at the moment (t_{peak}) when it is maximum, and the critical fluence (F_{crit}) is the maximum energy $U_{F,max}$ per area. Since, in practice the confocal parameter of the beam is much larger than thickness of the multilayer stack, the beam area is determined by the beam waist. Therefore, the energy and the fluence are related to each other through a constant, and both can be used.

The pulse intensity is a function of each position inside the stack z and time t, and f^2 is basically the maximum of this function in time and position over the incident intensity.

To calculate the f^2 of a pulse incident on a stack, we first take the Fourier transform of the pulse in time, and then propagate each individual spectral component inside the stack and find the amplitudes of each spectral component at the interfaces of layers, see appendix E. We then take the inverse Fourier transform of pulse in frequency domain to find the time evolution of electric field inside the stack, see appendix B.

Figure 5.7 shows the simulation results of designs that are optimized for maximum TH conversion efficiency respect to the number of layers. The C designs that are

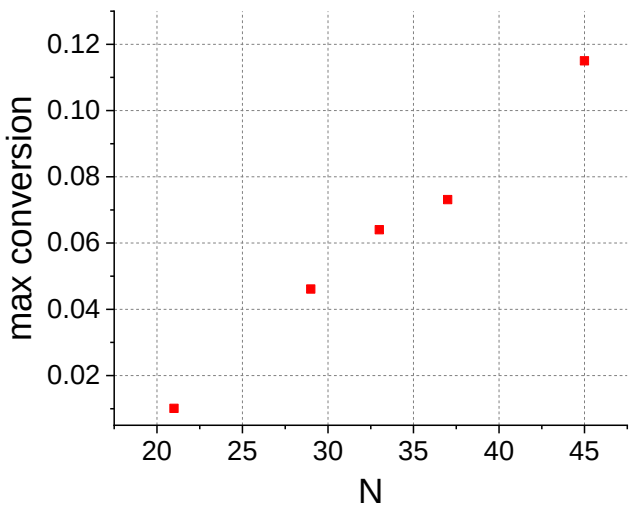

Figure 5.7: The maximum conversion efficiency of C designs optimized for incident 60 fs Gaussian pulses.

optimized for maximum conversion efficiency have a common feature with A designs, which is that more layers contribute to the output TH. However, in C designs, f^2 is lower compared to A designs, and also the layers that contribute to THG, have approximately equal maximum field enhancement intensity f^2. Figure. 5.8 shows a typical fundamental field intensity distribution at a time (t_{peak}) when it is maximum for an optimum design with $N = 45$.

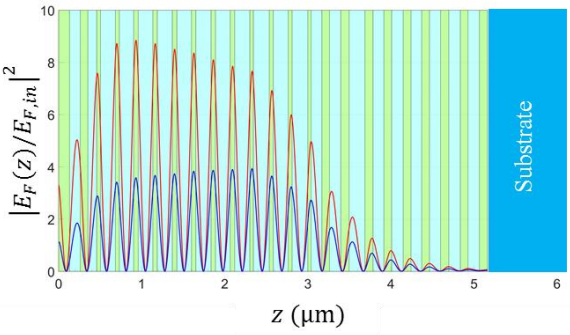

Figure 5.8: Normalized field intensity distribution (intensity enhancement) at time t_{peak} in an FTM of design C-type with $N = 45$ (see design S2 in appendix C) calculated with the pulse model (blue curve). At time t_{peak}, the intensity reaches a maximum inside the stack. For comparison, the red curve shows the intensity enhancement for monochromatic input at the same center wavelength (787 nm) as the pulse with a duration of 60 fs.

Unlike A designs, the local maximum in transmission line of a C design at the fundamental wavelength regime of a pulse does not always coincide with the central wavelength of the pulse.

The transmission at the TH regime is below 2% for the optimized designs that indicates the TH generated inside the stack will be reflected well.

5.5 Experimental Results and Interpretation

In this section, we will discuss the experimental results obtained with samples that are designed and optimized based on the pulse model, which includes the incident pulse bandwidth. The designs are optimized for the two available laser sources, see chapter 3, delivering different pulse durations at different central wavelengths.

5.5.1 The Samples Designed for Ti:Sapphire Oscillator

The Ti:Sapphire oscillator has a pulse train output with repetition rate of 110 MHz, where pulse duration of each individual pulse is 50 fs, centered at 787 nm. Note, the central wavelength of oscillator could be tuned over a stable 30 nm range, by moving in and out the prism in the laser cavity. To achieve spectrum beyond this range requires the realignment of laser components. A typical pulse spectrum at the oscillator output is shown in Fig 3.2. It shows the FWHM of the pulse spectrum is roughly 16 nm.

We designed two mirrors (both are C type designs) with 33 and 45 layers using the pulse model, where it is assumed that incident pulse has a temporal profile of a transform-limited Gaussian profile with pulse duration of 50 fs, centered at 787 nm.

The architecture and field distribution of FTMs with $N = 33$ layers (structure - Hafnia/(Silica/Hafnia)^{16}/substrate) and for $N = 45$ layers
(structure Hafnia/(Silica/Hafnia)^{22}/substrate) are shown in are shown in Fig. 5.9(a) and in Fig. 5.9(b).

The field intensity distribution for monochromatic (red curve) and pulse at time t_{peak} (blue curve) are shown in Fig. 5.9(a) and 5.9(b). The monochromatic fundamental field enhancement is always larger than the fundamental field enhancement at the maximum moment taking into account the pulse spectrum. Although, the electric field at the central wavelength of the pulse is in phase inside a multilayer structure, the spectral component stretching to shorter and longer wavelengths will have different phase acquisition. This is also critical for broadband short pulses, where even the local maxima of field distribution of the pulse intensity at the maximum moment does not coincide with the monochromatic field distribution. In the design of FTMs, for them to perform efficiently at fluences close to critical fluences (C designs), one needs to take into account the pulse intensity at the maximum moment.

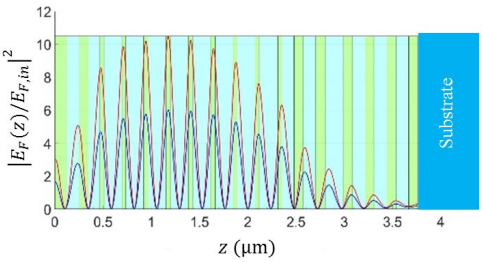

(a)

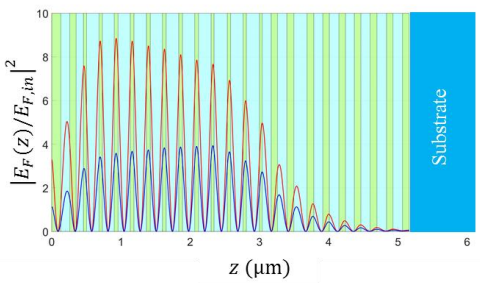

(b)

Figure 5.9: Normalized intensity distribution (intensity enhancement) at time t_{peak} in an FTM of design C (a) S1 with $N = 33$, and (b) S2 with $N = 45$ calculated with the pulse model (blue curve). At time t_{peak}, the intensity reaches a maximum inside the stack. For comparison, the red curve shows the intensity enhancement for monochromatic input at the same center wavelength (787 nm) as the pulse with a duration of 60 fs. The output of oscillator were 60 fs during the experiment.

The samples are fabricated with ion-beam sputtering by our collaborators in Hannover [32, 33]. The designed FTMs are coated with about 1 nm uncertainty in the thicknesses of the layers. The effect of uncertainty in the thickness of layers are simulated by generating 1000 designs from original design, with introducing randomness of ±1 percent of the thickness of any layer to its original value. We used 1% rather than 1 nm to consider the higher uncertainty specially for thick layers (> 100 nm) . The histogram of the value of calculated TH conversion for each design out of 1000 design are shown in Fig. 5.10(a) for S1 with $P_{50-100} = 1$, and 5.10(b) for S2

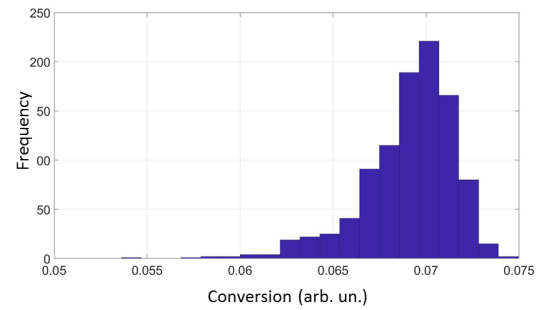

(a)

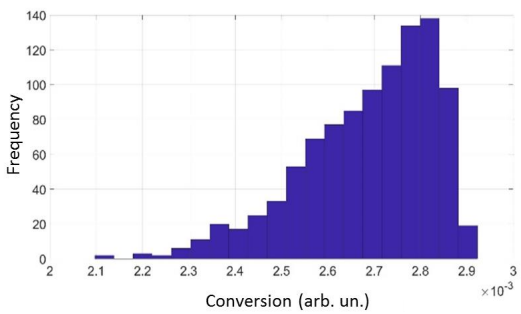

(b)

Figure 5.10: The histogram of TH conversion efficiency of 1000 designs generated with random thickness fluctuations starting from an optimized design (a) S1 with $N = 33$ and conversion $= 0.075$, (b) S2 with $N = 45$ and conversion $= 0.0029$.

with $P_{50-100} = 1$, see section 4.7. They show that the TH conversion of 50 percent of the generated designs are above the 80% of TH conversion of the original design. Therefore thickness uncertainty that exists during the fabrication shouldnt affect the THG dramatically. This is different from the monochromatic designs.

The experimental setup to measure TH conversion of the fabricated samples are shown in Fig. 5.11. The single shot and multiple shot (6 pulses in each burst) are done on fresh spots on the sample. The incoming fundamental pulse passes through a dichroic mirror (DM) and is focused onto the sample using an aspheric lens with

focal length of $f = 1.5$ cm. Using an aspheric lens allows us to reach fluences above the damage threshold (150 mJ/cm^2) of the sample. The maximum average power before the DM is 1.1 W that results in fluences of 250 mJ/cm^2 on the sample [34].

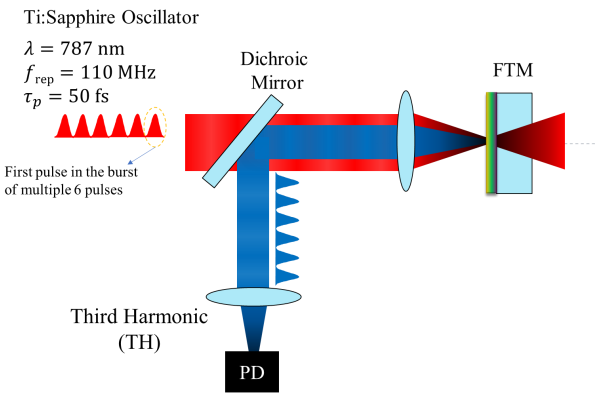

Figure 5.11: Schematic diagram of the experimental setup to measure TH in reflection from FTMs (S1 and S2). The illumination is by bursts of up to 6 pulses with central wavelength of 787 nm, repetition rate of 110 MHz, and pulse duration of 60 fs.

The experimental setup in Fig. 3.2 is used to test the samples S1 and S2. The TH conversion efficiency was measured for a single pulse and bursts of pulses. The results are shown in Fig. 5.12. At low fluences, the TH conversion efficiency scales with the second power of the incident fundamental energy. The absolute value predictions of the TH conversion efficiency based on the pulse model agrees with the experimental results. At high fluences, the TH conversion efficiency diverges from the square law. The physical mechanism that leads to this deviation is electron-plasma formation that occurs at these high fluences and constrain the THG. Here, low fluence means a regime below the expected damage threshold of the mirror based on measurements on single layers, taking into account the fundamental field enhancements. We will discuss in detail the response of FTMs near the damage threshold in the next chapter.

The pulse model predicts that both samples S1($N = 33$) and S2 ($N = 45$) should

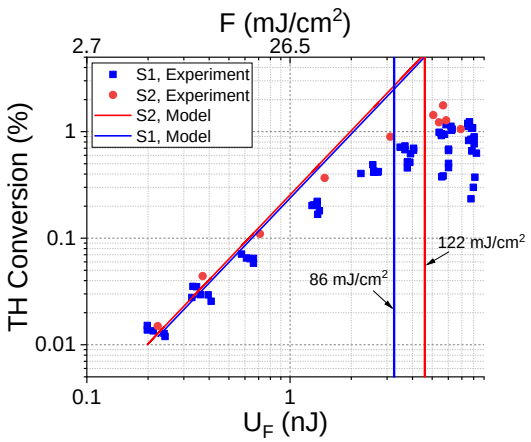

Figure 5.12: Measured and predicted TH conversion efficiencies of samples S1 ($N = 33$), and S2 ($N = 45$) as a function of the single-pulse energy (U_F)and fluence (F) in a burst of 6 pulses. The vertical lines at 120 and 150 mJ/cm^2 show the damage threshold of sample S1 and S2, assuming a field intensity enhancement of $f^2 = 5$, $f^2 = 4$ at t_{peak}, respectively. Using these enhancement values the critical fluences were calculated from the known LIDT values of single Hafnia films [1].

show almost equal TH conversion at the same incident fluence, which is consistent with experimental results at low fluences (where conversion scales with square of fundamental fluence), see Fig. 5.12. However, at high fluences, we see that the TH conversion efficiency of sample S1 diverges with higher rate compared to sample S2. Figure. 5.5.1 shows that S1 has a higher fundamental field enhancement (at the moment that maximum enhancement happens) compared to S2. It means that at the same fluence, the inner layers in sample S1 will experience higher fluences, $E_{F,internal} = f^2 \times E_{F,incident}$. Hence, the degrading mechanism for THG will trigger earlier in sample S1 than in sample S2. This result also points out the importance of taking into account the field enhancement in the optimization process, which we did in C designs. From a practical point of view, it is the internal fluence($F_{internal} = f^2 \times F_{incident}$) that determines the upper limit for fluence, not the fluence incident on the sample.

5.5.2 Samples Designed for the Femtosecond Pulse Amplifier

The design S2 ($N = 45$) optimized for a pulse central wavelength of 787 nm was modified through an optimization process for a central wavelength of 815 nm for transform limited Gaussian pulses with 60 fs, resulting in FTM S3. The structure of the design S3 with 45 layers is Hafnia/(Silica/Hafnia)^{22}/substrate. The structure and field intensity distribution of the design S3 is shown in Fig. 5.13.

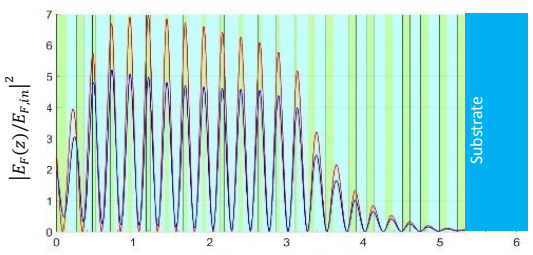

Figure 5.13: Normalized field intensity distribution (field intensity enhancement) at time t_{peak} in an FTM of design S3 with $N = 45$ calculated with the pulse model (blue curve). At time t_{peak}, the intensity reaches a maximum inside the stack. For comparison, the red curve shows the intensity enhancement for monochromatic input at the same center wavelength (815 nm) as the pulse with a duration of 60 fs.

The field intensity distributions for monochromatic and pulses (at time t_{peak}) are shown in Fig. 5.13. The structure of S3 resembles the samples S1 and S2 shown in Fig. 5.9(a) and Fig. 5.9(b). The fabrication process is explained earlier. The effect of layer thickness uncertainties is shown in Fig. 5.14.

The experimental setup to measure TH efficiency was already shown in Fig. 5.11. However, we used the output of a multi-pass amplifier to excite the sample instead of an oscillator. The amplifier produces pulses with 1 kHz repetition rate, centered at 815 nm with pulse duration of 42 fs. As an example, the spectrum of output pulses is shown in Fig. 5.15. It should be mentioned that the pulses at the output of the

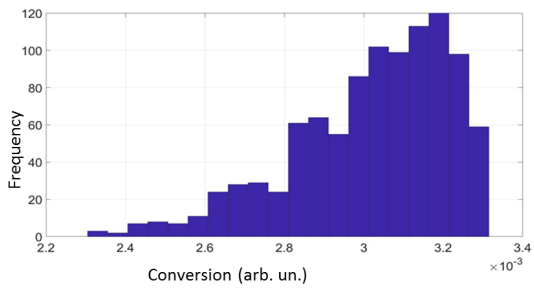

Figure 5.14: Histogram of TH conversion efficiency of 1000 designs generated with random thickness fluctuations starting from an optimized design S3 with $N = 45$ with conversion = 0.0033.

amplifier are not transform limited. The shortest pulse duration achievable using the grating compressor right before the amplifier output was 42 fs.

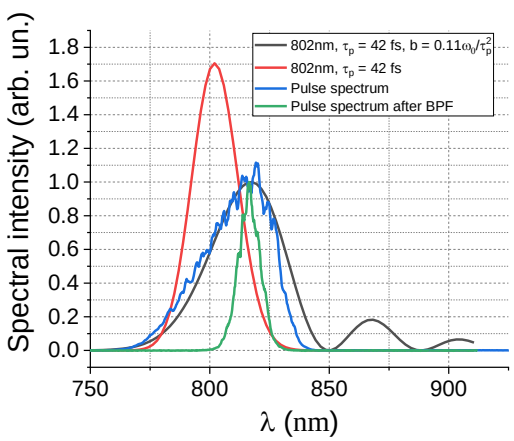

Figure 5.15: Measured spectrum of the amplifier output pulse (blue curve) and of pulses after a band-pass filter (BPF, green curve). The spectra of a transform-limited Gaussian pulse at 802 nm (red curve) and a chirped pulse (black curve) are also shown. Note, the amplitudes of spectral intensity are shown in scale at the same pulse energy for both 802 nm, $\tau_p = 42$ fs, with and w/o $b = 0.11\omega_0/\tau_p^2$.

The TH conversion efficiency of the sample relative to the incident pulse energy

is shown in Fig. 5.16. At low incident fundamental pulse energies, the TH conversion scales the with second power of the fundamental pulse energy. As the energy of the fundamental pulse increases, near the damage threshold, the conversion efficiency of TH does not follow the second power rule. We will discuss this in detail in the next chapter. The model predictions are also shown in Fig. 5.16.

In the model, we assumed for the complex field amplitude of the chirped pulse:

$$E(t) = e^{-2\ln 2\frac{t^2}{\tau_p^2}} e^{-ibt^3}, \tag{5.23}$$

where b is a chirp parameter. For a chirp parameter of $b = 0.11\omega_0/\tau_p^2$, $\tau_p = 42$ fs and a central wavelength of 802 nm the corresponding pulse spectrum (black curve) roughly resembles the measured spectrum (blue curve), cf. Fig. 5.15.

Using this chirped pulse electric field as input in the pulse model, the TH conversion efficiency of sample S3 is shown in Fig. 5.16. For the case of a transform limited Gaussian pulse with pulse duration of 42 fs centered at 815 nm, the predicted TH conversion will be 12 times that of a chirped pulse. Note, this factor would applies to low fluences, where TH conversion efficiency still follows the second power of fundamental pulse energy. At high fluences, the fundamental field enhancement of the incident pulse inside the stack will determine the maximum achievable TH conversion, which is factor of 10.

In a subsequent experiment, a band pass filter (BFP) with transmission bandwidth of 14 nm is placed in front of the fundamental pulses. The spectrum of the filtered fundamental pulse is shown in Fig. 5.15. The TH conversion efficiency relative to the energy of the filtered fundamental pulse is also shown in Fig. 5.15. The prediction with model agrees with the experimental values at low fluences. The maximum conversion efficiency of 1.8% was obtained at a fundamental pulse energy of 1 μJ, which corresponds to a fluence of 160 mJ/cm^2.

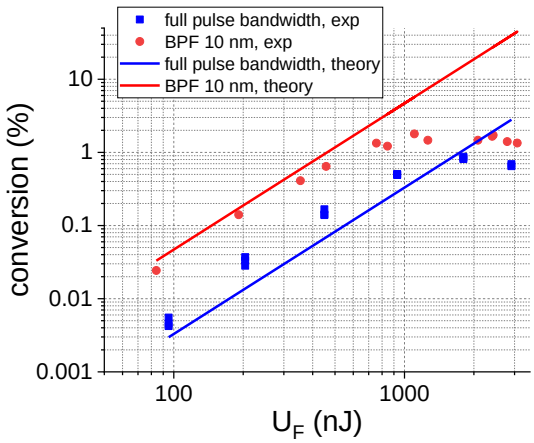

Figure 5.16: Measured TH conversion efficiency of sample S3 obtained with the full pulse spectrum (blue squares) and filtered pulse spectrum (red circles). The lines represent modeling results.

5.6 Summary

An FTM design model was developed that takes into account the spectral properties of short pulses and their effect on THG in layered structures. The pulse model shows that the absolute value of the TH conversion efficiency does not grow with $1/\tau_p^2$ for FTMs with design bandwidths smaller than the incident pulse bandwidth. Optimum designs based on the pulse model have a larger conversion bandwidth compared to their monochromatic counterparts at the same q_A value. The pulse model predictions are in agreement with experimental result at low fluences. At high fluences, in the vicinity of the damage threshold, the experimental values diverge from the model. This will be discussed in the next chapter, chapter 6. An FTM with a TH conversion efficiency of about 1.8% was demonstrated.

Chapter 6

Material Modification

In the previous chapters, we saw that the TH conversion efficiency does not scale with the square of the fundamental pulse energy at high fluences, resulting in efficiencies well below the predictions. In this chapter, we will discuss the physical origins of these discrepancies in more detail for single and multiple pulse illumination.

In the first part, the stability of the TH signal from an FTM under continuous illumination with a pulse train will be discussed. It will be explained in detail how the optical property of layers in a stack of thin films varies, and how this modification effects TH signal. The sources of this modification, and the physical mechanisms behind will be studied.

In the second part, the TH signal from an FTM at fluences close or above the damage threshold is studied for illumination with single pulses.

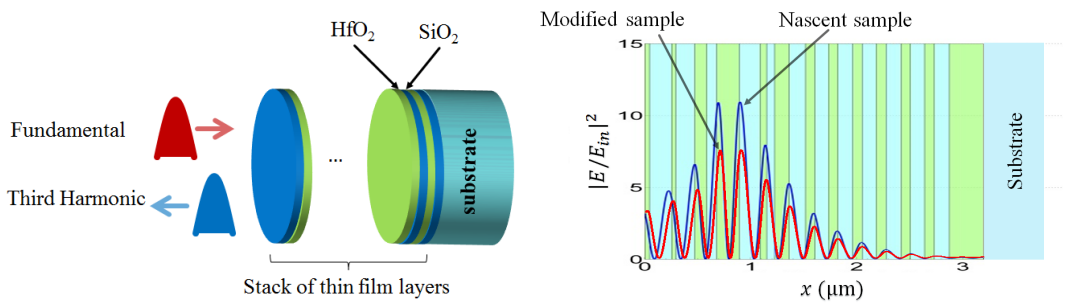

(a) (b)

Figure 6.1: (a) Third harmonic generation using the frequency tripling mirror consisting of a stack of hafnia and silica thin films. (b) Standing fundamental field intensity distribution in the stack of the original mirror and after laser-induced modifications, see text.

6.1 The Frequency Tripling Mirror Illumination by Pulse Trains

The FTM used for these experiments consists of 12 pairs of hafnia/silica films with an additional hafnia film on the substrate, see Fig. 6.1(a). The thicknesses of the individual layers are optimized for THG in reflection [24], see the design OS in appendix C for more detail. A train of femtosecond pulses is incident ($\lambda = 791$ nm) and TH radiation at 264 nm is detected in reflection, cf. Fig. 3.1 for the experimental setup.

The FTM under consideration has the structure of a Fabry-Perot (see Fig. 6.1(b)) that leads to a fundamental field enhancement in the thick hafnia layer. The mirror was optimized with the monochromatic model for design A.

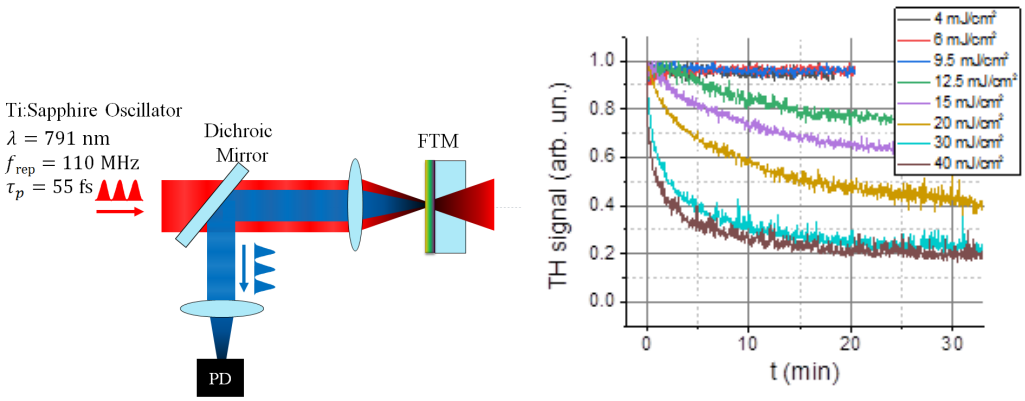

(a) (b)

Figure 6.2: (a) A train of pulses from a modelocked Ti:Sapphire oscillator is incident on a frequency tripling mirror. The third-harmonic radiation is detected in reflection by an avalanche photodiode (PD). (b) Third harmonic power as a function of time for different incident fluences.

6.1.1 Laser Induced Material Modifications

The experimental setup for THG from an FTM is shown in Fig. 6.2(a). The pulses from a fs pulse oscillator (791 nm, 110 MHz, 55 fs) are focused onto the sample with an aspheric lens and the TH is collected in reflection. Figure. 6.2(b) shows the normalized TH power as a function of time for different incident fluences of the fundamental pulse. The TH signal decreases on a time scale of min utes under continuous illumination before leveling off at about 20% of the initial value. Obviously, the material changes over time caused by the incident laser. The observed modifications are long-lived. After 24 hours without laser illumination, the THG efficiency was still the same as after 30 min.

6.1.2 Characterization of the induced material modifications

To assess possible laser induced substrate modifications we illuminated a bare material over several hours with the highest fluence available. We could not detect any long-lived change in transmission and reflection. To decide whether the incident fundamental wave, the generated TH or both are responsible for the material modification in the dielectric stack we performed two additional experiments. First, we illuminated the sample with circularly polarized light. TH in this case is not generated in an ideal isotropic medium [7] and consequently only a small amount ($10^{-5}\times$ the value for linear input polarization) was observed. Yet, the material was modified, albeit at a lower rate. The polarization effect of fundamental beam on material incubation has previously been studied [35]. These observations suggest that the fundamental radiation causes the observed incubation effects. Second, we tuned the fundamental wavelength from 791 nm to 756 nm and 815 nm and could not observe any laser induced modifications. For the same incident power the field enhancement at the detuned wavelengths is about 7 times smaller in the film that sees the maximum field. An obvious conclusion is that the material is modified by the fundamental pulse train and the layer with the highest field plays the dominant role in the observed change of the optical response.

The modified sample area was inspected first using Nomarski, transmission and reflection microscopy. While a spot on the sample was clearly visible, the signal to noise ratio was not high enough for a quantitative analysis. We therefore performed transmission and reflection measurements with a low fluence / power probe beam. The experimental setup is shown in Fig. 6.3. The sample was translated along the focused probe beam (direction z) while transmission $t(z)$ and reflection $r(z)$ were recorded. The results are shown in Fig. 6.4(a), and 6.4(b).

The maximum transmission and reflection change is observed when the sample is

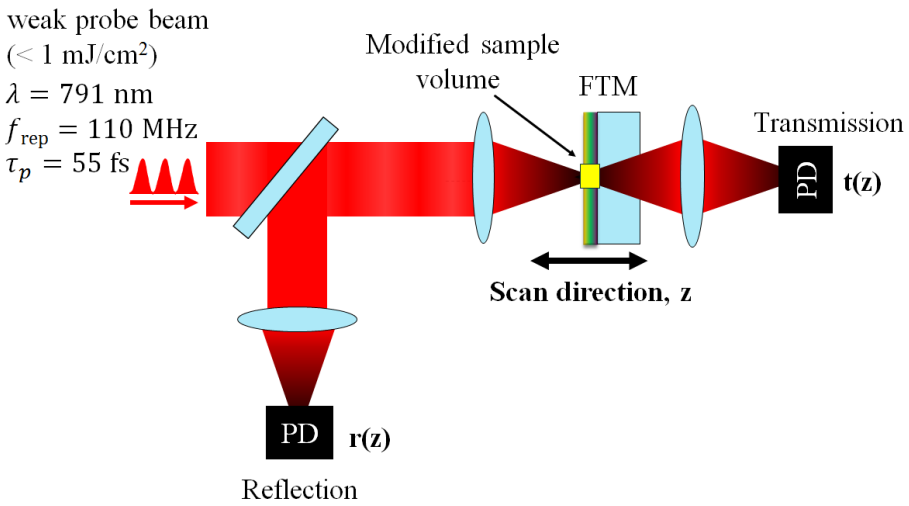

Figure 6.3: Measurement of transmission and reflection of a focused probe beam as a function of the sample position z. The waist of the focal spot was $w_0 = 6.2$ μm.

in focus, that is, when the spatial overlap of modified material and the probe beam is optimal. Although the relative change in reflection is about 10 times smaller than in transmission, the net change in absolute reflection and transmission is zero,

$$\Delta r + \Delta t \approx 0, \tag{6.1}$$

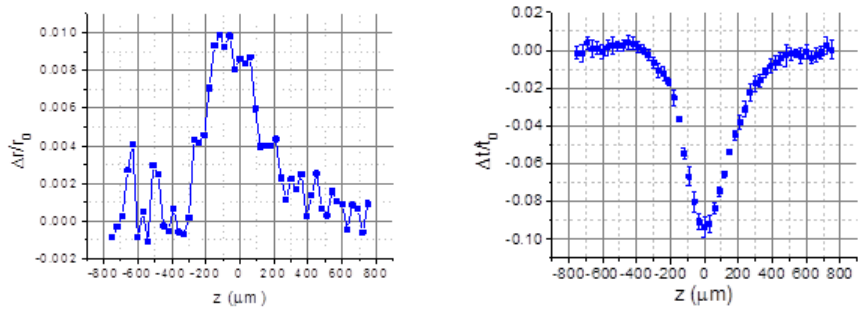

(a) (b)

Figure 6.4: (a) Reflection and (b) transmission change as a function of the sample position (at $z = 0$ the dielectric stack is in the focus of the probe).

where, $\Delta r = 0.1$, and $\Delta t = -0.1$. This means that, within experimental error, the induced modification changes only the real part of the refractive index.

The question arises what physical processes are triggered by the fundamental that give rise to this long-lived index change. Energy must be deposited to facilitate material modifications. A good indicator of the energy deposition of non-fluorescing samples is the temperature change during illumination. Figure 6.5(b) shows the experimental setup and the measured temperature change as a function of the incident mean power of the femtosecond pulse train.

For CW illumination, no measurable temperature increase is observed with the thermal camera. The linear absorbance is below the limit determined by the sensitivity of our detection apparatus. For the modelocked pulse train, a temperature change $\overline{\Delta T}$ of 1.4 K at the highest average power was detected. To relate $\overline{\Delta T}$ to an absorption we need a thermal model of the experimental situation. If we assume an infinitely thin absorbing film on a fused silica substrate illuminated by a CW Gaussian beam of power P and beam waist w, the temperature change in the volume of sample from time $t = 0$ s until t is [36]:

$$\Delta T(r,z,t) = \frac{AP}{2\pi^{3/2}\rho c\sqrt{D}} \int_0^t \frac{\exp\left[-\left(\frac{r^2}{2w^2+4Dt'}\right)-\left(\frac{z^2}{4Dt'}\right)\right]}{\sqrt{t'}(w^2+2Dt')}dt' \tag{6.2}$$

Here A is the absorbance of the film. $\rho = 5.71$ g/cm^3, $c = 0.522$ J/(g K), and $D = 34.3$ cm^2/s are density, specific heat, and diffusivity of fused silica, respectively. r and z are cylindrical coordinates and t is the illumination time. In the derivation of Eq. (6.2) the substrate is assumed semi-infinite, because the beam size is negligible compared to the substrate size. Note, the spatial resolution of our thermal camera is about 25 μm. This means the central pixel averages over parts of the temperature profile, and the temperature increase at $z = 0$ and $r = 0$ over a long enough time is about 3 times higher than what is shown in Fig. 6.5(b). Using this peak temperature allows us to associate an absorbance with the measured temperature increase using

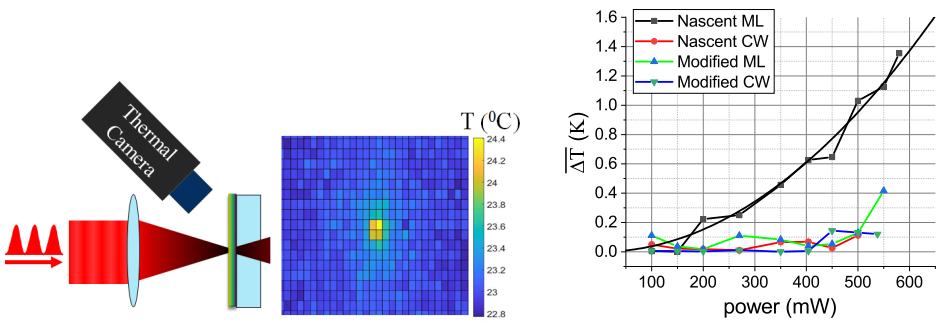

(a) (b)

Figure 6.5: (a) Measurement of the temperature in the vicinity of the laser focus using a thermal camera (FLIR A325). (b) Peak temperature as a function of the incident average power. The error bar of data points are ±0.1 K. Note, 100 mW corresponds to a single pulse fluence of 1.5 mJ/cm^2. The temperature increase of the nascent and modified sample for incident continuous wave (CW) and modelocked (ML) laser radiation at 791 nm is compared.

Eq. (6.2).

Figure 6.5(b) suggests that the absorbed power of the nascent material varies quadratically with incident power, which points to a two-photon absorption process. In this case the absorbance A of the sample is proportional to the incident pulse fluence. In our case, at an incident averaged (over the pulse train) power of 600 mW, $A \approx 290$ ppm.

For a two-photon absorption process the pulse intensity is governed by

$$-\frac{dI}{dz} = \beta I^2 \tag{6.3}$$

In Eq. (6.3), the intensity I corresponds to the Hafnia layer of sample OS that has the highest fundamental field enhancement.

If we make the simplifying assumption that 2-photon absorption occurs only in the layer of the highest field enhancement, we can estimate the two photon absorption coefficient and obtain $\beta \approx 70$ cm/TW. We couldn't find any TPA measurement in

a Hafnia film. The TPA coefficient of Ta_2O_5, a similar metal oxide albeit with a smaller bandgap, was measured to be 4.3 cm/GW [37]. For bulk Al_2O_3, another metal oxide similar to Hafnia a TPA coefficient of about 90 cm/TW was measured [38].

Due to the decrease in field enhancement, the absorbed power is smaller for the modified sample, cf. Fig. 6.5(b). Note that in such samples the resonance wavelength is shifted by the induced index change as will be discussed next..

6.1.3 Interpretation and Discussion

Since the absorption triggering the material modification is nonlinear, the layers that see the largest intensity play the dominant role in the measured TH, and the observed reflection and transmission change. The standing intensity distribution in the film stack was shown in Fig. 6.1(b). The peak intensity occurs in one, relatively thick, layer. Let us therefore assume that the material (refractive) index is only modified in this layer:

$$n = n_0 + \Delta n \tag{6.4}$$

The layer thicknesses of the FTM are well known. The change in reflection, transmission, TH efficiency, and nonlinear absorption are shown in Fig. 6.6. There are two areas, labelled D_1 and D_2, where the predicted values agree with the experimental observation. For the layer of interest (with the highest field intensity enhancement), Δn can predicted. Conversely, Δn can be found by requiring that the measured and modeled Δr and Δt are in agreement. From this, we find $\Delta n \approx 0.07$ describes the sample state at the asymptotic value of the TH, cf. Fig. 6.2(b). The sign of Δn was determined by comparing the modeled (Fig. 6.7(b)) and measured (Fig. 6.7(a)) spectrum of the transmitted pulse. A positive index change corresponds to a red

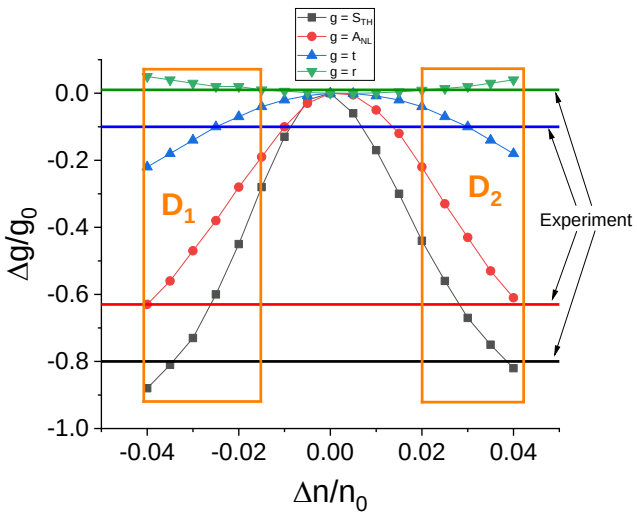

Figure 6.6: Calculated relative change in FTM parameters as a function of the relative index change. The parameter g stands for TH signal(S_{TH}), nonlinear absorption (A_{NL}), transmittance (t), and reflectance (r) relative as indicated. Experimentally determined single values of $\Delta g/g_0$ are shown with straight lines to see the crossing with predicted values.

shift of the spectrum, which was observed. It should be noted that a laser induced index change was also evident from earlier time-resolved pump-probe measurements [39]. The reason why an index change leads to a dramatic decrease of the TH power is two-fold:

1. the field enhancement inside the hafnia layers decreases, cf. Fig. 6.1(b), and thus reducing the nonlinear optical processes, and

2. the phases of the TH fields generated in the individual layers do not add up in phase anymore because of the now less than optimal phase shift in the modified layer.

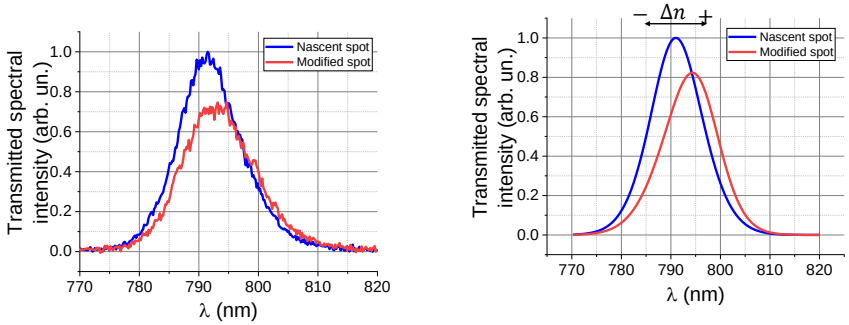

(a) (b)

Figure 6.7: (a) Measurement of the transmission spectrum of fundamental beam at a nascent, and modified spots (b) Predicted transmitted spectrum of fundamental beam through the original FTM, and a modified FTM(real part of refractive index of hafnia layer is increased by 0.07).

As a test, we used $\Delta n = 0.07$ and the two-photon absorption parameter $\beta = 70$ cm/TW (cf. Eq. (6.3)) to estimate the change in absorption (heating) taking into account the change in the standing field in the stack after material modification (cf. Fig. 6.1(b)). At an average power of 600 mW (pulse train with $RR = 110$ MHz, and average energy of each pulse 5.4 nJ), we obtain a temperature change of the modified spot (averaged over the camera pixel area) of $\overline{\Delta T} \approx 0.4$ K from the experiment and the two-photon absorption model using $\beta = 70$ cm/TW. For the same parameters and taking into account the $\Delta n = 0.07$ for layer 7, our model yields $\overline{\Delta T} \approx 0.6$ K, which agrees within experimental error with the measurement, cf. Fig. 6.5(b). In addition, when we model the TH from the modified stack (layer 7 with $\Delta n = 0.07$) we reproduce the observed drop (Fig. 6.2(b)) in TH conversion efficiency within experimental error.

6.1.4 Possible fundamental material properties consistent with 2-photon absorption

Direct band-to-band excitation of hafnia (bandgap $E_g \approx 5.8$ eV) requires a 4-photon absorption of 800-nm light. However, hafnia is known to have several possible mid-gap states associated with oxygen vacancies [2]. These states can mediate excitation of conduction band (CB) electrons via a two-step, two-photon absorption process. Most of the heating would occur through excitation and subsequent relaxation of these intermediate states and the temperature increase thus is expected to show the quadratic behavior shown in Fig. 6.5(b).

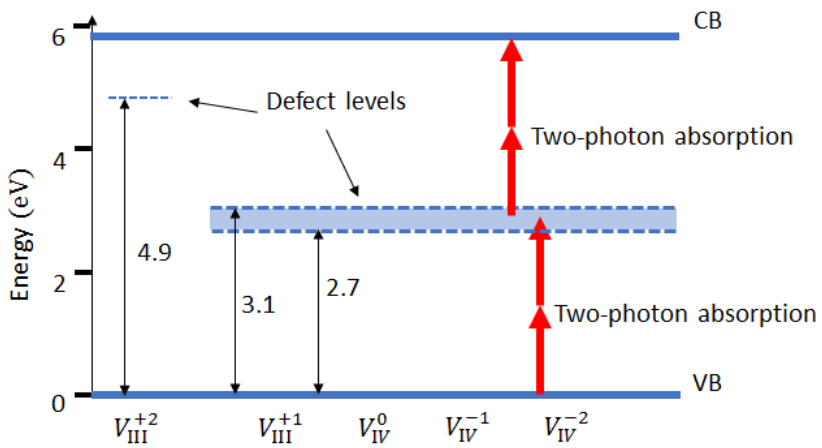

Figure 6.8: Kohn-Sham energy levels for neutral and charged oxygen vacancies in m-HfO_2. Two charged states ($q = +1, +2$) for threefold V_{III}^{q} and three charge states ($q = 0, -1, -2$) for fourfold V_{IV}^{q} coordinated oxygen vacancies. Adapted from reference [2]. The valence (VB) and conduction (CB) edges are indicated as well as possible two-photon absorption processes.

Long-lived states causing the index change in question are likely a result of relaxation of electrons out of CB. This has been suggested previously [40, 41] and is the cornerstone of incubation processes that control for example the multiple pulse (S on 1) LIDT in optical elements based on stacks of dielectric films. Only a relatively

small number of CB electrons are excited through multi-photon absorption process and therefore the contribution to the temperature change can be neglected.

We believe these long-lived states may be due to creation of oxygen vacancies in the material that are been suggested perviously [2]. The change in the density of these defects would lead to material change or consequently refractive index change, which is consistent with the change in transmission and reflection.

6.2 TH Signal of an FTM at Single Shot Excitation

So far we have studied FTM under continuous illumination, however even for single pulse illumination, the TH signal does not scale with the third power of the fundamental energy. To evaluate this situation in more detail we will use the FTM sample O3R (see appendix C). This FTM consists of a stack of 25 high and low index dielectric films made from Hafnia and Silica, whose individual thicknesses are designed for maximum TH generation in reflection using the monochromatic model, see Fig. 6.9.

6.2.1 Experimental Results

TH Energy as a Function of Input Energy

The TH energy produced by an FTM was measured using a 42-fs laser system operating at 815 nm at a repetition rate of 1 kHz. A Pockels cell(embedded inside the amplifier Fig. 3.4) picked bursts of pulses for excitation, see Fig. 6.10.

Figure 6.11(a) shows the TH energy as a function of the input energy for the first

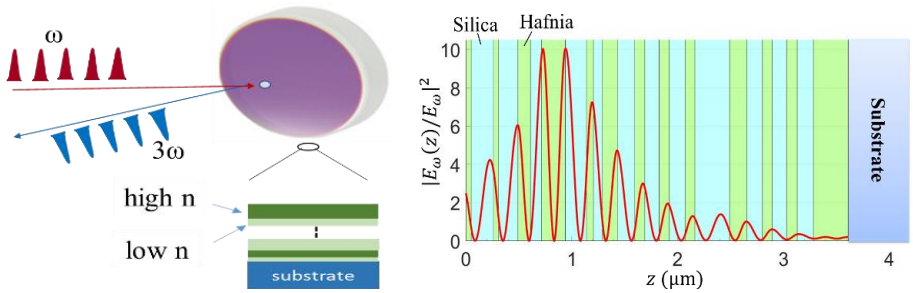

Figure 6.9: Schematic diagram of THG using a frequency tripling mirror (FTM). Standing (fundamental) field intensity distribution in an FTM sample O3R(see appendix C) with 25 layers.

six pulses of the burst. Each burst illuminated a new sample site. It can be seen that just before the LIDT is reached the TH energy starts to scale more slowly with increasing fundamental energy than what is expected from a third order nonlinear optical process. This scaling gets even slower for fundamental energies well above the single pulse LIDT. The single pulse LIDT of the mirror was determined with the crater size method [3]. The area within the beam where the fluence exceeds the damage fluence (area of the crater), F_{th}, for an incident pulse fluence F can be written as

$$A_c = 2A_b \ln(F/F_{th}), \tag{6.5}$$

where A_b is the area of the Gaussian beam. A representative Nomarski image of a crater and the crater area versus fluence are shown in Fig. 6.11(b). The damage threshold fluence is obtained from extrapolating to the fluence at which the crater area is zero. It should be noted that the crater develops after the pulse. This is the main reason why we observe TH for fluences $F > F_{th}$. For the first pulse we obtain TH from the highly excited, but still intact, film. For the second and the following pulses there are still film layers remaining and the developing crater does not fully cover the beam area. This gives rise to the still nonzero TH for high fluences.

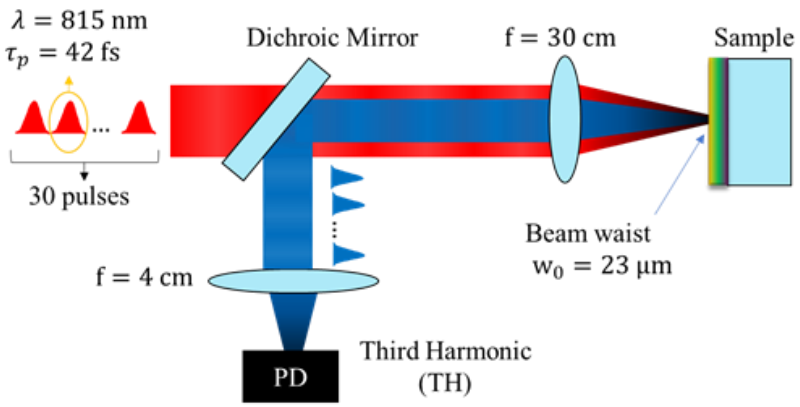

Figure 6.10: Measurement of TH energy as a function of the input energy (fluence). The input pulse energy was varied using a half-wave plate - polarizer sequence (not shown).

TH Spectra at Different Input Fluences

We investigated the spectrum of the TH for increasing incident fluence and different spectral widths of the fundamental. The results are summarized in Fig. 6.12(a),

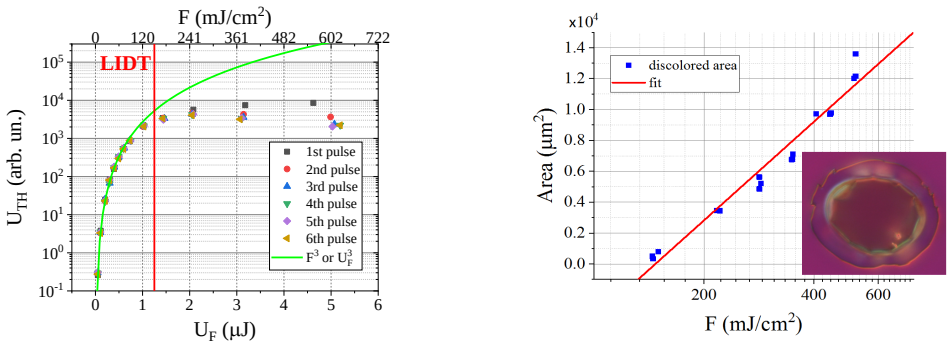

(a) (b)

Figure 6.11: (a) TH energy (U_{TH}) as a function of input energy (U_F), or fluence (F). (b) The LIDT was measured using the crater size technique [3]. A threshold of $F_{th} \approx 0.15$ J/cm^2 was obtained by extrapolation of the crater area to zero.

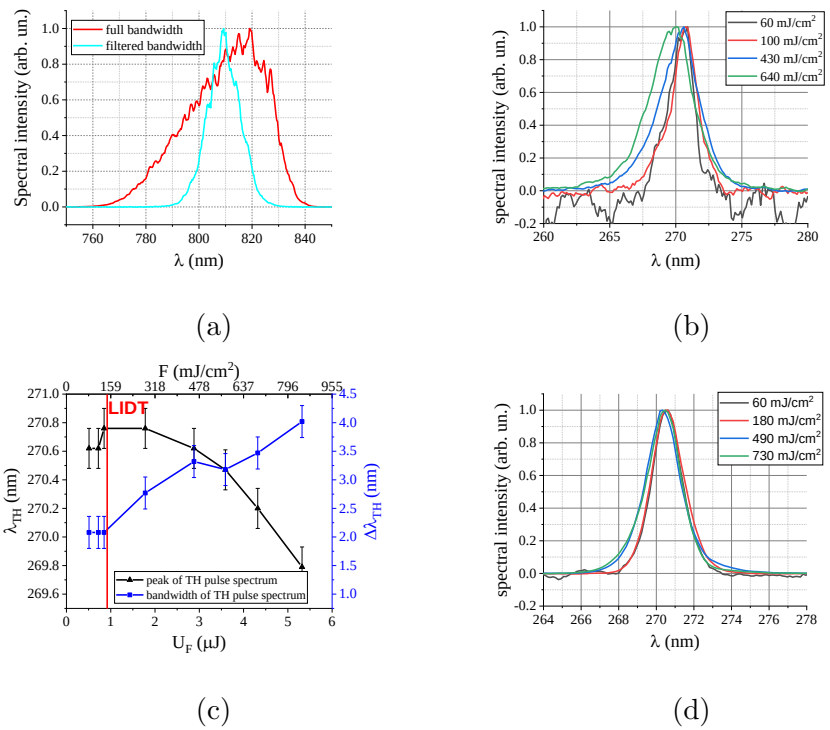

Figure 6.12: (a) Full bandwidth of our amplified fs pulses and bandwidth after an interference bandpass filter. (b) Spectra of TH for different incident fluences (full bandwidth). (c) Measured width of the TH spectrum and TH center wavelength as a function of the fluence of the fundamental (full bandwidth). (d) TH spectra for different input fluences (reduced bandwidth). The pulse duration were 42 fs, 64 fs for full and reduced bandwidth, respectively.

6.12(b), 6.12(c), and 6.12(d).

The peak of the TH spectrum shifts to shorter wavelengths (blue shift) at high fluences if the full bandwidth was used. Also, the bandwidth of the generated TH pulses increases with fluence. A bandpass filter at 810 nm is used to narrow the pulse spectrum, see Fig. 6.12(a). The TH spectral broadening and blue-shift for the filtered fundamental pulse are negligible compared to the case when the full pulse spectrum was used.

6.2.2 Interpretation and Discussion

As discussed earlier, in the small-signal limit (no pump depletion), the TH should grow with the cube of the fundamental power up to the laser-induced damage threshold (LIDT). This is not what we observed, cf. Fig. 6.11(a). There are several possible reasons why a deviation from the ideal power law can be expected for high input fluences even for illumination with one or a few pulses. It should be noted this case is different from the condition discussed earlier in this chapter, where we had a train of pulses illuminating the sample with a repetition rate of 110 MHz over a long time.

The deviation of the TH conversion efficiency from square-law scaling with fundamental fluence has its origin in nonlinear processes that occur during a single pulse. Potential detrimental nonlinear processes for FTMs under single pulse excitation are (i) creation of an electron-hole plasma, (ii) multi-photon absorption and (iii) the optical Kerr effect. We will discuss them briefly and summarize their estimated effect on the complex refractive index for one FTM example and one incident fluence in Table. 6.1. All these processes result in a change of the complex refractive index. This may lead to absorption, a change in the standing field distribution in the multilayer stack, cf. Fig. 6.9, and the phase-mismatch controlling THG. To first order we can assume that only the high-index (hafnia) layer is affected in which the standing wave produced the highest intensity.

Recall that the FTM is a resonant structure, see section 4.3, and a change in the refractive index will also change the wavelength at which the TH spectrum peaks. Typical bandwidths of FTMs are on the order of 4-6 nm corresponding to the conversion of fundamental pulses with a bandwidth of 8 to 12 nm.

Figures 6.13(a) and 6.13(b) show the calculated TH signal as a function of the change in (a) the real and (b) the imaginary part of the refractive index at the fundamental wavelength in the 227-nm thick hafnia layer with the highest intensity

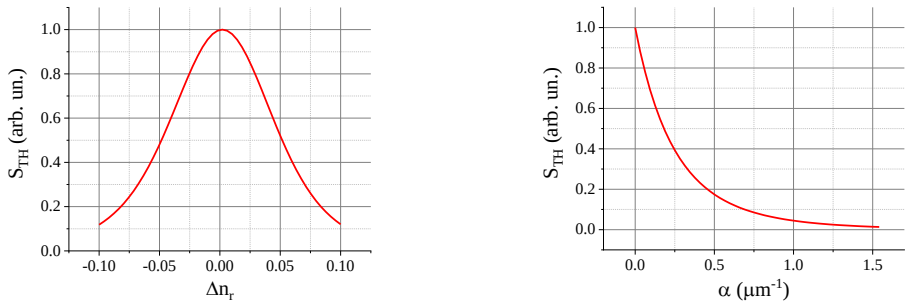

(a) (b)

Figure 6.13: Calculated TH energy as a function of (a) the deviation of the real part of the refractive index form the value used in the FTM design, and (b) the imaginary part of the refractive index at the fundamental wavelength. What we show in (b) is the corresponding small-signal absorption coefficient, and we assume a film thickness of 227 nm The response of the whole FTM was calculated even though the real index change and the induced absorption were assumed only for the layer with the maximum standing field intensity.

of the 25-layer stack under consideration, cf. Fig. 6.9. Previously in this chapter we discussed multi-photon absorption in dielectric films [1, 42]. For our hafnia films of interest, we identified two-photon absorption as the dominant loss process for fluences close to LIDT, and determined the corresponding two-photon absorption coefficient $\alpha = \beta I$, where $\beta \approx 70$ cm/TW [6], see section 6.1.2. As is well-known from LIDT models, short laser pulses excite electrons from the VB to the CB [43] through high-field ionization [44]. To first order, the CB electrons form a plasma changing the complex refractive index of the film. This index change was measured with time resolution previously [39]. Table. 6.1 lists Δn_r and α (at the pulse peak intensity).

Figure. 6.14 shows a schematic diagram of how electron-plasma formation may lead to spectral broadening of the TH spectrum and the blue-shift of its peak. Initially, when the leading part of the fundamental pulse illuminates the sample, it

Table 6.1: **Estimated and previously measured values of the refractive index change for different nonlinear optical processes. We assumed 42 fs pulses at 815 nm and an input fluence of** 0.15 **J/cm^2,** $I_{max} \approx 29$ **TW/cm^2. For the optical Kerr effect, we list the peak change** $n_2 I_{max}$ **where** $n_2 \approx 1.7 \times 10^{-15}$ **cm^2/W [5]. The absorption coefficient due to two-photon absorption is** βI_{max}**, where** $\beta \approx 70$ **cm/TW [6]. The pulse peak intensity is the incident intensity multiplied by an intensity enhancement factor due to the stack of dielectric films. In our example** $f^2 = 10$**.**

	Δn_r@815 nm	$\alpha(\mu\text{m}^{-1})$	Δn_r@272 nm	$\alpha(\mu\text{m}^{-1})$
Kerr effect	0.05			
Two-Photon-Absorption		0.2		
Electron-plasma	-0.015	1.2	-0.0096	0.2

excites electrons from the valance band (VB) to the conduction band (CB). The presence of the electron-plasma in the CB leads to a negative change in the refractive index. This can be seen from the well-known Drude model of an electron plasma, see for example [45]:

$$(n_r + in_i)^2 = \epsilon_{core} - \frac{4\pi n_p e^2}{m}\frac{\tau^2}{1+\omega^2\tau^2} + i\frac{4\pi n_p e^2}{m}\frac{\tau}{\omega(1+\omega^2\tau^2)}, \tag{6.6}$$

where n_r, and n_i are the real and imaginary part of refractive index respectively. ϵ_{core} is the initial permitivity of the material in case of no plasma density. n_p is the plasma density, e is the electron charge, m effective mass of the electron, τ is the electron momentum relaxation time and ω is the angular frequency of incident light.

The trailing part of the pulse produces TH affected by the index change due to the plasma. This shifts the TH spectrum to shorter wavelengths, because the model shows that reduction in refractive index of a hafnia layer (the seventh layer from the air interface of design O3R) blue-shifts the TH peak. Since the leading part of the pulse is unaffected the spectrometer records a broadened TH pulse spectrum. For hafnia, the change $\Delta\epsilon_r \approx -0.05$ and $\Delta\epsilon_i \approx 0.2$ has been previously measured at incident fluences of $0.5F_{th}$ and 800 nm [39]. In right side of Eq.(6.6), we take $n_r = n_{r,core} + \Delta n_r$, and $n_i = n_{i,core} + \Delta n_i$, where $n_{r,core}$, and $n_{i,core}$ are initial real and imaginary part of refractive index, where $(n_{r,core} + in_{i,core})^2 = \epsilon_{core}$. Δn_r and Δn_i are

the change in real and imaginary part of refractive index. The change in the refractive index could be calculated as $\Delta n_r = 0.05$, and $\Delta n_i = -0.01$ at 800 nm. The best agreement of our model with observations (blue shift of 0.3 nm, spectral broadening of 1 nm and decrease in conversion efficiency by a factor of 11 was obtained for $\Delta n_r = -0.015$, $\Delta n_i = 0.075$ at 815 nm, and $\Delta n_r = -0.01$, $\Delta n_i = 0.013$ at 272 nm.

Comparing the results from Table. 6.1 and Fig. 6.14 it is obvious that only the plasma effect can explain the observed reduction in TH signal relative to what is expected from the ideal cubic conversion law. For this reason we will elucidate the plasma effect on THG in more detail.

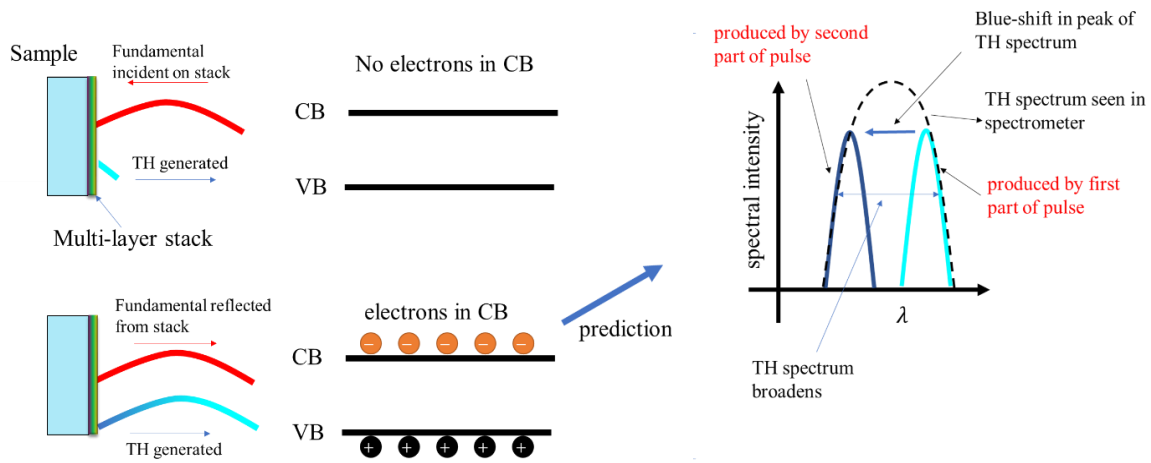

Figure 6.14: Illustration of how an electron-hole plasma can affect THG. The negative change in the refractive index leads to a shift in the FTMs resonance converting different parts of the fundamental spectrum at different times.

The negative change in the refractive index leads to a shift in the FTM's resonance converting different parts of the fundamental spectrum at different times, see Fig. 6.14. This is most pronounced if the input spectrum is broader than the FTMs bandwidth, which is the case for the unfiltered spectrum. Thus, the observed TH spectral broadening is due to the blue shift of the TH spectrum, cf. Fig. 6.12(b). The

incident fundamental pulse spectrum was about 2x larger than the FTMs conversion bandwidth. In the case, where the fundamental pulse spectrum is filtered, there is no excess fundamental spectral component to be converted to TH. Hence, a much smaller (negligible) TH blue-shift and spectral broadening is observed. The common trend for both full and filtered pulse spectrum is the drop of TH conversion efficiency with increasing fluence.

Figure. 6.15 shows the TH spectrum with and without taking into account a negative index change of $\Delta n_r = -0.015$ due to the electron-hole plasma, cf. Table. 6.1. The predicted blue shift of the TH spectrum and the drop in TH observed in the experiments are reproduced only qualitatively and overestimates the trends. Quantitative agreement would require the modeling of the time dependence of the induced changes during the pulse in detail.

The presence of the electron-plasma in the conduction band will introduce a negative change of the refractive index. The model predicts that the Hafnia layer with maximum intensity of the fundamental will have a refractive index smaller smaller than that of the other Hafnia layers. Thus, according to our model, the fundamental wavelength for peak TH conversion efficiency should happen at shorter wavelengths. This leads to the following hypothesis. If the pulse has a center wavelength longer than what the FTM is designed for, under high-fluence illumination the film stack will move closer to "resonance" with the incident pulse. To test this interpretation, we tried to excite the mirror at three different wavelengths of 803, 810, and 815 nm. Our measurements predicted that the wavelength of 810 nm is the resonance wavelength for maximum THG at low fluences. The results are shown in Fig. 6.16.

The pulse durations at 803 nm, 810 nm, and 815 nm were measured to be 61 fs, 64 fs, and 68 fs with GRENOUILLE device, respectively. Since the TH conversion scales inversely with the second power of the pulse duration, the TH signal vs fundamental pulse energy for different wavelengths should be corrected for the pulse duration for a

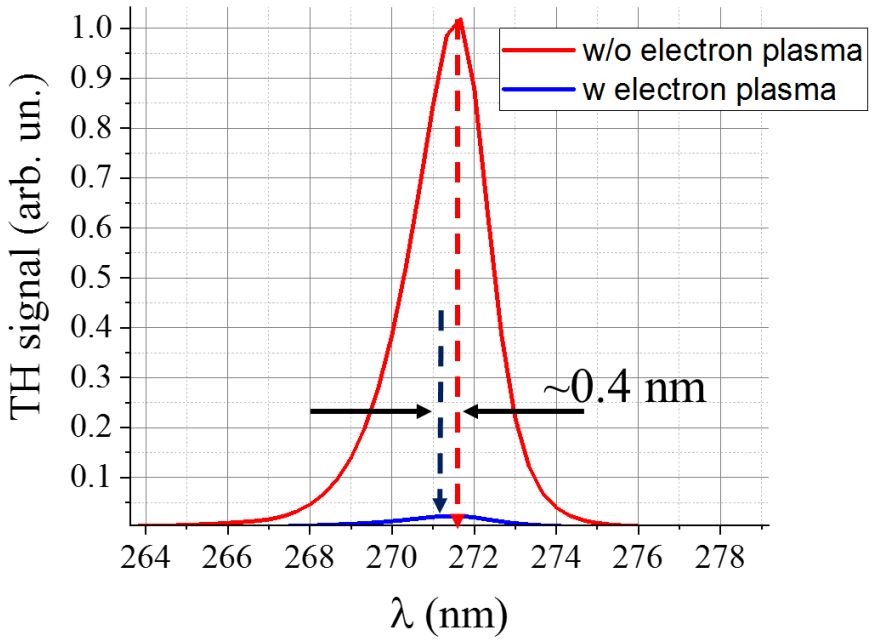

Figure 6.15: TH spectrum with and without taking into account the negative index change produced by the electron-hole plasma during the pulse using the monochromatic model. The fluence was 0.38 J/cm^2 and the index changes were taken from Table. 6.1.

better comparison. The bandwidth of the pulses was 14 nm in all cases. The results show that at the highest fluence, the pulse at 815 nm shows the same conversion efficiency as the fundamental pulses at 810 nm. This supports our hypothesis.

6.2.3 Summary

We studied the linear and nonlinear response of an when exposed to femtosecond laser pulses at fluences below and near the LIDT. Under continuous illumination of the mirror with pulse trains the third-harmonic (TH) conversion efficiency deteriorates

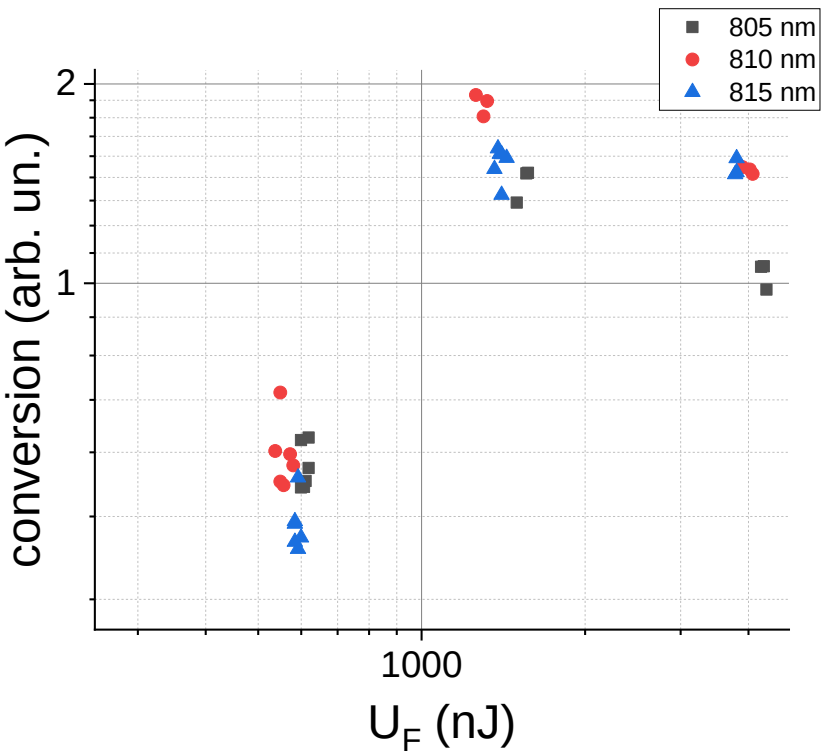

Figure 6.16: Conversion efficiency of the FTM sample O3R (with experimentally determined TH peak at 810 nm at low fluences) as a function of the fluence of the incident fundamental pulse for wavelengths of 805 nm, 810 nm, and 815 nm.

as a function of time and saturates at about 20% of the initial value for the FTM studied. The drop in TH signal vs time observed with a train of pulses (shown in Fig.1 of this chapter) is characteristic for one mirror. There were other examples where the efficiency actually even went up. Transmission and reflection measurements of the modified sample area reveal that the laser exposure changes the real part of the refractive index in the hafnia layer of the stack that sees the highest field enhancement. This was probably due to the wavelength of the incident pulse being detuned from the design wavelength. The index change in the sample leading to a smaller field enhancement and subsequently to smaller TH generation. This was tested by measuring the temperature change induced by two-photon absorption.

The observed drop agrees with model predictions. The material modification is triggered by the incident fundamental radiation, not by the generated TH. Two-photon absorption in hafnia is mediated by well-known intrinsic defects like oxygen vacancies. The long-lived material modification is likely caused by the relaxation of conduction band electrons. In addition, third-harmonic radiation produced in dielectric films is affected by a change in the material properties during a single pulse just below and above the 1-on-1 LIDT. The generation of an electron-plasma in the CB was identified as the process controlling the observed spectral shift and the broadening of the TH pulse spectra. This index change is also responsible for the deviation of the TH energy from the expected cubic dependence on the fundamental pulse energy.

Chapter 7

Summary and Outlook

The potential of stacks of dielectric films for the frequency tripling of laser radiation was investigated. Aperiodic sequences of high and low refractive index (n_H and n_L) layers, made for example from hafnia and silica that maximize the third harmonic (TH) in reflection and transmission, were designed using computer optimization. Design concepts of interest involve maximizing the TH for a given incident intensity (type A) and maximum intensity (or fluence) inside the stack (type B). Mirrors of type C maximize the conversion efficiency while keeping the intrafilm fluence below a critical value determined by laser induced damage (LID).

The FTMs were designed at UNM and selected samples were fabricated in the Laser Center Hannover (LZH, Hannover) by the group of Prof. Ristau. These mirrors were then tested and characterized at UNM.

For narrow-bandwidth incident radiation the numerically calculated third harmonic signal was found to increase rapidly with increasing number of layers N and the refractive index ratio $\Delta = n_H/n_L$, and decreased with increasing FTM bandwidth according to $1/\Delta\lambda^4$.

The numerical results were confirmed by analytical models. These models assumed that the film stack serves several purposes simultaneously. A group of layers closest to the substrate reflects TH and fundamental light. Top layers close to the air interface, depending on the mirror type, represent a mirror for the fundamental. In between these two mirrors the fundamental field is enhanced in the remaining aN layers (Fabry-Perot effect) and the high-index layers produce TH. The TH signal was found to be proportional to $N^2\Delta^{3(1-a)N/2}$.

Linear losses of TH are most critical for type-A and type-C FTMs if N less than ≈ 50, and losses for the fundamental affect the conversion most critically in type-A and type-C with N larger than ≈ 50, and type-B FTMs.

The conversion efficiencies measured with 40 fs to 60 fs pulses at wavelengths between 780 nm and 820 nm were on the order of one percent, well below the predictions. Two principal causes were identified - (i) the FTM designs do not properly take into account the full pulse bandwidth and (ii) the material changes during the illumination, leading to refractive index changes that render the mirror design less efficient. During a single pulse an electron plasma in the conduction band produces the major contribution to the index change. During a pulse train, long-lived defect states known to exist in hafnia and observed before, are responsible.

Corresponding observations were a gradual drop of the TH during continuous illumination with a pulse train until a saturation value was reached. Multi-(two-) photon absorption in hafnia produced long-lived material modifications leading to positive refractive index changes. In the case of single pulse illumination, electron-plasma formation in the conduction band introduces a negative index change in the high index layer(hafnia). The change in refractive index degrades FTM from an optimum design.

Our newly developed THG model for film stacks that took into account the full

pulse bandwidth described our measurements, in particular the dependence of THG efficiency on pulse duration, well for incident fluences below the onset of detrimental material modifications.

We developed a new design process based on this model that also takes into account LID information [46]. Corresponding mirrors with $N = 45$ suggest conversion efficiencies on the order of 7 % for pulse durations of 60 fs. A prototype mirror showed the best single pulse conversion of about 2 %. Reason for the discrepancy is the aforementioned material modification. The latter is experimentally obvious from the transition of the cubic dependence of the TH signal on the fundamental fluence to a weaker dependence.

In summary, the concept of an FTM and the developed design algorithms are valid and should be of practical interest. The film stacks tailored to enhance TH in reflection increase the conversion efficiency by more than 5 orders of magnitude compared to off-the-shelf high reflectors. Currently, the major obstacle for practical applications requiring efficiencies greater than a few percent is the material response under illumination with intense light during a single pulse and a train of pulses. Progress can be expected from current research efforts to improve the quality of dielectric coatings needed for PetaWatt lasers and the development of stacks of crystalline films. The latter could provide larger values of $\chi^{(3)}$ reducing the required intrafilm intensities and associated detrimental processes. Alternatively, more detailed knowledge of the material modifications could lead to FTM designs where the corresponding changes of the refractive index are already taken into account.

Appendix A

Wave Equation of THG

Here we present the derivation of Eq. (2.8) that governs the evolution of the TH field in the positive z direction.

Inserting Eq. (2.5) and Eq. (2.6) into Eq. (2.4) and using $P_{NL} = \epsilon_0 \chi^{(3)} E_F^3$ yields:

$$\frac{\partial^2}{\partial z^2}(B_r(z)e^{i(3\omega t-\kappa z)}) - \frac{n^2}{c^2}\frac{\partial^2}{\partial t^2}(B_r(z)e^{i(3\omega t-\kappa z)}) = \frac{\chi^{(3)}}{c^2}\frac{\partial^2}{\partial t^2}(Ae^{i(\omega t-kz)}). \tag{A.1}$$

After differentiation of each term and dividing by $e^{i\omega t}$ we obtain

$$e^{-i\kappa z}\frac{\partial^2 B_r}{\partial z^2} - 2i\kappa e^{-i\kappa z}\frac{\partial B_r}{\partial z} - \kappa^2 e^{-i\kappa z}B_r + \frac{n^2(3\omega)^2}{c^2}e^{-i\kappa z}B_r = -\frac{9\omega^2\chi^{(3)}}{c^2}A^3 e^{-3ikz}. \tag{A.2}$$

Since $\kappa = \frac{3n\omega}{c}$ the terms three and four in left hand side cancel each other. Division by $e^{-i\kappa z}$ produces

$$\frac{\partial^2 B_r}{\partial z^2} - 2i\kappa\frac{\partial B_r}{\partial z} = -\frac{9\omega^2\chi^{(3)}}{c^2}A^3 e^{-i\Delta k_- z}, \tag{A.3}$$

where $\Delta k_- = 3kz - \kappa$. Using the slowly varying envelope approximation $\left|\frac{\partial^2 B_r(z)}{\partial z^2}\right| << 2\kappa\left|\frac{\partial B_r(z)}{\partial z}\right|$, we can neglect the first term in Eq. (A.3) and obtain:

$$\frac{\partial B_r(z)}{\partial z} = -\frac{9i\omega^2\chi^{(3)}}{2\kappa c^2}A^3 e^{-i\Delta k_- z}. \tag{A.4}$$

The same procedure can be used to derive Eq. (2.9).

Appendix B

The Optical Parameters of Different Materials

Relevant material parameters of the thin-film coatings used in the thesis are summarized here. The refractive index and $\chi^{(3)}$ at the fundamental wavelength of 800 nm and the TH wavelength of 267 nm are shown in Table B.1 [4]. The damage

Table B.1: **Complex refractive index n, third-order susceptibility $\chi^{(3)}$ and coherence length of selected film materials. The $\chi^{(3)}$ values are from [4], where $\gamma = 2 \times 10^{-22} m^2/V^2$ is $\chi^{(3)}$ of fused silica.**

material	n (@800nm)	n (@267nm)	L_{coh} (nm)	$\chi^{(3)}$
HfO_2 (film)	1.9547	2.1488	676	20.3γ
	$-0.0004i$	$-0.0058i$		
SiO_2 (film)	1.4755	1.5342	2234	γ
Al	2.6052	0.219	55	8γ
	$-8.527i$	$-3.16i$		
Suprasil	1.4542	1.5015	2768	γ
Al_2O_3 (film)	1.6530	1.7516	1451	8.2γ
Ta_2O_5 (film)	2.0621	2.7272	195	35γ
	$-0.1575i$	$-0.0058i$		

thresholds of selected materials are shown in Table B.2 [1]. The critical fluence F_{crit}

inside the film can be calculated using the field intensity enhancement factor f and the incident fluence F_{inc} at the damage threshold using the relation $F_{crit} = f^2 F_{inc}$. Note that the f^2 depends on the FTM architecture. Here we list the LIDTs for single films of thickness D.

Table B.2: **The incident fluence F leading to damage in films with thickness D, bandgap of E_g, and refractive index of n_0 at 800 nm for a pulse duration of 50 fs from [1].**

material	n_0	D (nm)	E_g (eV)	F (mJ/cm^2)	f^2
HfO_2 (film)	2.09	568	5.1	700	0.66
SiO_2 (film)	1.50	790	8.3	1470	0.66
Al_2O_3 (film)	1.65	716	6.5	1040	0.66
Ta_2O_5 (film)	2.17	546	3.8	390	0.66

Appendix C

The Structure of Designs

Table C.1 summarizes important paramters of FTMs used in the thesis. We assumed

Table C.1: **Design names, number of layers N, fundamental wavelength λ, and complex refractive index n of the high and low index materials used. Note, n_{Sub} is the refractive index of the substrate Suprasil.**

Design	N	λ (nm)	n_{HfO_2} @λ	n_{HfO_2} @$\lambda/3$	n_{SiO_2} @λ	n_{SiO_2} @$\lambda/3$	n_{Sub} @λ	n_{Sub} @$\lambda/3$
SL	1	787	$1.9547 - 0.0004i$	$2.1481 - 0.0058i$	1.4755	1.5340	1.4542	1.5014
OS	25	787	$1.9547 - 0.0004i$	$2.1481 - 0.0058i$	1.4755	1.5340	1.4542	1.5014
A27	27	787	$1.9547 - 0.0004i$	$2.1481 - 0.0058i$	1.4755	1.5340	1.4542	1.5014
L1R	25	787	1.9107	$2.1305 - 0.0047i$	1.4719	1.5286	1.4542	1.5014
N1R	37	787	1.9107	$2.1305 - 0.0047i$	1.4719	1.5286	1.4542	1.5014
S1	33	787	$1.9409 - 0.0001i$	$2.1652 - 0.0046i$	1.4751	1.5220	1.4542	1.5014
S2	45	787	1.9141	$2.1249 - 0.0041i$	1.4765	1.5325	1.4542	1.5014
S3	45	815	1.9129	$2.1018 - 0.0034i$	1.4760	1.5265	1.4536	1.5
O3R	25	815	$1.9122 - 0.0001i$	$2.1039 - 0.0030i$	1.4548	1.5070	1.4428	1.4960

that the $\chi^{(3)}$ of materials does not vary between different coating runs. This assumption is based on measurements of $\chi^{(3)}$ of HfO_2 from two different coatings of a single layer hafnia with the same thickness that produced the same TH signal within the measurement errors.

The order and thickness (in nm) of films in the designs are as follows.

1. Design SL

air/x[HfO_2]/Sub

x = [377]

2. Design OS

air/x[$HfO_2(SiO_2HfO_2)^{12}$]/Sub

x=[47.2 207 40.5 176.4 114.6 93.1 213.7 195.8 63.6 73.9 138.6 153 90.3 127.7 87.5 141.5 87.2 134 91.9 140.3 88.8 134.2 91.9 141 320.6]

3. Design A27

air/x[$HfO_2(SiO_2HfO_2)^{13}$]/Sub

x=[98.1 130.1 97.9 132.5 95.9 137.2 102.6 138.5 102.8 134.3 399.5 98.6 142.6 394.2 92.0 133.5 96.1 131.0 98.4 135.9 110.5 143.5 103.1 132.1 96.8 128.9 99.5]

4. Design L1R

air/x[$HfO_2(SiO_2HfO_2)^{12}$]/Sub

x=[53 187.8 50.6 177.4 110.4 103.1 229.3 185.6 60.6 73 138.3 147.1 88.3 136.5 91.3 143.8 88 134.7 92.9 137 327.8 134.9 90.7 142.4 326.9]

5. Design N1R

air/x[$HfO_2(SiO_2HfO_2)^{18}$]/Sub

x=[105.2 143.4 114.5 135.8 97.8 135.2 98 133.9 88.7 139.9 106.9 138.7 105.3 133.8 230.1 345.5 141.5 61.5 143.7 140.1 83.7 400.8 99.1 383.9 101.4 132.7 98.4 136 113.3 146.5 99.5 133.1 99.1 126.1 100.3 133.6 319]

6. Design S1

air/x[$HfO_2(SiO_2HfO_2)^{16}$]/Sub

x=[125 130.2 94 118.5 42.7 183.3 42.4 183.6 49.4 184.1 45.9 183.1 47 186.2 46.2 184.8 43.4 186.9 43.6 193.1 40.8 125.3 93 131.6 98.6 185.4 95.6 131.4 93.4 132 95 132 95]

7. Design S2

air/x[$HfO_2(SiO_2HfO_2)^{22}$]/Sub

x=[131.9 129 91.6 106.3 46.1 179.3 47.1 172.3 55.2 176.1 53.5 180.9 55.1 175.4 52.7 183.3 53.1 177.7 53.6 182.7 42.2 192.1 47.6 179.9 46.8 189.3 39.4 129.9 91.7 136.1 100.3 190 97.7 131.1 93.4 138.8 93.9 129.1 93.6 133.8 98.4 139.6 91.9 137.6 98.3]

8. Design S3

air/x[$HfO_2(SiO_2HfO_2)^{22}$]/Sub

x=[133.8 132.2 92.3 110.6 47.1 186.0 48.3 179.1 57.6 183.1 53.9 187.0 56.8 181.7 55.8 189.6 54.7 183.1 55.2 190.4 49.3 199.2 49.5 186.5 47.5 195.9 39.5 133.5 87.0 140.4 103.7 197.0 101.0 135.6 96.5 142.5 97.0 133.6 96.8 137.9 99.7 144.4 95.1 142.5 101.8]

9. Design O3R

air/x[$HfO_2(SiO_2HfO_2)^{12}$]/Sub

x=[51.2 211 47.9 181.4 117.6 105.1 224 199.8 68.8 83.9 144.6 162 93.5 136.7 95.2 147.5 94.6 326.2 164.8 146.4 90.8 138.7 98.9 151.7 329.6]

Appendix D

Fourier Transform and Parseval Theorem

Here we summarize the Fourier transform conventions that are used in the entire work, see also [29]. The Fourier Transform of a function in the time domain $f(t)$ is defined as:

$$F(\Omega) = \mathcal{F}\{f(t)\} = \int_{-\infty}^{+\infty} dt f(t) e^{-i\Omega t}. \tag{D.1}$$

Then, the inverse Fourier Transform will be:

$$f(t) = \mathcal{F}^{-1}\{F(\Omega)\} = \frac{1}{2\pi} \int_{-\infty}^{+\infty} d\Omega F(\Omega) e^{+i\Omega t}. \tag{D.2}$$

The convolution theorem states that

$$\mathcal{F}\{\int_{-\infty}^{+\infty} d\tau f(t-\tau) f(\tau)\} = F^2(\Omega). \tag{D.3}$$

The Fourier Transforms of $f^2(t)$ and $f^3(t)$ using the convolution theorem are:

$$\mathcal{F}\{f^2(t)\} = \frac{1}{2\pi} \int_{-\infty}^{+\infty} d\Omega' F(\Omega - \Omega') F(\Omega') \tag{D.4}$$

and

$$\mathcal{F}\{f^2(t)\} = \frac{1}{(2\pi)^2}\int_{-\infty}^{+\infty} d\Omega' F(\Omega-\Omega')\int_{-\infty}^{+\infty} d\Omega'' F(\Omega'-\Omega'')F(\Omega''). \tag{D.5}$$

Finally, Parseval theorem states

$$\int_{-\infty}^{+\infty} dt\,|f(t)|^2 = \frac{1}{2\pi}\int_{-\infty}^{+\infty} d\Omega\,|F(\Omega)|^2\,. \tag{D.6}$$

Appendix E

Theory of Third Harmonic Generation in a Frequency Tripling Mirror

Here we summarize the derivation and relations corresponding to THG in reflection using an FTM. We follow the procedure outlined in paper [30].

Figure. E.1 shows an overview of an FTM. The fundamental and TH fields are labeled with E_F and E. The fields at the right and the left interfaces are labeled with and without a hyphen, respectively. The first and second subscripts of fields show the number of medium and field propagation direction. We define a vector for fundamental fields at each interface as $\vec{v}_i = (E_{F,i,r}, E_{F,i,l})$. Using a matrix formalism, the fields at each interface can be calculated using the relation.

$$\vec{v}_i = \begin{pmatrix} E_{F,i,r} \\ E_{F,i,l} \end{pmatrix} = \mathcal{H}_{i,i-1}\mathcal{L}_{i-1}...\mathcal{H}_{2,1}\mathcal{L}_1\mathcal{H}_{1,0} \begin{pmatrix} E'_{F,0,r} \\ E'_{F,0,l} \end{pmatrix} \tag{E.1}$$

where $\mathcal{H}_{i,j}$ and $\mathcal{L}_i$ are the transfer matrix from layer i to j and propagation matrix

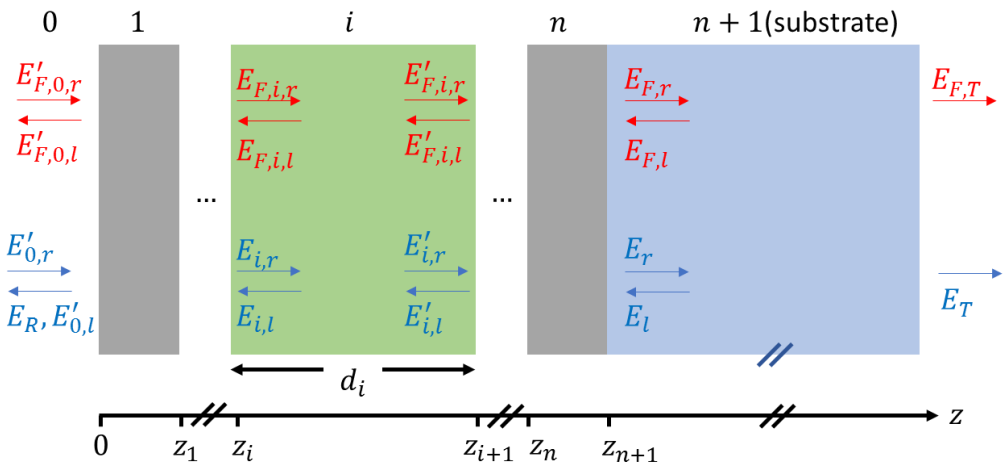

Figure E.1: THG in a stack of layers on a substrate. TH and fundamental fields are labeled E and E_F, respectively. Fields propagating to the right (r) and left (l) are distinguished in each layer. Fields on the right interfaces are labeled with a prime.

in layer i, respectively. These matrices are:

$$\mathcal{H}_{i,j} = \frac{1}{t_{ij}} \begin{pmatrix} 1 & r_{ij} \\ r_{ij} & 1 \end{pmatrix} \tag{E.2}$$

and

$$\mathcal{L}_i = \begin{pmatrix} e^{-ik_i d_i} & 0 \\ 0 & e^{+ik_i d_i} \end{pmatrix}, \tag{E.3}$$

where, r_{ij},t_{ij},k_i, and d_i are the reflection and transmission coefficient of the fundamental field from layer i to j, the wavenumber and the thickness of layer i, respectively.

The overall transfer matrix $\mathcal{M}$ is

$$\mathcal{M} = \mathcal{H}_{n+1,n}\mathcal{L}_n ... \mathcal{H}_{2,1}\mathcal{L}_1\mathcal{H}_{1,0}, \tag{E.4}$$

which relates the fields in the substrate to the incident fields as:

$$\vec{v}_{n+1} = \begin{pmatrix} E_{F,r} \\ E_{F,l} \end{pmatrix} = \begin{pmatrix} \mathcal{M}_{11} & \mathcal{M}_{12} \\ \mathcal{M}_{21} & \mathcal{M}_{22} \end{pmatrix} \begin{pmatrix} E'_{F,0,r} \\ E'_{F,0,l} \end{pmatrix}. \tag{E.5}$$

Here, $\mathcal{M}_{ij}$ are the elements of the transfer matrix $\mathcal{M}$. If we ignore the reflection at the back surface of the substrate, then:

$$E'_{F,0,l} = -\frac{\mathcal{M}_{21}}{\mathcal{M}_{22}} E'_{F,0,r}. \tag{E.6}$$

This relation determines the left field component in the vector $\vec{v}_0$.

So far we have dealt only with the fundamental field components. In the next step, we will calculate the TH fields at each interface. First, we define a TH field vector for the input $\vec{w}'_0 = (E'_{0,r}, E'_{0,l})$, and in substrate $\vec{w}_{n+1} = (E_r, E_l)$. The overall transfer matrix M is

$$M = H_{n+1,n} L_n ... H_{2,1} L_1 H_{1,0}, \tag{E.7}$$

where $H_{i,j}$ and L_i are the transfer matrix from layer i to j and propagation matrix in layer i, respectively. They are:

$$H_{i,j} = \frac{1}{\tau_{ij}} \begin{pmatrix} 1 & \rho_{ij} \\ \rho_{ij} & 1 \end{pmatrix} \tag{E.8}$$

and

$$L_i = \begin{pmatrix} e^{-i\kappa_i d_i} & 0 \\ 0 & e^{+i\kappa_i d_i} \end{pmatrix}, \tag{E.9}$$

where, ρ_{ij},τ_{ij}, and κ_i are reflection, transmission coefficient of TH field from layer i to j and the wavenumber in layer i, respectively.

Assuming TH generation in layer i under negligible pump depletion (small signal conversion), the TH field at the right boundary is

$$E'_{i,r} = E_{i,r} e^{-i\kappa_i d_i} + \Delta E_{i,r}. \tag{E.10}$$

$\Delta E_{i,r}$ is the TH field component propagating to the right that is generated in layer i. Similarly we find the left propagating TH field component $\Delta E_{i,l}$. Solving the

Maxwell wave equation in the layer i [30], resulting TH field would be:

$$\Delta E_{i,r} = -\frac{9i\omega^2\chi_i^{(3)}d_i e^{-i\kappa_i d_i}}{2\kappa_i c^2}$$
$$\{E_{F,i,r}^3 e^{-i\frac{\Delta k_i^- d_i}{2}}\,\mathrm{sinc}\left(\frac{\Delta k_i^- d_i}{2}\right) + E_{F,i,l}^3 e^{+i\frac{\Delta k_i^+ d_i}{2}}\,\mathrm{sinc}\left(\frac{\Delta k_i^+ d_i}{2}\right)$$
$$+ 3E_{F,i,r}^2 E_{F,i,l} e^{-i\frac{\Delta\phi_i^- d_i}{2}}\,\mathrm{sinc}\left(\frac{\Delta\phi_i^- d_i}{2}\right) + 3E_{F,i,r}E_{F,i,l}^2 e^{+i\frac{\Delta\phi_i^+ d_i}{2}}\,\mathrm{sinc}\left(\frac{\Delta\phi_i^+ d_i}{2}\right)\} \tag{E.11}$$

and

$$\Delta E_{i,l} = -\frac{9i\omega^2\chi_i^{(3)}d_i}{2\kappa_i c^2}\{E_{F,i,r}^3 e^{-i\frac{\Delta k_i^+ d_i}{2}}\,\mathrm{sinc}\left(\Delta k_i^+ d_i 2\right)$$
$$+ E_{F,i,l}^3 e^{+i\frac{\Delta k_i^- d_i}{2}}\,\mathrm{sinc}\left(\frac{\Delta k_i^- d_i}{2}\right)$$
$$+ 3E_{F,i,r}^2 E_{F,i,l} e^{-i\frac{\Delta\phi_i^+ d_i}{2}}\,\mathrm{sinc}\left(\frac{\Delta\phi_i^+ d_i}{2}\right) + 3E_{F,i,r}E_{F,i,l}^2 e^{+i\frac{\Delta\phi_i^- d_i}{2}}\,\mathrm{sinc}\left(\frac{\Delta\phi_i^- d_i}{2}\right)\}. \tag{E.12}$$

Here, $\Delta k_i^{\mp} = ik_i \mp \kappa_i$ and $\Delta\phi_i^{\mp} = k_i \mp \kappa_i$. Next we define the vector $\vec{\Delta}_i = (\Delta E_{i,r}, -\Delta E_{i,l}e^{i\kappa_i d_i})$ that shows the TH fields that are generated at the right interface of the layer i. The total TH field at the right will be the sum of TH fields propagating to the right plus the TH fields from the other layers

$$\begin{pmatrix} E'_{i,r} \\ E'_{i,l} \end{pmatrix} = L_i \begin{pmatrix} E_{i,r} \\ E_{i,l} \end{pmatrix} + \vec{\Delta}_i \tag{E.13}$$

. Next we propagate the TH fields to the output interface, TH vector at $\vec{w}_{n+1}$ will be.

$$\vec{w}_{n+1} = H_{n+1,n}L_n H_{n,n-1}...L_1 H_{1,0}\vec{w}'_0 + H_{n+1,n}L_n H_{n,n-1}...L_2 H_{2,1}\vec{\Delta}_1$$
$$+ H_{n+1,n}L_n H_{n,n-1}...L_3 H_{3,2}\vec{\Delta}_2 + ... + H_{n+1,n}\vec{\Delta}_n \tag{E.14}$$

After rearranging the above Eq.(E.14), $E'_{0,l}$ and E_r can be written as

$$\begin{pmatrix} E_r \\ E'_{0,l} \end{pmatrix} = \frac{1}{M_{11}^{-1}} \begin{pmatrix} 1 & 0 \\ M_{21}^{-1} & -M_{11}^{-1} \end{pmatrix}$$
$$H_{0,1}L_1^{-1}[\vec{\Delta}_1 + H_{1,2}L_2^{-1}\vec{\Delta}_2 + ... + H_{1,2}L_2^{-1}...H_{n-1,n}L_n^{-1}\vec{\Delta}_n]$$
$$+ \frac{1}{M_{11}^{-1}} \begin{pmatrix} 1 & -M_{12}^{-1} \\ M_{21}^{-1} & M_{11}^{-1}M_{22}^{-1} - M_{12}^{-1}M_{21}^{-1} \end{pmatrix} \begin{pmatrix} E'_{0,r} \\ E_l \end{pmatrix}, \quad \text{(E.15)}$$

where the terms M_{ij} are the elements of matrix M^{-1}, and L_i^{-1} is the inverse of propagation matrix for layer i. Assuming no incident TH field, $E'_{0,r} = 0$, and $E_l = 0$.

Appendix F

The Reflectance and Transmittance of End Mirrors of an FTM

We want to investigate the reflection from the group of top and bottom layers of a design-A FTM (design A27 with $N = 27$ layers for fundamental wavelength $\lambda = 787$ nm, see appendix B). These two stacks can be considered as two mirrors (M_S and M_A). Figures F.1(b) and F.2(b) show these mirrors (parts that are not grey) M_A and M_S next to air and substrate.

The reflection spectrum Fig. F.1(a) from M_A is close to that of a QW structure at the fundamental wavelength λ. However at the TH wavelength $\lambda/3$ the reflection of an ideal QW stack is smaller.

The reflection spectrum Fig. F.2(a) from M_S is close to that of a QW structure at the fundamental wavelength λ. However at the TH wavelength $\lambda/3$ M_S is highly reflective unlike an ideal QW.

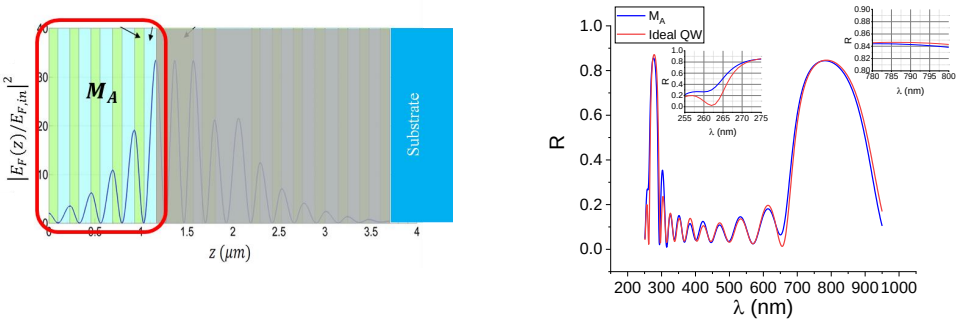

(a) (b)

Figure F.1: (a) Multilayer stack M_A (green is hafnia, and blue is silica) next to air interface. (b) The reflection spectrum of mirror M_A, and an ideal QW with same number of layers and order.

The high reflection of both end mirrors at fundamental, and high reflection of mirror next to substrate at TH wavelength is expected. Because our computer search is looking for designs that maximize TH in reflection. While we have shown this for an optimum type A design A27, in general this is true for type A and C designs, and also applies to end mirrors on top of the substrate in case of type B designs.

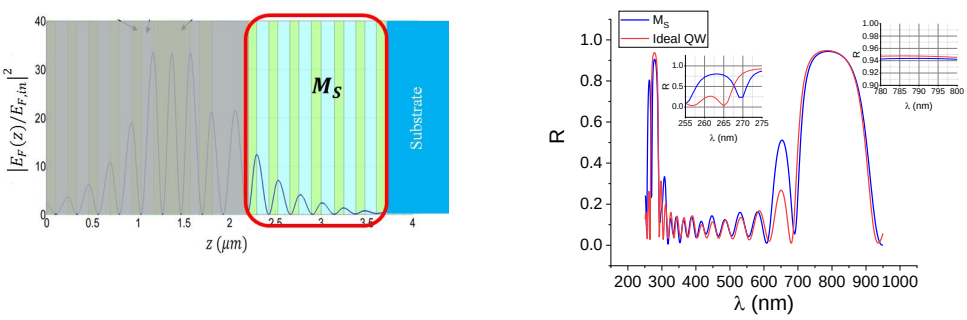

(a) (b)

Figure F.2: (a) Multilayer stack M_S (green is hafnia, and blue is silica)on top of substrate. (b) The reflection spectrum of mirror M_S, and an ideal QW with same number of layers and order.

Appendix G

THG from an FTM on Top of a Perfect Reflector

In this Appendix, we show an analytical proof that the TH fields from individual layers of stack of dielectric films on top of a perfect reflector (ideal metal), will have phase difference of integer multiple of $\pm\pi$ at the output of the mirror.

G.1 Transmission Matrix of a Perfect reflector

We assume light is normally incident from a lossless medium 1 with a refractive index of n_1 onto medium 2 with a refractive index of $n_2 - ik_2$. The reflectance R using the Fresnel relation at normal incidence is

$$R = \frac{(n_2 - n_1)^2 + k_2^2}{(n_2 - n_1)^2 + k_2^2} \tag{G.1}$$

A perfect reflector (medium 2) is defined in case that reflectance from of light incident from medium 1 on medium 2 is $R = 1$, and transmittance $T = 0$. Setting

Eq.(G.1) to 1, entails that the real part of the refractive index of medium 2 to be $n_2 \ll n_1$, or its imaginary part of refractive index $k_2 \gg n_2, n_1$.

Knowing the transmission and reflection field amplitudes at normal incidence are:

$$t_{21} = \frac{2n_1}{n_1 + n_2 - ik_2} \tag{G.2}$$

$$r_{21} = \frac{n_1 - n_2 + ik_2}{n_1 + n_2 - ik_2} \tag{G.3}$$

if we apply the condition of perfect reflector they turn into:

$$t_{21} \approx -\frac{2n_1}{ik_2} \tag{G.4}$$

$$r_{21} \approx -1 \tag{G.5}$$

Therefore, transmission matrix of the perfect reflector from medium 2 to 1 will look like

$$H_{21} = -\frac{ik_2}{2n_1}\begin{pmatrix} 1 & -1 \\ -1 & 1 \end{pmatrix} \tag{G.6}$$

which will use symbol H for TH wavelength, and $\mathcal{H}$ for fundamental.

G.2 Phase relation of for/backward propagating fundamental fields

In this section, it will be shown that there is a constant phase relationship between forward and backward propagating fundamental fields inside each layer of a stack on top of a perfect reflector. The perfect reflector is labelled with index $n+1$. The forward and backward propagating fields in perfect reflector $n+1$ are related to incident field with relation (G.7).

$$\begin{pmatrix} E_{F,r} \\ E_{F,l} \end{pmatrix} = \mathcal{H}_{n+1,n}\mathcal{L}_n ... \mathcal{H}_{2,1}\mathcal{L}_1\mathcal{H}_{1,0}\begin{pmatrix} E'_{F,0,r} \\ E'_{F,0,l} \end{pmatrix} \tag{G.7}$$

Since there are no propagating fields inside a perfect reflector $E_{F,r} = E_{F,l} = 0$. The transmission matrix $\mathcal{H}_{n+1,n}$ is:

$$\mathcal{H}_{n+1,n} = -\frac{ik_{n+1,F}}{2n_{n,F}} \begin{pmatrix} 1 & -1 \\ -1 & 1 \end{pmatrix} \tag{G.8}$$

where, where $k_{n+1,F}$, and $n_{n,F}$ are imaginary and real part of refractive indices at fundamental wavelength in layers $n+1$, and n. In addition, the matrix form of product of transmission and propagation matrices posses a symmetric property as follow:

$$\mathcal{L}_n ... \mathcal{H}_{2,1} \mathcal{L}_1 \mathcal{H}_{1,0} = \begin{pmatrix} a & b \\ b^* & a^* \end{pmatrix} \tag{G.9}$$

We plug in the relations (G.8) and (G.9) into relation (G.7), and after simplification, it yields

$$E'_{F,0,l} = \frac{b^* - a}{b - a^*} E'_{F,0,r} \tag{G.10}$$

In general for any layer i, the forward and backward propagating fields at interface are related to incident field as follow:

$$\begin{pmatrix} E_{F,i,r} \\ E_{F,i,l} \end{pmatrix} = \mathcal{H}_{i,i-1} \mathcal{L}_{i-1} ... \mathcal{H}_{2,1} \mathcal{L}_1 \mathcal{H}_{1,0} \begin{pmatrix} E'_{F,0,r} \\ E'_{F,0,l} \end{pmatrix} \tag{G.11}$$

where using the relation (G.10), it can be rewritten as:

$$\begin{pmatrix} E_{F,i,r} \\ E_{F,i,l} \end{pmatrix} = \begin{pmatrix} a_i & b_i \\ b_i^* & a_i^* \end{pmatrix} \begin{pmatrix} 1 \\ \frac{b^* - a}{b - a^*} \end{pmatrix} E'_{F,0,r} \tag{G.12}$$

using equation (G.12), there is a relation between $F_{i,r}$ and $E^*_{F,i,l}$.

$$\frac{E_{F,i,r}}{E^*_{F,i,l}} = \frac{b^* - a}{b - a^*} \frac{E'_{F,0,r}}{E'^*_{F,0,r}} \tag{G.13}$$

It shows the relation $E_{F,i,r} = e^{i\phi} E^*_{F,i,l}$, where ϕ is a phase that depends on the phase of incident fundamental field and transmission matrix of whole stack.

G.3 In Phase TH Fields at Output Interface

In this section, it will be proven analytically that TH fields generated in each layer inside the dielectric stack(negligible absorption) on top of a perfect reflector superpose constructively or destructively at the output interface. In other word, TH fields due to each layer have relative phase of integer multiples of π. We start with equation (E.15), and insert the identity matrix in the form $I = M^{-1}M$ in that relation, where M is from relation (E.4). After simplification it yields:

$$\begin{pmatrix} E_r \\ E'_{0,l} \end{pmatrix} = \begin{pmatrix} M_{22} & -M_{12} \\ 0 & 1/M_{22} \end{pmatrix} [H_{n+1,n}L_n...L_2H_{2,1}\vec{\Delta}_1 + H_{n+1,n}L_n...L_3H_{3,2}\vec{\Delta}_2 + ... + H_{n+1,n}\vec{\Delta}_n] \quad \text{(G.14)}$$

factoring out transmission matrix of perfect reflector $H_{n+1,n}$,

$$\begin{pmatrix} E_r \\ E'_{0,l} \end{pmatrix} = \begin{pmatrix} M_{22} & -M_{12} \\ 0 & 1/M_{22} \end{pmatrix} H_{n+1,n}[L_n...L_2H_{2,1}\vec{\Delta}_1 + L_n...L_3H_{3,2}\vec{\Delta}_2 + ... + \vec{\Delta}_n] \quad \text{(G.15)}$$

every term inside the bracket is a vector that can be written with

$$\vec{v_i} = \begin{pmatrix} v_{1,i} \\ v_{2,i} \end{pmatrix} = L_n...L_{i+2}H_{i+2,i+1}L_{i+1}H_{i+1,i}\vec{\Delta_i} \quad \text{(G.16)}$$

, and plugging in the value of matrix $H_{n+1,n}$, then

$$\begin{aligned}
&\begin{pmatrix} E_r \\ E'_{0,l} \end{pmatrix} = - \begin{pmatrix} M_{22} & -M_{12} \\ 0 & 1/M_{22} \end{pmatrix} \frac{ik_{n+1}}{2n_n} \begin{pmatrix} 1 & -1 \\ -1 & 1 \end{pmatrix} \\
&\left[\begin{pmatrix} v_{1,1} \\ v_{2,1} \end{pmatrix} + \begin{pmatrix} v_{1,2} \\ v_{2,2} \end{pmatrix} + ... + \begin{pmatrix} v_{1,n} \\ v_{2,n} \end{pmatrix} \right] \\
&= - \begin{pmatrix} M_{22} & -M_{12} \\ 0 & 1/M_{22} \end{pmatrix} \frac{ik_{n+1}}{2n_n} \\
&\left[\begin{pmatrix} v_{1,1} - v_{2,1} \\ -v_{1,1} + v_{2,1} \end{pmatrix} + \begin{pmatrix} v_{1,2} - v_{2,2} \\ -v_{1,2} + v_{2,2} \end{pmatrix} + ... + \begin{pmatrix} v_{1,n} - v_{2,n} \\ -v_{1,n} + v_{2,n} \end{pmatrix} \right] \\
&= - \begin{pmatrix} M_{22} & -M_{12} \\ 0 & 1/M_{22} \end{pmatrix} \frac{ik_{n+1}}{2n_n} \\
&[(v_{1,1} - v_{2,1}) + (v_{1,2} - v_{2,2}) + ... + (v_{1,n} - v_{2,n})] \begin{pmatrix} 1 \\ -1 \end{pmatrix} \\
&\qquad = -\frac{ik_{n+1}}{2n_n} [(v_{1,1} - v_{2,1}) + (v_{1,2} - v_{2,2}) + ... + (v_{1,n} - v_{2,n})] \begin{pmatrix} M_{22} + M_{12} \\ -1/M_{22} \end{pmatrix}
\end{aligned} \tag{G.17}$$

where, where k_{n+1}, and n_n are imaginary and real part of refractive indices at TH wavelength in layers $n+1$, and n. After rearranging it in the form shown below:

$$\begin{aligned}
&\begin{pmatrix} E_r \\ E'_{0,l} \end{pmatrix} = -\frac{ik_{n+1}}{2n_n}(v_{1,1} - v_{2,1}) \\
&\left[1 + \frac{v_{1,2} - v_{2,2}}{v_{1,1} - v_{2,1}} \left[1 + ... + \frac{v_{1,n-1} - v_{2,n-1}}{v_{1,n-2} - v_{2,n-2}} \left[1 + \frac{v_{1,n} - v_{2,n}}{v_{1,n-1} - v_{2,n-1}} \right] \right] ... \right] \\
&\qquad\qquad\qquad\qquad\qquad\qquad \begin{pmatrix} M_{22} + M_{12} \\ -1/M_{22} \end{pmatrix}
\end{aligned} \tag{G.18}$$

From here on, we will show that all terms inside brackets are real numbers. In other word the phase difference between those terms is zero. To show that, we

calculate $\vec{v}$ vector for two consecutive layers, so we will have

$$\begin{pmatrix} v_{1,i} \\ v_{2,i} \end{pmatrix} = \begin{pmatrix} P_{11}^{(i+1)} & P_{12}^{(i+1)} \\ P_{21}^{(i+1)} & P_{22}^{(i+1)} \end{pmatrix} L_{i+1} H_{i+1} \vec{\Delta}_i \tag{G.19}$$

$$\begin{pmatrix} v_{1,i+1} \\ v_{2,i+1} \end{pmatrix} = \begin{pmatrix} P_{11}^{(i+1)} & P_{12}^{(i+1)} \\ P_{21}^{(i+1)} & P_{22}^{(i+1)} \end{pmatrix} \vec{\Delta}_{i+1} \tag{G.20}$$

after inserting the matrix values, and simplification, it yields:

$$\begin{aligned}
&\begin{pmatrix} v_{1,i} \\ v_{2,i} \end{pmatrix} \\
&= \begin{pmatrix} P_{11}^{(i+1)} & P_{12}^{(i+1)} \\ P_{21}^{(i+1)} & P_{22}^{(i+1)} \end{pmatrix} \begin{pmatrix} e^{-i\kappa_{i+1}d_{i+1}} & 0 \\ 0 & e^{i\kappa_{i+1}d_{i+1}} \end{pmatrix} \frac{1}{\tau_{i+1,i}} \begin{pmatrix} 1 & \rho_{i+1,i} \\ \rho_{i+1,i} & 1 \end{pmatrix} \begin{pmatrix} \Delta_{i,r} \\ \Delta_{i,l} \end{pmatrix} \\
&= \frac{1}{\tau_{i+1,i}} \begin{pmatrix} P_{11}^{(i+1)} & P_{12}^{(i+1)} \\ P_{21}^{(i+1)} & P_{22}^{(i+1)} \end{pmatrix} \begin{pmatrix} e^{-i\kappa_{i+1}d_{i+1}}\Delta_{i,r} + \rho_{i+1,i}e^{-i\kappa_{i+1}d_{i+1}}\Delta_{i,l} \\ \rho_{i+1,i}e^{i\kappa_{i+1}d_{i+1}}\Delta_{i,r} + e^{i\kappa_{i+1}d_{i+1}}\Delta_{i,l} \end{pmatrix} \\
&= \frac{1}{\tau_{i+1,i}} \\
&\begin{pmatrix} P_{11}^{(i+1)}(e^{-i\kappa_{i+1}d_{i+1}}\Delta_{i,r} + \rho_{i+1,i}e^{-i\kappa_{i+1}d_{i+1}}\Delta_{i,l}) + P_{12}^{(i+1)}(\rho_{i+1,i}e^{i\kappa_{i+1}d_{i+1}}\Delta_{i,r} + e^{i\kappa_{i+1}d_{i+1}}\Delta_{i,l}) \\ P_{21}^{(i+1)}(e^{-i\kappa_{i+1}d_{i+1}}\Delta_{i,r} + \rho_{i+1,i}e^{-i\kappa_{i+1}d_{i+1}}\Delta_{i,l}) + P_{22}^{(i+1)}(\rho_{i+1,i}e^{i\kappa_{i+1}d_{i+1}}\Delta_{i,r} + e^{i\kappa_{i+1}d_{i+1}}\Delta_{i,l}) \end{pmatrix}
\end{aligned} \tag{G.21}$$

and for other relation

$$\begin{aligned}
\begin{pmatrix} v_{1,i+1} \\ v_{2,i+1} \end{pmatrix} &= \begin{pmatrix} P_{11}^{(i+1)} & P_{12}^{(i+1)} \\ P_{21}^{(i+1)} & P_{22}^{(i+1)} \end{pmatrix} \vec{\Delta}_{i+1} \\
&= \begin{pmatrix} P_{11}^{(i+1)} & P_{12}^{(i+1)} \\ P_{21}^{(i+1)} & P_{22}^{(i+1)} \end{pmatrix} \begin{pmatrix} \Delta_{i+1,r} \\ \Delta_{i+1,l} \end{pmatrix} \\
&= \begin{pmatrix} P_{11}^{(i+1)}\Delta_{i+1,r} + P_{12}^{(i+1)}\Delta_{i+1,l} \\ P_{21}^{(i+1)}\Delta_{i+1,r} + P_{22}^{(i+1)}\Delta_{i+1,l} \end{pmatrix}
\end{aligned} \tag{G.22}$$

now it yields

$$\begin{aligned}\frac{v_{1,i+1}-v_{2,i+1}}{v_{1,i}-v_{2,i}} &= \tau_{i+1,i}\frac{(P_{11}^{(i+1)}+P_{21}^{(i+1)})\Delta_{i+1,r}-(P_{12}^{(i+1)}+P_{22}^{(i+1)})\Delta_{i+1,l}}{(P_{11}^{(i+1)}+P_{21}^{(i+1)})(e^{-i\kappa_{i+1}d_{i+1}}\Delta_{i,r}+\rho_{i+1,i}e^{-i\kappa_{i+1}d_{i+1}}\Delta_{i,l})} \\ &\qquad -(P_{12}^{(i+1)}+P_{22}^{(i+1)})(\rho_{i+1,i}e^{i\kappa_{i+1}d_{i+1}}\Delta_{i,r}+e^{i\kappa_{i+1}d_{i+1}}\Delta_{i,l}) \\ &= \tau_{i+1,i}\frac{\Delta_{i+1,r}-\frac{P_{12}^{(i+1)}+P_{22}^{(i+1)}}{P_{11}^{(i+1)}+P_{21}^{(i+1)}}\Delta_{i+1,l}}{(e^{-i\kappa_{i+1}d_{i+1}}\Delta_{i,r}+\rho_{i+1,i}e^{-i\kappa_{i+1}d_{i+1}}\Delta_{i,l})} \\ &\qquad -\frac{P_{12}^{(i+1)}+P_{22}^{(i+1)}}{P_{11}^{(i+1)}+P_{21}^{(i+1)}}(\rho_{i+1,i}e^{i\kappa_{i+1}d_{i+1}}\Delta_{i,r}+e^{i\kappa_{i+1}d_{i+1}}\Delta_{i,l})\end{aligned} \tag{G.23}$$

Since propagation and transmission matrices are in below form for all layers and interfaces

$$\begin{pmatrix} a & b \\ b^* & a^* \end{pmatrix} \tag{G.24}$$

so

$$\left|\frac{a+b^*}{b+a^*}\right| = 1 \tag{G.25}$$

and any product of these matrices will be

$$\begin{pmatrix} a_1 & b_1 \\ b_1^* & a_1^* \end{pmatrix}\begin{pmatrix} a_2 & b_2 \\ b_2^* & a_2^* \end{pmatrix} = \begin{pmatrix} c_{11} & c_{12} \\ c_{21} & c_{22} \end{pmatrix} \tag{G.26}$$

like

$$\left|\frac{c_{11}+c_{21}}{c_{12}+c_{22}}\right| = \left|\frac{a_1a_2+b_1b_2^*+a_1b_2+b_1a_2^*}{a_1^*a_2^*+b_1^*b_2+a_1^*b_2^*+b_1^*a_2}\right| = 1 \tag{G.27}$$

so in general for any arbitrary number of product of these matrices, above relation will hold, and therefore we can write below relation where it is only a phase and its magnitude is one:

$$\frac{P_{12}^{(i+1)}+P_{22}^{(i+1)}}{P_{11}^{(i+1)}+P_{21}^{(i+1)}} = e^{i\alpha_{i+1}} \tag{G.28}$$

so we will have

$$\begin{aligned}
&\frac{v_{1,i+1}-v_{2,i+1}}{v_{1,i}-v_{2,i}} \\
&= \tau_{i+1,i}\frac{\Delta_{i+1,r}-e^{i\alpha_{i+1}}\Delta_{i+1,l}}{(e^{-i\kappa_{i+1}d_{i+1}}\Delta_{i,r}+\rho_{i+1,i}e^{-i\kappa_{i+1}d_{i+1}}\Delta_{i,l}) \\
&\qquad -e^{i\alpha_{i+1}}(\rho_{i+1,i}e^{i\kappa_{i+1}d_{i+1}}\Delta_{i,r}+e^{i\kappa_{i+1}d_{i+1}}\Delta_{i,l})} \\
&= \tau_{i+1,i}\frac{\Delta_{i+1,r}-e^{i\alpha_{i+1}}\Delta_{i+1,l}}{(e^{-i\kappa_{i+1}d_{i+1}}-e^{i\alpha_{i+1}}\rho_{i+1,i}e^{i\kappa_{i+1}d_{i+1}})\Delta_{i,r} \\
&\qquad +(\rho_{i+1,i}e^{-i\kappa_{i+1}d_{i+1}}-e^{i\alpha_{i+1}}e^{i\kappa_{i+1}d_{i+1}})\Delta_{i,l}} \\
&= \tau_{i+1,i}\frac{\Delta E_{i+1,r}+e^{i\alpha_{i+1}}\Delta E_{i+1,l}e^{i\kappa_{i+1}d_{i+1}}}{(e^{-i\kappa_{i+1}d_{i+1}}-e^{i\alpha_{i+1}}\rho_{i+1,i}e^{i\kappa_{i+1}d_{i+1}})\Delta E_{i,r} \\
&\qquad -(\rho_{i+1,i}e^{-i\kappa_{i+1}d_{i+1}}-e^{i\alpha_{i+1}}e^{i\kappa_{i+1}d_{i+1}})\Delta E_{i,l}e^{i\kappa_i d_i}}
\end{aligned} \tag{G.29}$$

Using equations (E.11) and (E.12), and the relation $E_{F,i,r} = e^{i\phi}E^*_{F,i,l}$, the two relations below can be derived:

$$\Delta E_{i,r} = -e^{3i\phi}e^{-i\kappa_i d_i}\Delta E^*_{i,l} \tag{G.30}$$

$$\Delta E_{i+1,r} = -e^{3i\phi}e^{-i\kappa_{i+1}d_{i+1}}\Delta E^*_{i+1,l} \tag{G.31}$$

after plug in

$$\begin{aligned}
\frac{v_{1,i+1}-v_{2,i+1}}{v_{1,i}-v_{2,i}} &= \tau_{i+1,i}\times\frac{-e^{3i\phi}e^{-i\kappa_{i+1}d_{i+1}}\Delta E^*_{i+1,l}+e^{i\alpha_{i+1}}\Delta E_{i+1,l}e^{i\kappa_{i+1}d_{i+1}}}{-(e^{-i\kappa_{i+1}d_{i+1}}-e^{i\alpha_{i+1}}\rho_{i+1,i}e^{i\kappa_{i+1}d_{i+1}})e^{3i\phi}e^{-i\kappa_i d_i}\Delta E^*_{i,l}} \\
&\qquad -(\rho_{i+1,i}e^{-i\kappa_{i+1}d_{i+1}}-e^{i\alpha_{i+1}}e^{i\kappa_{i+1}d_{i+1}})\Delta E_{i,l}e^{i\kappa_i d_i}
\end{aligned}$$

$$\begin{aligned}
&= \tau_{i+1,i}\times\frac{e^{3i\phi}e^{-i\kappa_{i+1}d_{i+1}}\Delta E^*_{i+1,l}-e^{i\alpha_{i+1}}\Delta E_{i+1,l}e^{i\kappa_{i+1}d_{i+1}}}{(e^{-i\alpha_{i+1}}e^{-i\kappa_{i+1}d_{i+1}}-\rho_{i+1,i}e^{i\kappa_{i+1}d_{i+1}})e^{i\alpha_{i+1}}e^{3i\phi}e^{-i\kappa_i d_i}\Delta E^*_{i,l}} \\
&\qquad +(\rho_{i+1,i}e^{-i\kappa_{i+1}d_{i+1}}-e^{i\alpha_{i+1}}e^{i\kappa_{i+1}d_{i+1}})\Delta E_{i,l}e^{i\kappa_i d_i}
\end{aligned} \tag{G.32}$$

now if we define two relations as follow

$$z_1 = \tau_{i+1,i}e^{i\kappa_{i+1}d_{i+1}}\Delta E_{i+1,l} \tag{G.33}$$

$$z_1 = |z_1|e^{i\theta_1} \tag{G.34}$$

and

$$z_2 = (\rho_{i+1,i} e^{-i\kappa_{i+1} d_{i+1}} - e^{i\alpha_{i+1}} e^{i\kappa_{i+1} d_{i+1}}) e^{i\kappa_i d_i} \Delta E_{i,l} \tag{G.35}$$

$$z_2 = |z_2| e^{i\theta_2} \tag{G.36}$$

so we can rewrite equation in this form

$$\begin{aligned}
\frac{v_{1,i+1} - v_{2,i+1}}{v_{1,i} - v_{2,i}} &= \frac{e^{3i\phi} z_1^* - e^{i\alpha_{i+1}} z_1}{-e^{i\alpha_{i+1}} e^{3i\phi} z_2^* + z_2} \\
&= \left|\frac{z_1}{z_2}\right| \frac{e^{3i\phi} e^{-i\theta_1} - e^{i\alpha_{i+1}} e^{+i\theta_1}}{-e^{i\alpha_{i+1}} e^{3i\phi} e^{-i\theta_2} + e^{i\theta_2}} \\
&= \left|\frac{z_1}{z_2}\right| \frac{e^{3i\phi} e^{-i\theta_1} - e^{i\alpha_{i+1}} e^{+i\theta_1}}{-e^{i\alpha_{i+1}} e^{3i\phi} e^{-i\theta_2} + e^{i\theta_2}} \frac{-e^{-i\alpha_{i+1}} e^{-3i\phi} e^{i\theta_2} + e^{-i\theta_2}}{-e^{-i\alpha_{i+1}} e^{-3i\phi} e^{i\theta_2} + e^{-i\theta_2}} \\
&= \left|\frac{z_1}{z_2}\right| \frac{-e^{-i(\alpha_{i+1}+\theta_1-\theta_2)} - e^{i(\alpha_{i+1}+\theta_1-\theta_2)} + e^{-i(3\phi-\theta_1-\theta_2)} + e^{i(3\phi-\theta_1-\theta_2)}}{2(1 - cos(\alpha_{i+1} + 3\phi - 2\theta_2))} \\
&= \left|\frac{z_1}{z_2}\right| \frac{-cos(\alpha_{i+1} + \theta_1 - \theta_2) + cos(3\phi - \theta_1 - \theta_2)}{1 - cos(\alpha_{i+1} + 3\phi - 2\theta_2)}
\end{aligned} \tag{G.37}$$

which is a real number. So, the all terms in Eq. (G.18) are real.

References

[1] M. Mero, J. Liu, W. Rudolph, D. Ristau, and K. Starke, "Scaling laws of femtosecond laser pulse induced breakdown in oxide films," *Physical Review B*, vol. 71, no. 11, p. 115109, 2005.

[2] P. Broqvist and A. Pasquarello, "Oxygen vacancy in monoclinic HfO2: A consistent interpretation of trap assisted conduction, direct electron injection, and optical absorption experiments," *Applied Physics Letters*, vol. 89, no. 26, pp. 2004–2007, 2006.

[3] J. M. Liu, "Simple technique for measurements of pulsed Gaussian-beam spot sizes," *Optics Letters*, vol. 7, no. 5, p. 196, 1982.

[4] C. Rodríguez and W. Rudolph, "Characterization and $\chi\hat{}3$ measurements of thin films by third-harmonic microscopy," *Optics Letters*, vol. 39, no. 20, p. 6042, 2014.

[5] N. Boling, A. Glass, and A. Owyoung, "Empirical relationships for predicting nonlinear refractive index change in optical solids," *IEEE Journal of Quantum Electronics*, vol. 14, no. 8, pp. 601–608, 1978.

[6] A. Khabbazi Oskouei, S. Baur, L. Emmert, M. Jupe, T. Willemsen, M. Steinecke, L. Jensen, D. Ristau, and W. Rudolph, "Femtosecond laser-induced modifications of frequency tripling mirrors," in *Laser-Induced Damage in Optical Materials 2018: 50th Anniversary Conference* (V. E. Gruzdev, D. Ristau, M. Soileau, G. J. Exarhos, and C. W. Carr, eds.), no. November, p. 66, SPIE, nov 2018.

[7] R. W. Boyd, *Nonlinear Optics*. Academic Press, 3 ed., 2008.

[8] P. A. Franken, A. E. Hill, C. W. Peters, and G. Weinreich, "Generation of optical harmonics," *Physical Review Letters*, vol. 7, no. 4, pp. 118–119, 1961.

[9] J. F. Ward and G. H. C. New, "Optical Third Harmonic Generation in Gases by a Focused Laser Beam," *Physical Review*, vol. 185, no. 1, pp. 57–72, 1969.

[10] R. W. Terhune, P. D. Maker, and C. M. Savage, "Physical Review Letters," *J. Phys. Rev. Letters*, vol. 8, no. 10, pp. 404–406, 1962.

[11] P. J. Wegner, J. M. Auerbach, T. A. Biesiada, Jr., S. N. Dixit, J. K. Lawson, J. A. Menapace, T. G. Parham, D. W. Swift, P. K. Whitman, and W. H. Williams, "NIF final optics system: frequency conversion and beam conditioning," *Proceedings of SPIE*, p. 180, 2004.

[12] P. J. Wegner, J. M. Auerbach, C. E. Barker, S. C. Burkhart, S. A. Couture, J. J. DeYoreo, R. L. Hibbard, L. W. Liou, M. A. Norton, P. K. Whitman, and L. A. Hackel, "Frequency converter development for the National Ignition Facility," p. 392, jul 1999.

[13] Y. Barad, H. Eisenberg, M. Horowitz, and Y. Silberberg, "Nonlinear scanning laser microscopy by third harmonic generation," *Applied Physics Letters*, vol. 70, no. 8, pp. 922–924, 1997.

[14] B. Weigelin, G.-J. Bakker, and P. Friedl, "Third harmonic generation microscopy of cells and tissue organization," *Journal of Cell Science*, vol. 129, no. 2, pp. 245–255, 2016.

[15] R. A. Weber, *Nonlinear Microscopy for Material Characterization*. The University of New Mexico. ProQuest Dissertations Publishing, 2012. 3553920., 2013.

[16] G. I. Petrov, V. Shcheslavskiy, V. V. Yakovlev, I. Ozerov, E. Chelnokov, and W. Marine, "Efficient third-harmonic generation in a thin nanocrystalline film of ZnO," *Applied Physics Letters*, vol. 83, no. 19, pp. 3993–3995, 2003.

[17] T. M. Kardaś, M. Nejbauer, P. Wnuk, B. Resan, C. Radzewicz, and P. Wasylczyk, "Full 3D modelling of pulse propagation enables efficient nonlinear frequency conversion with low energy laser pulses in a single-element tripler," *Scientific Reports*, vol. 7, p. 42889, 2017.

[18] W. Seka, S. D. Jacobs, J. E. Rizzo, R. Boni, and R. S. Craxton, "Demonstration of high efficiency third harmonic conversion of high power Nd-glass laser radiation," *Optics Communications*, vol. 34, no. 3, pp. 469–473, 1980.

[19] K. Miyata, V. Petrov, and F. Noack, "High-efficiency single-crystal third-harmonic generation in BiB_3O_6," *Optics Letters*, vol. 36, no. 18, p. 3627, 2011.

[20] R. Craxton, "High efficiency frequency tripling schemes for high-power Nd: Glass lasers," *IEEE Journal of Quantum Electronics*, vol. 17, pp. 1771–1782, sep 1981.

[21] M. R. Shcherbakov, D. N. Neshev, B. Hopkins, A. S. Shorokhov, I. Staude, E. V. Melik-Gaykazyan, M. Decker, A. A. Ezhov, A. E. Miroshnichenko, I. Brener, A. A. Fedyanin, and Y. S. Kivshar, "Enhanced third-harmonic generation in silicon nanoparticles driven by magnetic response," *Nano Letters*, vol. 14, no. 11, pp. 6488–6492, 2014.

[22] N. Kumar, J. Kumar, C. Gerstenkorn, R. Wang, H. Y. Chiu, A. L. Smirl, and H. Zhao, "Third harmonic generation in graphene and few-layer graphite films," *Physical Review B - Condensed Matter and Materials Physics*, vol. 87, no. 12, 2013.

[23] T. Tsang, "Reflected optical harmonics from dielectric mirrors," *Applied Optics*, vol. 33, no. 33, p. 7720, 1994.

[24] C. Rodríguez, S. Günster, D. Ristau, and W. Rudolph, "Frequency tripling mirror," *Optics Express*, vol. 23, no. 24, p. 31594, 2015.

[25] A. M. Zheltikov, "Third-harmonic generation with no signal at 3ω," *Physical Review A - Atomic, Molecular, and Optical Physics*, vol. 72, no. 4, pp. 1–5, 2005.

[26] D. Nguyen, L. A. Emmert, I. V. Cravetchi, M. Mero, W. Rudolph, M. Jupe, M. Lappschies, K. Starke, and D. Ristau, "TixSi1-xO2 optical coatings with tunable index and their response to intense subpicosecond laser pulse irradiation," *Applied Physics Letters*, vol. 93, no. 26, 2008.

[27] R. Trebino, *Frequency-Resolved Optical Gating: The Measurement of Ultrashort Laser Pulses*. Boston, MA: Springer US, 2000.

[28] F. L. Pedrotti, L. M. Pedrotti, and L. S. Pedrotti, *Introduction to Optics*. Cambridge University Press, 3rd ed., dec 2017.

[29] J.-C. Diels and W. Rudolph, *Phenomena, Ultrashort Laser Pulse Fundamentals, Techniques, and Applications on a Femtosecond Time Scale*. Academic Press, 2nd ed., 2006.

[30] C. Rodriguez and W. Rudolph, "Modeling third-harmonic generation from layered materials using nonlinear optical matrices," *Optics Express*, vol. 22, no. 21, pp. 1678–1684, 2014.

[31] C. C. Davis, *Lasers and Electro-optics: Fundamentals and Engineering*. Cambridge University Press, 1 ed., 1996.

[32] N. Kaiser and H. K. Pulker, eds., *Optical Interference Coatings*, vol. 88 of *Springer Series in Optical Sciences*. Berlin, Heidelberg: Springer Berlin Heidelberg, 2003.

[33] T. Willemsen, P. Geerke, M. Jupé, L. Gallais, and D. Ristau, "Electronic quantization in dielectric nanolaminates," p. 100140C, dec 2016.

[34] A. K. Oskouei, L. Emmert, M. Steinecke, M. Jupé, D. Ristau, A. K. Oskouei, L. Emmert, M. Steinecke, M. Jupé, L. Jensen, and W. Rudolph, "tool to study dielectric material damage threshold (LIDT)," no. November, 2019.

[35] L. A. Emmert, C. Rodriguez, Z. Sun, F. Beygi Azar Aghbolagh, S. Günster, D. Ristau, D. Patel, C. S. Menoni, and W. Rudolph, "Optical coatings excited by femtosecond lasers near the damage threshold: challenges and opportunities," in *Proc. of SPIE 9632, 96320K* (G. J. Exarhos, V. E. Gruzdev, J. A. Menapace, D. Ristau, and M. Soileau, eds.), p. 96320K, nov 2015.

[36] K. Olson, A. Ogloza, J. Thomas, and J. Talghader, "High power laser heating of low absorption materials," *Journal of Applied Physics*, vol. 116, no. 12, 2014.

[37] O. Razskazovskaya, T. T. Luu, M. K. Trubetskov, E. Goulielmakis, and V. Pervak, "Nonlinear behavior and damage of dispersive multilayer optical coatings induced by two-photon absorption," vol. 9237, p. 92370L, 2014.

[38] R. DeSalvo, A. A. Said, D. J. Hagan, E. W. Van Stryland, and M. Sheik-Bahae, "Infrared to ultraviolet measurements of two-photon absorption and n2 in wide bandgap solids," *IEEE Journal of Quantum Electronics*, vol. 32, no. 8, pp. 1324–1333, 1996.

[39] M. Mero, A. J. Sabbah, J. Zeller, and W. Rudolph, "Femtosecond dynamics of dielectric films in the pre-ablation regime," *Applied Physics A: Materials Science and Processing*, vol. 81, no. 2, pp. 317–324, 2005.

[40] A. Rosenfeld, M. Lorenz, R. Stoian, and D. Ashkenasi, "Ultrashort-laser-pulse damage threshold of transparent materials and the role of incubation," *Applied Physics A: Materials Science and Processing*, vol. 69, no. 7, pp. 373–376, 1999.

[41] L. A. Emmert, M. Mero, and W. Rudolph, "Modeling the effect of native and laser-induced states on the dielectric breakdown of wide band gap optical materials by multiple subpicosecond laser pulses," *Journal of Applied Physics*, vol. 108, no. 4, 2010.

[42] J. Jasapara, A. V. Nampoothiri, W. Rudolph, D. Ristau, and K. Starke, "Femtosecond laser pulse induced breakdown in dielectric thin films," *Physical Review B - Condensed Matter and Materials Physics*, 2001.

[43] N. Blombergen, "Laser-Induced Electric Breakdown in Solids," *IEEE Journal of Quantum Electronics*, no. 3, pp. 375–386, 1974.

[44] L. V. Keldysh, "Ionization in the field of a strong electromagnetic wave," *Soviet Physics JETP*, 1965.

[45] N. Peyghambarian, S. Koch, and A. Mysyrowicz, *Introduction to Semiconductor Optics*. Englewood Cliffs, New Jersey: Prentice-Hall, 1993.

[46] A. Khabbazi Oskouei, M. Lenzner, L. A. Emmert, M. Jupé, T. Willemsen, M. Steinecke, D. Ristau, and W. Rudolph, "Damage threshold affected by the spatiotemporal evolution of femtosecond laser pulses in multilayer structures," *Optical Engineering*, vol. In press.